

Protein Adsorption in Tentacle-Type Anion Exchangers and the Influence of Process Related  
Fouling

---

A Thesis

Presented to

the faculty of the School of Engineering and Applied Science

University of Virginia

---

In partial Fulfillment

of the requirements for the Degree

Master of Science in Chemical Engineering

by

Rachel Elizabeth Corbett

April 2012

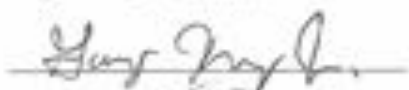
APPROVAL SHEET

The thesis  
is submitted in partial fulfillment of the requirements  
for the degree of  
Master of Science

  
AUTHOR

The thesis has been read and approved by the examining committee:

  
Advisor

  
\_\_\_\_\_

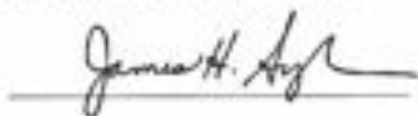
\_\_\_\_\_

\_\_\_\_\_

\_\_\_\_\_

\_\_\_\_\_

Accepted for the School of Engineering and Applied Science:

  
\_\_\_\_\_

Dean, School of Engineering and Applied Science

May  
2012

## Abstract

The physical and protein adsorption properties of Fractogel TMAE, a tentacle-type anion exchange resin, were investigated for both virgin and used samples to determine the influence of process related fouling. The resin average particle diameter was found to vary between 70 and 72  $\mu\text{m}$  for different resin lots. Inverse size exclusion chromatography (iSEC) indicated a bimodal distribution of pore sizes, with some large pores, 40 nm in radius, occupying about 9% of the particle volume and much smaller pores, with radius between 4 and 5 nm, occupying 74% of the particle volume. Similar results were obtained by iSEC for resin samples fouled by process use, indicating that the core structure of these particles is unchanged. Transmission electron micrographs (TEM) showed that the resin backbone has a microgranular structure and that the same structure persists. In this case, however, a dense layer, approximately 0.5  $\mu\text{m}$  thick, was also seen at the particle exterior surface of the fouled particles. The equilibrium binding capacity of BSA was determined to be  $178 \pm 1$  mg/mL for both virgin and fouled samples, respectively, while the corresponding values for Thyroglobulin were  $95 \pm 4$  and  $25 \pm 2$  mg/mL. The BSA adsorption kinetics was also 2-3 fold slower for the fouled resin, but much larger differences between virgin and fouled resin were seen for the much larger Thyroglobulin. Based on the shape of intraparticle protein concentration profiles determined by confocal laser scanning microscopy (CLSM), the protein transport mechanism was determined to be “solid diffusion” for both virgin and fouled resin samples and proteins. However, transport of Thyroglobulin was much slower for the fouled sample as a result of its larger size and increased diffusional hindrance in the fouled surface layer. The key conclusion is that fouling occurs through the formation of a thin but very dense skin layer that greatly affects the transport kinetics of large proteins.

## Acknowledgements

I greatly appreciate all faculty and graduate students within the Chemical Engineering Department for making my experience at the University of Virginia memorable. I would like to individually thank the following people:

- My advisor, Giorgio Carta, for his guidance and direction throughout my research.
- Dr. Inchan Kwon and Dr. Gary Koenig for being on my thesis committee.
- Ranga Godavarti, Jeff Salm, Glen Bolton, Chris Gallo, and Tim Iskra from Pfizer for sharing their knowledge of protein purification processes
- My research group, Ernie Perez-Almodovar, Tarl Vetter, Yige Wu, Frank Bartnik, Drew Bundschuh, and Mimi Zhu, for their help with my research and the countless memories.
- My family for their unconditional love and support, I would not be where I am today without their encouragement.
- My boyfriend, Christopher, who has supported me throughout this process and never let me lose sight of my goals.

## Table of Contents

<b>Abstract .....</b>	<b>i</b>
<b>Acknowledgements .....</b>	<b>ii</b>
<b>Table of Contents.....</b>	<b>iii</b>
<b>List of Figures .....</b>	<b>v</b>
<b>List of Tables.....</b>	<b>viii</b>
<b>List of Symbols.....</b>	<b>ix</b>
<b>Chapter 1. Introduction .....</b>	<b>1</b>
<b>Chapter 2. Background Theory .....</b>	<b>6</b>
2.1. Protein adsorption kinetics.....	6
2.1.1. Extraparticle transport .....	6
2.1.2. Intraparticle transport .....	7
2.1.3. Comparison of extraparticle and intraparticle resistances.....	8
2.1.4. Micro-scale comparison of transport mechanisms .....	9
2.2. Fouling behavior .....	10
<b>Chapter 3. Experimental Materials and Methods.....</b>	<b>13</b>
3.1 Materials .....	13
3.2 Methods.....	17
3.2.1 Inverse size exclusion chromatography.....	17
3.2.2 Transmission electron microscopy .....	19
3.2.2.1 Effect of column compression .....	19
3.2.2.2 Fouling of packed mini-column.....	21
3.2.3 Protein binding capacity studies .....	21
3.2.4 Batch adsorption kinetics.....	22
3.2.5 Confocal laser scanning microscopy .....	24
3.2.5.1 Fluorescent labeling of proteins.....	25
3.2.5.2 Avoiding fluorescence attenuation effects.....	27
3.2.5.4 CLSM measurements.....	31

<b>Chapter 4. Results for Virgin Resin Samples.....</b>	<b>35</b>
4.1 Inverse size exclusion chromatography .....	35
4.2 Transmission electron microscopy.....	41
4.3 Protein binding capacity studies .....	57
4.3.1 Batch adsorption kinetics.....	59
4.4 Confocal laser scanning microscopy.....	63
<b>Chapter 5. Results for Fouled Resin Samples.....</b>	<b>70</b>
5.1 Inverse size exclusion chromatography .....	70
5.2 Transmission electron microscopy.....	73
5.3 Protein binding capacity studies .....	82
5.3.1 Batch adsorption kinetics.....	87
5.4 Confocal laser scanning microscopy.....	90
5.4.1 Single component adsorption .....	90
5.4.2 Sequential adsorption .....	93
<b>Chapter 6. Conclusions .....</b>	<b>96</b>
6.1 Physical properties of Fractogel TMAE HiCap (m) .....	96
6.2 Protein adsorption properties .....	97
6.3 Mechanism of protein transport .....	98
6.4 Impact of process Use .....	98
<b>Chapter 7. Recommendations .....</b>	<b>101</b>
7.1 Determination of foulant species .....	101
7.2 Mechanism of process related fouling .....	102
<b>Chapter 8. References .....</b>	<b>103</b>

## List of Figures

<b>Figure 2.1.</b> Sketches of “homogeneous fouling” and “surface fouling” mechanisms of a tentacle type resin where the black areas represent the resin backbone, the grey strands represent the functionalized tentacles and the aggregates represent the foulant species. ....	11
<b>Figure 2.2.</b> Depiction of the additional film resistance created by surface fouling where the dashed line indicates the foulant layer and the dotted line represents the boundary layer outside the resin particle.....	11
<b>Figure 3.1.</b> Particle size distributions for Fractogel TMAE HiCap (m) Samples A and B.....	15
<b>Figure 3.2.</b> Size exclusion chromatography analyses for as-received and purified BSA.....	16
<b>Figure 3.3.</b> Images of equipment used for column compression studies.....	20
<b>Figure 3.4.</b> Schematic of stirred-batch apparatus. ....	23
<b>Figure 3.5.</b> Gradient elution analyses of native and dye-conjugated proteins on a Fractogel TMAE column (Sample B) at pH 8.5. Top panels: BSA native and labeled using Rhodamine Red <sup>TM</sup> -X. Bottom panels: Thyroglobulin native and labeled using Rhodamine Green <sup>TM</sup> -X.....	28
<b>Figure 3.6.</b> Predicted relationship between emitted fluorescence for Rhodamine Red labeled BSA as a function of protein concentration at the center of a 100 $\mu\text{m}$ particle for 1:1 dye-to-protein ratio (left) and 1:40 dye-to-protein ratio (right). ....	30
<b>Figure 3.7.</b> Optical Images of Fractogel TMAE HiCap (m) when immersed in TRIS buffer solution (left) and a 30% sucrose solution (right). ....	32
<b>Figure 4.1.</b> Inverse size exclusion results for (a) dextran standards and (b) un-retained proteins for Sample B. The dashed line represents the retention volume of T2000.....	36
<b>Figure 4.2.</b> Comparison of iSEC retention volumes at the peak maxima as a function of molecular radius for dextran standards and un-retained proteins.....	37
<b>Figure 4.3.</b> Inverse size exclusion results for two lots of Fractogel TMAE, (a) Sample A and (b) Sample B, where the dashed line represents the retention volume of T2000.....	38
<b>Figure 4.4.</b> Comparison of experimental and theoretical $K_D$ -values for Sample B based on unimodal and bimodal pore size distribution models.....	41
<b>Figure 4.5.</b> Electron micrographs of Fractogel TMAE HiCap (m). TEM used to obtain imaging of interior structure. (a) 5k Image of Sample A at the edge (b) 10k at the center of the particle; (c) 5k Image of Sample B at the edge, and (d) 10k at the center of the particle. ....	43
<b>Figure 4.6.</b> Electron micrographs of Fractogel TMAE Sample B saturated with BSA. (a) 5k magnification image at the center of the particle, (b) 5k magnification image at the edge of the particle, and (c) 10k magnification image at the edge of the particle. ....	48

- Figure 4.7.** Optical images of mini-columns mechanically compressed to 10, 17 and 30% compression, embedded with LR White, dried onto microscope slides and stained using electric blue. ....50
- Figure 4.8.** Comparison of experimental and theoretical  $\varepsilon$ -values based on two compressibility models as described in eqs. 4.5 and 4.6. ....53
- Figure 4.9.** Representative electron micrographs of Fractogel TMAE HiCap (m) within a 30% mechanically compressed column. Low magnification images of two particles in (a) close contact and (b) touching. Higher magnification images of two particles touching are shown at (c) 5k with (d) a 10k close up of the area of contact. ....54
- Figure 4.10.** Single component adsorption isotherms for Sample B for (a) BSA and (b) Thyroglobulin. ....59
- Figure 4.11.** Batch uptake curves for purified BSA and Thyroglobulin at different initial protein concentrations. ....61
- Figure 4.12.** Batch uptake curves for BSA at different initial protein concentrations. The line shows the fitted curves obtained using the pore diffusion model. ....62
- Figure 4.13.** Comparison of batch uptake curves for 2 mg/mL purified BSA using TRIS buffer and 30% sucrose solution. ....65
- Figure 4.14.** CLSM images of batch adsorption of 0.2 mg/mL BSA in Fractogel TMAE Sample B. The laser intensity was varied in order to avoid saturation of the CCD detector; up to 9 minutes an intensity of 2% was used, with an intensity of 0.8% thereafter. ....66
- Figure 4.15.** CLSM images of batch adsorption of 0.5 mg/ml BSA in Fractogel TMAE Sample B. The laser intensity was varied in order to avoid saturation of the CCD detector; up to 9 minutes an intensity of 2% was used, with an intensity of 0.8% thereafter. The individual resin bead diameter is shown in parentheses above each image. ....68
- Figure 4.16.** Batch adsorption CLSM images of 0.2 mg/mL BSA 30% sucrose solution using Fractogel TMAE Sample B. The laser intensity was varied in order to avoid saturation of the CCD detector; up to 12 minutes an intensity of 4% was used, with an intensity of 2% thereafter. The individual resin bead diameter is shown in parentheses above each image. ....69
- Figure 4.17.** CLSM images of batch adsorption of 0.2 mg/mL Thyroglobulin in Fractogel TMAE Sample B. Each of the images shown was taken at an intensity of 19%. The individual resin bead diameter is shown in parentheses above each image. ....70
- Figure 5.1.** Inverse size exclusion results for Fractogel TMAE (a) Sample B – clean and (b) Sample D – fouled. The dashed line represents the retention volume of T2000. Both columns had an internal diameter of 0.5 cm and were ran at a flow rate of 0.5 mL/min. The lengths of the packed bed were 5.6 and 5.5 cm for Samples A and B, respectively. ....71
- Figure 5.2.** Comparison of experimental and theoretical KD-values for Sample D based on unimodal and bimodal pore distribution models. ....72

**Figure 5.3.** Transmission electron micrographs of Fractogel TMAE HiCap (m) Sample D. (a) Image of particle at 1k magnification showing a denser skin layer over a substantial portion of the particle exterior; (b) 10k image showing structure of dense skin layer, about 0.5  $\mu\text{m}$  thick, at particle exterior surface; (c) 10k image of particle interior showing no evidence of foulant. .... 74

**Figure 5.4.** TEMs of Fractogel TMAE Sample B particles packed into a mini-column, mechanically compressed 30%, and fouled as discussed in Section 3.2.2.2. The black and white arrows highlight the fouled and clean areas, respectively. (a) Particles in close proximity; (b) particles in contact with each other; (c) high magnification image of particles in contact with each other; (d) high magnification image of the particles in (c); (e) high magnification image of exposed particle surface..... 77

**Figure 5.5.** TEMs of a fouled sample of Fractogel TMAE after a protease treatment. (a) 5k magnification image at edge of particle; (b) 5k magnification image of particle interior; (c) 10k magnification image of edge of particle..... 83

**Figure 5.6.** Protein binding capacities for Samples B and D using (a) BSA and (b) Thyroglobulin after 1.5 hours of protein exposure. Lines are calculated based on the Langmuir isotherm. .... 86

**Figure 5.7.** Batch uptake curves of BSA at different initial protein concentrations for (a) Sample B (virgin) and (b) Sample D (fouled). .... 88

**Figure 5.8.** Batch uptake curves for Thyroglobulin at different initial protein concentrations for Samples B (virgin) and D (fouled). .... 89

**Figure 5.9.** CLSM images of batch adsorption of 0.2 mg/ml purified BSA in Fractogel TMAE Sample D. The laser intensity was varied in order to avoid saturation of the CCD detector; up to 9 minutes an intensity of 2% was used, with an intensity of 0.8% thereafter. The individual resin bead diameter is shown in parentheses above each image. .... 100

**Figure 5.10.** CLSM images of batch adsorption of 0.2 mg/ml Thyroglobulin in Fractogel TMAE Sample D. Each of the images shown was taken at an intensity of 19%. The individual resin bead diameter is shown in parentheses above each image. .... 102

**Figure 5.11.** CLSM images of two-component batch adsorption using Thyroglobulin and purified BSA in series at concentrations of 0.2 mg/ml for Fractogel TMAE Sample B. The images were taken at an intensity of 19% for Thyroglobulin adsorption. The intensity was varied between 2% and 0.8% for the BSA adsorption in order to avoid saturation. The individual resin bead diameter is shown below each image..... 94

**Figure 5.12.** CLSM images of two-component batch adsorption in series using purified BSA and Thyroglobulin at concentrations on 0.2 mg/ml for Fractogel TMAE Sample D. The images were taken at an intensity of 19% for Thyroglobulin adsorption. The intensity was varied between 2% and 0.8% for the BSA adsorption in order to avoid saturation. The individual resin bead diameter is shown below each image..... 95

### List of Tables

<b>Table 3.1.</b> Properties fluorescent dyes used in this work. $\epsilon$ is the extinction coefficient at the emission maxima. ....	17
<b>Table 3.2.</b> Dextran standards and proteins used in iSEC experiments. ....	18
<b>Table 4.1.</b> Parameters obtained using unimodal and bimodal models for inverse size exclusion data.....	41
<b>Table 4.2.</b> Parameters obtained by fitting the BSA uptake data with the pore diffusion model..	62
<b>Table 5.1.</b> Parameters obtained for virgin (B) and fouled (D) samples using unimodal and bimodal models for inverse size exclusion data. Index (a) indicates the average pore radius reported by EMD Chemical for Fractogel TMAE.....	73
<b>Table 5.2.</b> Parameters obtained by fitting batch uptake data using purified BSA for Samples B and D with the pore diffusion model. ....	88

### List of Symbols

$A$	absorbance in a 1 cm cell ( $M^{-1}cm^{-1}$ )
$Bi$	Biot Number
$C$	protein concentration in the bulk liquid (mg/mL)
$C_{dye}$	molar concentration of dye (mol/L)
$C_o$	initial protein concentration in solution (mg/mL)
$C_p$	protein concentration in particle pores (mg/mL)
$C_s$	protein concentration at the particle surface (mg/mL)
$C_s'$	protein concentration on the particle side of the fouled layer (mg/mL)
$C_{total\ protein}$	total protein molar concentration (mol/L)
$CF_{280nm}$	correction factor for adsorption of dye at a wavelength of 280 nm
$d_p$	particle diameter ( $\mu m$ )
$\overline{d_p}$	average particle diameter ( $\mu m$ )
$D_e$	effective pore diffusivity ( $cm^2/s$ )
$D_e'$	effective pore diffusivity through the fouled layer (mg/mL)
$D_{e,app}$	apparent effective pore diffusivity ( $cm^2/s$ )
$D_o$	protein diffusivity in free solution ( $cm^2/s$ )
$D_s$	protein diffusivity in the adsorbed state ( $cm^2/s$ )
$I_{em}$	intensity of the fluorescence emitted
$I_{ex}$	intensity of the transmitted light
$I_{ex,o}$	intensity of the incident light
$J$	main transfer flux
$K$	equilibrium constant in Langmuir model (mL/mg)

$K_D$	distribution coefficient
$k_{dye}$	proportionality constant between the excitation light and emitted light
$k_f$	film mass transfer coefficient
$(k_f)_{fouled}$	mass transfer coefficient of the fouled resin
$(k_f)_{clean}$	mass transfer coefficient of the clean resin
$\ell$	optical path length (cm)
$m$	resin elasticity
$M_p$	molecular mass of the dextran sample (kDa)
$M_{resin}$	mass of the resin (g)
$q$	adsorbed protein concentration (mg/mL particle)
$q_m$	maximum binding capacity
$r_p$	particle radius ( $\mu\text{m}$ )
$r_{pore}$	average pore radius (nm)
$r_{pore,M}$	average pore radius of large pores (nm)
$r_{pore,m}$	average pore radius of micropores (nm)
$r_s$	hydrodynamic radii of the dextran standards (nm)
$Sh$	Sherwood number
$V$	protein solution volume (mL)
$V_c$	total column volume (mL)
$V_o$	extraparticle void volume (mL)
$V_R$	average retention volume (mL)
$V_{resin}$	volume of hydrated resin particles (mL)

**Greek Symbols**

$\varepsilon$	extraparticle void fraction
$\varepsilon_{dye}$	dye molar extinction coefficient ( $M^{-1}cm^{-1}$ )
$\varepsilon_m$	intraparticle porosity of micropores
$\varepsilon_M$	intraparticle porosity of large pores
$\varepsilon_o$	initial extra particle porosity
$\varepsilon_p$	intraparticle porosity
$\varepsilon_{protein}$	protein molar extinction coefficient ( $M^{-1}cm^{-1}$ )
$\delta'$	thickness of the fouled layer (nm)
$\lambda$	average compression of a packed bed
$\tau_p$	tortuosity factor

## Chapter 1. Introduction

Ion exchange chromatography is the most widely used industrial scale bio-purification technique for pharmaceutical proteins. Ion exchangers are broadly defined either as cation exchangers, which are negatively charged, or anion exchangers, which are positively charged. These materials reversibly adsorb oppositely charged biomolecules as a result of electrostatic interaction. For example, anion exchangers adsorb negatively charged species that are attracted to positively charged functional groups on the resin. Ion exchange resins are often highly hydrophilic and therefore nonspecific binding and protein unfolding are minimized. For these reasons, ion exchangers are widely accepted in biopharmaceutical manufacturing and are a component of practically all large-scale process schemes.

Ion exchangers are commonly used either in a capture mode, where the product of interest is bound and impurities flow through, or in “flow through” mode, where impurities are strongly bound and the product flows through the column. Intermediate cases are also possible where the target product is very weakly bound while the impurities are strongly held (Kelley et al. 2008). For example, in the purification of monoclonal antibodies, a multiple step process is normally used where the antibody is first bound on a highly selective affinity chromatography matrix containing Protein A as a ligand. Protein A is an immunoglobulin binding protein that forms a very strong complex with human IgG at neutral pHs. The majority of impurities present in monoclonal antibody culture supernatants, including host cell proteins, DNA, and viruses, are not bound to Protein A and flow through the column. However, a small fraction of impurities are still retained in the Protein A column, either because they are complexed to the IgG or because they are nonspecifically bound to the resin matrix. For example, Shukla and Hinckley (2008) have shown that for the case of the Protein A resin MabSelect, host cell proteins do not

independently bind to the resin matrix but are instead associated with the IgG product species. In this case, upon elution of the bound monoclonal antibody, which is obtained at low pH, these impurities contaminate the eluted product fraction. Since most of these impurities are acidic (i.e. negatively charged), an anion exchange column can be used to remove them from the target monoclonal antibody product in a “flow through” process. The pH and salt concentration at which these anion exchange steps are conducted are critical (Kelley et al., 2008). For example, adjusting pH and salt concentration over certain ranges allows one to remove both acidic impurities and weakly bound basic impurities.

Regardless of how the ion exchange process is conducted, process performance is influenced by two distinct characteristics: (a) the equilibrium binding capacity and (b) the adsorption kinetics. The equilibrium binding capacity influences how much of the target protein of impurities can be bound at equilibrium, while the adsorption kinetics determine the rate at which the adsorption process can occur and, thus, the residence time required within the column.

Additional factors that influence column performance include flow properties and fouling behavior. The flow properties are affected by the mechanical compressibility of the resin. Softer compressible particles result in higher operating pressures, which are not desirable. Thus, it is important to understand how the resin becomes compacted under both flow and mechanical compression. The fouling behavior is especially important when the feed solution contains large species, such as soluble aggregates or insoluble microparticles. In this case, fouling can occur as a result of irreversible binding of these species, which can either coat the chromatographic surface, thereby preventing adsorption of proteins, or block access to the resin pores thereby introducing a kinetic limitation to the rate at which proteins bind.

Adsorption equilibrium, kinetics, mechanical properties, and fouling characteristics are not only affected by the chemistry but also by the structural properties of the resin. Three broad categories of ion exchangers used in protein purification are gels, macroporous matrices, and composite materials. Gels are based on soft hydrophilic polymers, such as dextran or agarose, which are cross-linked to form a three-dimensional network matrix functionalized with ion exchange groups. These materials have high binding capacity, but are mechanically weak. Macroporous matrices are comprised of a rigid backbone, which can either be inorganic, or polymer-based. This backbone defines a network of large pores that allow the protein to diffuse in and bind to the pore surfaces. The rigid backbone structure provides strong mechanical properties, but generally limits the available surface area resulting in low binding capacities. Composite materials are usually obtained by incorporating flexible polymers, also called “tentacles”, grafted into a macroporous matrix. These polymers, functionalized with ion exchange groups, serve as “surface extenders” by defining a gel phase supported by the rigid backbone (Carta and Jungbauer, 2010). As a result, these composite materials can exhibit both high mechanical strength and high binding capacities.

Protein transport can also occur differently in these materials. In macroporous matrices, protein transport occurs by ordinary diffusion through the liquid filled macropores, termed “pore diffusion”. The driving force for this mechanism is the gradient in protein concentration in the liquid phase. For dilute solutions, this driving force is small resulting in low rates of adsorption. On the other hand, protein transport in gels and composite matrices can occur by a different mechanism, called “solid diffusion”, where the driving force is the gradient of protein concentration adsorbed in the gel. Since the latter can be very large when adsorption capacity is high, high mass transfer rates can be obtained (Stone and Carta, 2007; Suda et al., 2009).

This work examines the behavior of a tentacle-type anion exchanger, called Fractogel TMAE HiCap (m) (EMD Chemicals, Darmstadt, Germany), in its application to a “flow through” step in the purification of a monoclonal antibody. The specific aims of this work are to:

- a. Characterize the physical structure of the resin including particle size, accessible pore radius, and packing properties;
- b. Characterize the adsorption properties (binding capacity and adsorption kinetics) for two model acidic proteins with different molecular masses: Bovine serum albumin (MW~65,000) and Thyroglobulin (MW~650,000). It is assumed that these proteins are models for low and high molecular weight impurities found in monoclonal antibody feedstocks to a “flow through” anion exchange step; and
- c. Determine the nature and effects of fouling derived from actual process use of the resin on protein adsorptive properties.

The tools used to address these aims include:

- a. Optical microscopy to determine particle size and the particle size distribution of the resin;
- b. Inverse size exclusion chromatography (iSEC) with neutral probes to determine the size exclusion limit of the resin;
- c. Transmission electron microscopy (TEM) to determine the physical structure of the backbone matrix of the resin and the localization of foulants;
- d. Adsorption equilibrium measurements to determine the maximum binding capacity for both virgin and fouled resin;
- e. Transient batch uptake measurements to determine the protein adsorption kinetics for both virgin and fouled resin; and

- f. Confocal laser scanning microscopy (CLSM) to determine the movement of adsorbed protein molecules within individual resin particles for both virgin and fouled resin beads.

The results of this research are expected to not only shed light on the structural and functional properties of the resin, but also to help devise ways in which fouling and/or its effects can be mitigated.

## Chapter 2. Background Theory

This chapter provides theoretical background for two critical aspects of this work: (a) protein adsorption kinetics and (b) fouling mechanisms and their potential effects on protein adsorption.

### 2.1. Protein adsorption kinetics

Diffusional mass transfer typically controls protein adsorption kinetics due to the fact that proteins are large molecules and, thus, have low diffusivities. Both extraparticle mass transport and transport within the resin pores can potentially affect the overall adsorption kinetics, but their respective contribution is different for different conditions and intraparticle transport mechanisms.

#### 2.1.1. Extraparticle transport

In general, transport outside the particles is described in terms of a boundary layer resistance and is represented by a mass transfer coefficient,  $k_f$ . Accordingly, the protein mass transfer flux at the particle surface is given by:

$$J = k_f (C - C_s) \quad (2.1)$$

where  $C$  is the protein concentration in the bulk liquid and  $C_s$  is the protein concentration at the particle surface (LeVan and Carta, 2007). The mass transfer coefficient is usually expressed by the Sherwood number,  $Sh$ , that is defined as:

$$Sh = \frac{k_f d_p}{D_o} \quad (2.2)$$

where  $d_p$  is the particle diameter and  $D_o$  is the protein diffusivity in free solution. In turn, the value of  $Sh$  is determined by the flow outside of the particles, caused either by agitation when the particles are suspended in a mixed vessel, or by a pressure gradient when the particles are packed in the column. Engineering correlations are available to predict  $Sh$  for both of these cases as reviewed by LeVan and Carta (2007).

### 2.1.2. Intraparticle transport

Transport within the particles is typically completely diffusion-controlled since the pores are generally too small to allow convective flow. Two different diffusion mechanisms can be distinguished as “pore diffusion” and “solid diffusion” (LeVan and Carta, 2007). For “pore diffusion”, protein transport occurs through large, liquid-filled pores and the flux,  $J$ , is expressed by:

$$J = -D_e \nabla C_p \quad (2.3)$$

where  $D_e$  is the effective pore diffusivity and  $C_p$  is the protein concentration in the liquid within the pores.  $D_e$  can be written as follows (Cussler, 1997):

$$D_e = \frac{\varepsilon_p}{\tau_p} D_o \quad (2.4)$$

where  $\varepsilon_p$  is the particle porosity and  $\tau_p$  is its tortuosity factor. The latter accounts for the fact that the pores are not straight making the actual diffusion path longer. Since  $\varepsilon_p$  is less than 1 and  $\tau_p$  is greater than 1, the ratio  $D_e/D_o$  is always less than 1. Carta and Jungbauer (2010) suggest that  $D_e/D_o$  is around 0.1 for protein diffusion in typical macroporous matrices.

For “solid diffusion”, protein transport occurs in the adsorbed phase and is represented by the following equation (Levan and Carta, 2007):

$$J = -D_s \nabla q \quad (2.5)$$

where  $D_s$  is the protein diffusivity in the adsorbed state and  $q$  is the adsorbed protein concentration. This mechanism of transport requires the protein molecules to retain diffusional mobility in the adsorbed state either by migration along the surface or through interactions with flexible polymers in a gel.

As shown, for example, by Schirmer and Carta (2008), at the macroscopic level the mechanisms of pore and solid diffusion are not directly distinguishable because both lead to uptake curves (amount of protein adsorbed as a function of time) that have nearly the same shape

and the same dependence on particle size. In fact, in both cases the flux can be written as follows:

$$J = -D_{e,app} \nabla C \quad (2.6)$$

where  $D_{e,app}$  is an apparent effective pore diffusivity and  $C$  is the protein concentration in solution. When the actual mechanism is pore diffusion,  $D_{e,app}$  equals  $D_e$ . For solid diffusion, however,  $D_{e,app}$  can be approximated as follows:

$$D_{e,app} \cong D_s \frac{q}{C} \quad (2.7)$$

When protein binding is highly favorable,  $q$  is essentially independent of  $C$  and therefore  $D_{e,app}$  becomes inversely related to the protein concentration in solution.

### 2.1.3. Comparison of extraparticle and intraparticle resistances

As noted above, both extraparticle and intraparticle transport resistances can, in general, affect the overall rate of transport. Their relative importance is generally described by the Biot number,  $Bi$ . In terms of the apparent effective pore diffusivity defined by eq. 2.6,  $Bi$  is given by the following equation:

$$Bi = \frac{k_f r_p}{D_{e,app}} \quad (2.8)$$

where  $r_p$  is the particle radius. In general, the external resistance is negligible when  $Bi$  is greater than 10 (Carta and Jungbauer, 2010). Small values of  $Bi$ , on the other hand, indicate that external resistance is important or even dominant. In terms of  $Sh$ ,  $Bi$  can be written as follows:

$$Bi = \frac{1}{2} \frac{Sh}{(D_{e,app}/D_o)} \quad (2.9)$$

The Sherwood number is always larger than 2 and typically greater than 10 (LeVan and Carta, 2007). For pore diffusion  $D_{e,app}/D_o$  equals  $D_e/D_o$ , which is much less than 1. In this case,  $Bi$  is always large so that the external resistance is usually negligible. On the other hand, for solid diffusion,  $D_{e,app}/D_o$  is approximated as:

$$\frac{D_{e,app}}{D_o} = \frac{D_s}{D_o} \frac{q}{C} \quad (2.10)$$

which can be much larger than 1 making  $Bi$  small. In this case the external resistance can actually be dominant.

#### 2.1.4. Micro-scale comparison of transport mechanisms

As noted in the previous sections, intraparticle transport mechanisms are not directly distinguishable at the macroscopic level. However, profound differences can be seen microscopically. When binding is highly favorable, pore diffusion results in a sharp intraparticle concentration profile. In this case, when the particle is first exposed to a protein solution, a protein saturated layer is immediately formed at the particle surface and advances toward the center of the particle with a sharp interface between the advancing saturation front and the protein-free core. This situation is described by the well known shrinking core model (Froment and Bischoff, 1990). Conversely, when solid diffusion is dominant, the intraparticle concentration profile is expected to be smooth following the well-known trends predicted by Fick's second law of diffusion (Cussler, 1997). These qualitative differences can be brought to light by measuring intraparticle concentration profiles during transient adsorption within an individual resin bead.

As discussed in Section 2.1.3, when solid diffusion controls intraparticle transport the internal mass transfer resistance can be dominant, which occurs when  $Bi$  is much less than 10. In this case, except for at very short times, the intraparticle protein concentration profile is expected to be flat with the particle becoming uniformly saturated at a rate completely controlled by the external resistance. Determining intraparticle convection profiles can also elucidate this behavior.

## 2.2. Fouling behavior

In this context, resin fouling is defined as the irreversible binding or accumulation of materials on a chromatographic resin that prevents it from performing the adsorption of a solute. A few papers (Cromwell et al., 2006; Shukla and Hinckely, 2008) discuss the formation of aggregates in bioprocesses that can potentially lead to resin fouling and measures that can be taken to improve the purity of Protein A eluate product fractions. Although resin fouling is a practical problem in mAb purification, no specific information is available on the fouling mechanism of ion exchange resins used in a flow-through mode following a Protein A capture step.

As a working hypothesis we can consider two extreme cases, “homogeneous fouling” and “surface fouling”, as sketched in Fig. 2.1. In “homogeneous fouling” (Fig. 2.1, left), the foulant is assumed to be protein that unfolds and coats the inner adsorbent surfaces preventing binding of the solute of interest. On the other hand, in “surface fouling” (Fig. 2.1, right), the foulant is aggregated protein, which is irreversibly bound on the outer surface of the particle blocking access to the underlying matrix. In the latter case, the effect of fouling can be thought of as an additional resistance to transport that slows down the kinetics of adsorption. Figure 2.2 shows another depiction of surface fouling. The dotted line represents the external boundary layer through which transport is described by eq. 2.1.

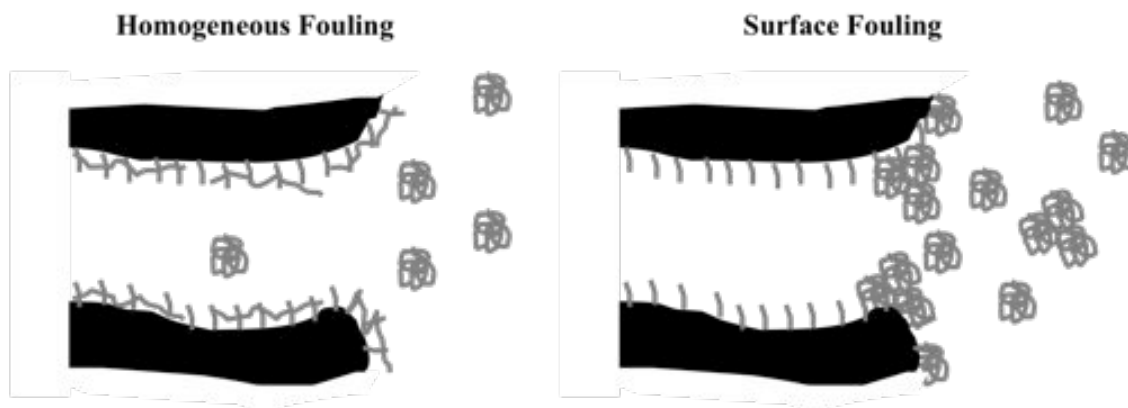


**Figure 2.1.** Sketches of “homogeneous fouling” and “surface fouling” mechanisms of a tentacle type resin where the black areas represent the resin backbone, the grey strands represent the functionalized tentacles and the aggregates represent the foulant species.

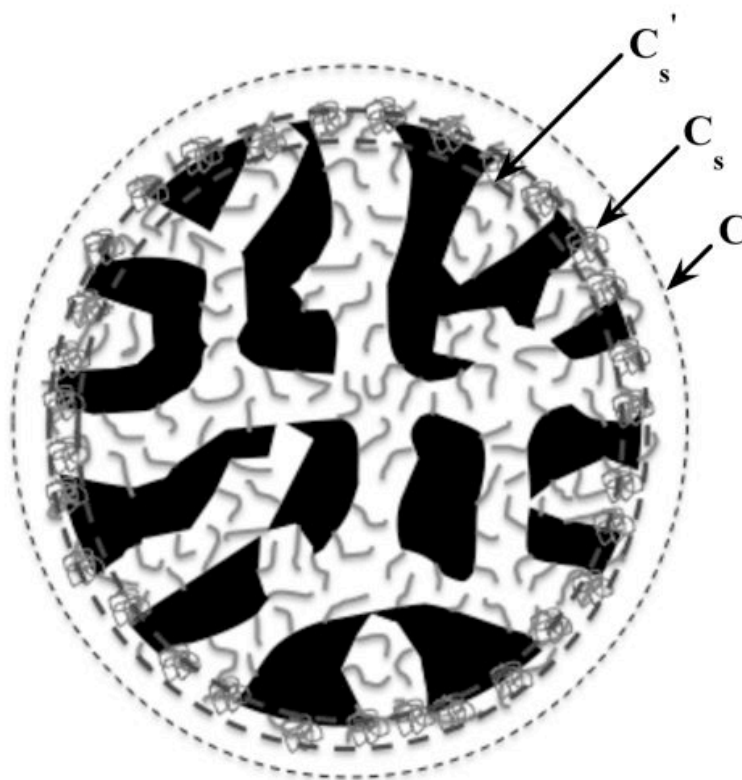


**Figure 2.2.** Depiction of the additional film resistance created by surface fouling where the dashed line indicates the foulant layer and the dotted line represents the boundary layer outside the resin particle.

The mass transfer flux through the fouled layer can be written as:

$$J = \frac{D_e'}{\delta'} (C_s - C_s') \quad (2.11)$$

where  $\delta'$  is the thickness of the fouled layer,  $D_e'$  is the effective pore diffusivity through the fouled layer and  $C_s'$  is the concentration on the particle side of the fouled layer. Since these resistances are in series, an overall mass transfer coefficient for the fouled resin,  $(k_f)_{fouled}$ , can be defined by the following equation:

$$\frac{1}{(k_f)_{fouled}} = \frac{1}{(k_f)_{clean}} + \frac{\delta'}{D_e'} \quad (2.12)$$

Where  $(k_f)_{clean}$  is the mass transfer coefficient of the clean resin (obtained from  $Sh$  as described in Section 2.1.1).  $D_e'$  must be related to the physical characteristics of the fouled layer. This value can be very small, or even zero, when a very compact fouled layer is formed.

## Chapter 3. Experimental Materials and Methods

### 3.1 Materials

The adsorbent used in this work is Fractogel TMAE HiCap (m) from EMD Chemicals. The resin has a polymethacrylate backbone with positively charged polymer chains, referred to as “tentacles” that serve as surface extenders (EMD Chemicals, 2011). According to the manufacturer specifications, the resin has particle diameters in the range of 40-90  $\mu\text{m}$  with a matrix pore radius of 40 nm. The resin contains the quaternary ammonium ion trimethylaminoethyl (TMAE) as functional groups and is, thus, a strong anion exchanger. The addition of the tentacles increases the accessibility to the functional groups by oppositely charged protein molecules thereby increasing the protein adsorption capacity. Moreover, the tentacles can affect protein transport through electrostatic interactions.

A resin sample (Sample A) was obtained from EMD Chemicals while another (Sample B) was obtained from Pfizer, Inc. (Andover, Massachusetts, USA). Both of these samples were of the virgin resin. A third sample of the Fractogel TMAE resin, denoted as Sample D was also obtained from Pfizer. This sample was fouled by its use in a polishing process step and was obtained in a pre-packed Omnifit column with dimensions of 0.66 cm x 12 cm.

All experiments conducted with these resin samples were in a TRIS buffer prepared using ACS grade chemicals from Fisher Scientific. Solutions containing a 50 mM chloride concentration were prepared by dilution of 1 M HCl with distilled-deionized water. The pH of the solution was then adjusted to the desired value of 8.5 by adding tris(hydroxymethyl)aminomethane (TRIS). This buffering species has a pKa of 8.06 and a buffering range of 7.0-9.0 (Beynon and Easterby, 1996). All experiments were performed at room temperature ( $22\pm 2^\circ\text{C}$ ).

Micrographs were taken at 100x magnification in order to obtain the particle size distribution of each resin sample. Image J (version 1.44) was used to obtain the diameter of the particles by setting the circularity and size. This open domain program, downloadable from <http://rsbweb.nih.gov/ij>, has the capability of measuring particles that are not in direct contact with one another by globalizing a scale of known distance to pixels. Figure 3.1 shows the particle size distributions for Samples A and B. The corresponding volume-average particle diameters were determined to be  $d_p=70$  and  $72 \mu\text{m}$  for Samples A and B, respectively. It is obvious that there is no substantial difference between the two samples.

The bovine serum albumin, BSA (MW~65,000, pI~5), used in these studies was obtained from Sigma Chemical Co. (St. Louis, MO) with a manufacturer's reported purity greater than 99% based on agarose gel electrophoresis. However, the samples were found to contain a substantial amount of higher molecular weight species (likely BSA oligomers). Thus, prior to experimental use, the BSA was purified by size exclusion chromatography with a Superdex™ 200 10/300 GL column from GE Healthcare. The SEC separation was conducted in TRIS buffer at a flow rate of 0.5 mL/min with 0.5 mL samples injected at a concentration of ~5 mg/mL using an AKTA Explorer 10 from GE Healthcare. A purified monomer fraction was collected between 12.9 and 14.5 mL. The results are shown in Fig. 3.2, where the purified product is compared to crude BSA.

The second model protein used was Thyroglobulin, TG, from bovine thyroid (MW~670,000, pI~5), also obtained from Sigma, with a manufacturer reported purity of >90% based on agarose gel electrophoresis. This protein was used in the as-received form.

Glucose, dextran probes and un-retained proteins were used for inverse size exclusion chromatography (iSEC). The iSEC standards used ranged from glucose (180 Da) to a dextran

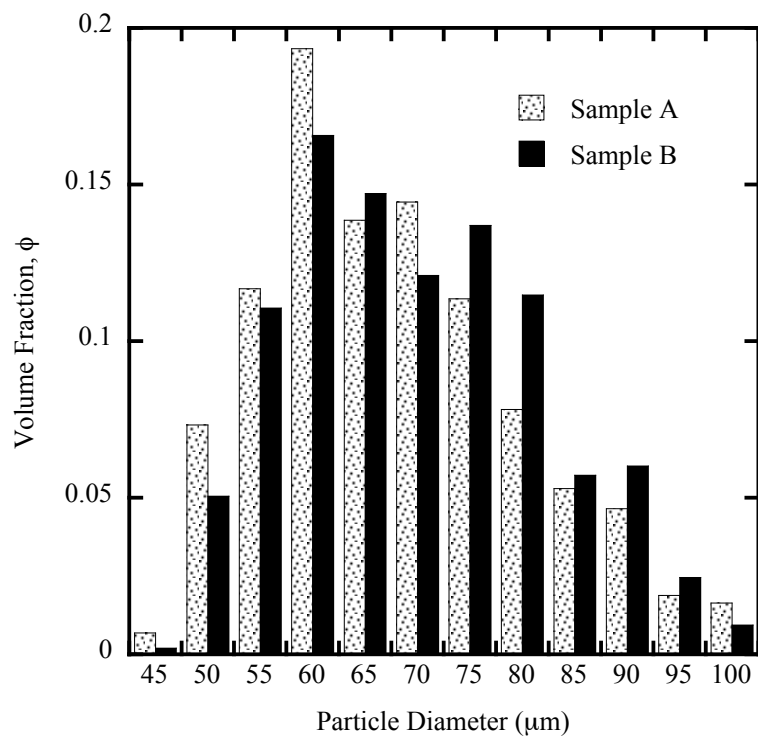


**Figure 3.1.** Particle size distributions for Fractogel TMAE HiCap (m) Samples A and B.

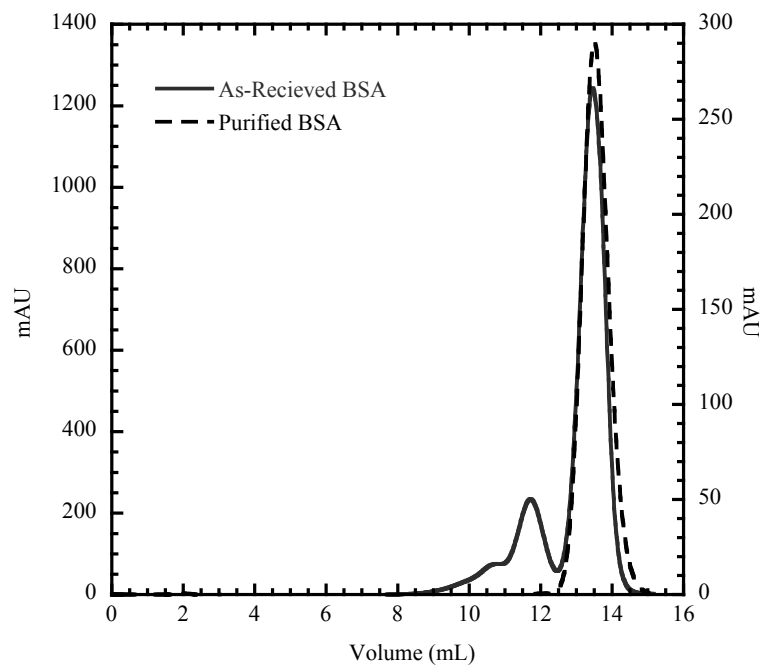


**Figure 3.2.** Size exclusion chromatography analyses for as-received and purified BSA.

with 2,000 kDa molecular mass and were obtained from Fisher Scientific and GE Healthcare. Lysozyme (MW~15,000),  $\alpha$ -Chymotrypsinogen (MW~25,000), and a monoclonal antibody (MW~150,000) were used under un-retained conditions in high salt buffer solutions to eliminate electrostatic interactions with the resin. Lysozyme from chicken egg white and  $\alpha$ -Chymotrypsinogen A Type II from bovine pancreas were obtained from Sigma Chemical Co. (St. Louis, MO). The monoclonal antibody was available in our laboratory.

Fluorescent labeling of proteins was obtained using Rhodamine Red and Rhodamine Green succinimidyl esters obtained from Invitrogen (Grand Island, NY). The properties of each label can be found in Table 3.1.

**Table 3.1.** Properties fluorescent dyes used in this work.  $\epsilon$  is the extinction coefficient at the emission maxima.

Dye	Formula	MW	Excitation/Emission maxima (nm)	$\epsilon$ (cm <sup>-1</sup> M <sup>-1</sup> )
Rhodamine Red	C <sub>37</sub> H <sub>44</sub> N <sub>4</sub> O <sub>10</sub> S <sub>2</sub>	767	570/590	120,000
Rhodamine Green	C <sub>25</sub> H <sub>18</sub> ClN <sub>3</sub> O <sub>7</sub>	621	505/527	68,000

## 3.2 Methods

### 3.2.1 Inverse size exclusion chromatography

Inverse size exclusion chromatography was used to determine the accessible pore radius of Fractogel TMAE HiCap. For this purpose, the resin samples were flow-packed into Tricorn 0.5 cm x 5 cm columns using a 50 mM Cl<sup>-</sup> TRIS buffer at pH 8.5 containing 2 M NaCl with an ÄKTA Explorer 10 system (GE Healthcare) using Unicorn operating software. The resin manufacturer's recommended maximum superficial velocity of 800 cm/hr was used to pack the columns. This is equivalent to a flow rate of 2.6 mL/min for the chosen column size. The actual iSEC experiments were carried out using a Waters HPLC system (Model e2695) with a refractive index detector. The column was first equilibrated with the working buffer before a

series of 20  $\mu\text{L}$  injections of 5 mg/mL glucose and dextran standards were made and eluted at a flow rate of 0.5 mL/min. For each standard, the first moment, or mean retention volume, was then calculated from the eluted peaks and compared to each probe's hydrodynamic radius to determine the average pore radius,  $\overline{r_{pore}}$ . Corrections were made in the first moment calculation to account for the extracolumn volume, which was obtained by making injections to the same column without the packing and with the column ends adapted and pushed against each other. Hydrodynamic radii,  $r_s$ , of the dextran standards were estimated from the correlation of Hagel et al. (1996), which is given by

$$r_s = 0.0271 \cdot M_p^{0.498} \quad (1)$$

where  $M_p$  is the molecular mass of the dextran sample (Hagel et al., 1996). The same set-up and protocol were used for the un-retained proteins, with the working buffer for all of the experiments being 1 M NaCl 50 mM Cl<sup>-</sup> TRIS pH 8.5 to suppress interaction with the resin matrix. Table 3.2 summarizes the hydrodynamic radii and molecular weight of the iSEC probes under consideration.

**Table 3.2.** Dextran standards and proteins used in iSEC experiments.

<b>Dextran</b> <b><math>M_p</math> (kDa)</b>	<b><math>r_s</math></b> <b>(nm)</b>	<b>Protein</b>	<b><math>M_p</math></b> <b>(kDa)</b>	<b><math>r_s</math></b> <b>(nm)</b>
2000	37.2	mAb	150	5.0
500	18.6	$\alpha$ -Chymotrypsinogen	25	2.1
70	7	Lysozyme	15	1.7
40	5.3			
10	2.6			
Glucose	0.4			

### 3.2.2 Transmission electron microscopy

Transmission electron microscopy was used to observe the internal structure of the adsorbent particles. For this purpose, the particles were embedded in an acrylic resin (LRWhite, obtained from London Resin Company, Ltd., London, United Kingdom). This was achieved by first dehydrating the particles with multiple washes of ethanol-water mixtures with increasing ethanol concentrations, with the last wash being anhydrous ethanol. Following this step, the particles were then washed with LRWhite-ethanol solutions beginning with a 1:1 (v/v) ratio of LRWhite to ethanol, increasing to a 2:1 ratio, and ending with 100% LRWhite. The resin samples were then cured for 24 hours at 45°C, ultramicrotomed into 80 nm sections, and imaged using a JEOL 100 CX transmission electron microscope. Personnel at the University of Virginia's Advanced Microscopy facility ultramicrotomed and sectioned the samples.

#### 3.2.2.1 Effect of column compression

TEM was also used to examine the effects of mechanical compression of the column on the packed bed structure. These studies were carried out by packing the resin in a modified 1 mL syringe (Tuberculin Slip Tip Syringe), made by Becton, Dickinson and Company (Franklin Lakes, New Jersey), that was fitted with a polypropylene frit and a custom designed aluminum plunger. The plunger, visible in Fig. 3.3 comprised a 2 mm inner flow channel and two O-rings to prevent leakage. The resin samples were first gravity-packed into the syringe using a 50/50 slurry. A second frit was then placed on top of the settled bed followed by insertion of the plunger. The assembly was then placed in the set-up illustrated in Fig. 3.3 where a micrometer screw could be used to exert a specified degree of mechanical compression. Mechanical compressions of 10, 17, and 30% were used. After compression, the column was embedded in LRWhite resin. In this case, a pump (LabAlliance<sup>TM</sup> Series II) was used to dehydrate the resin

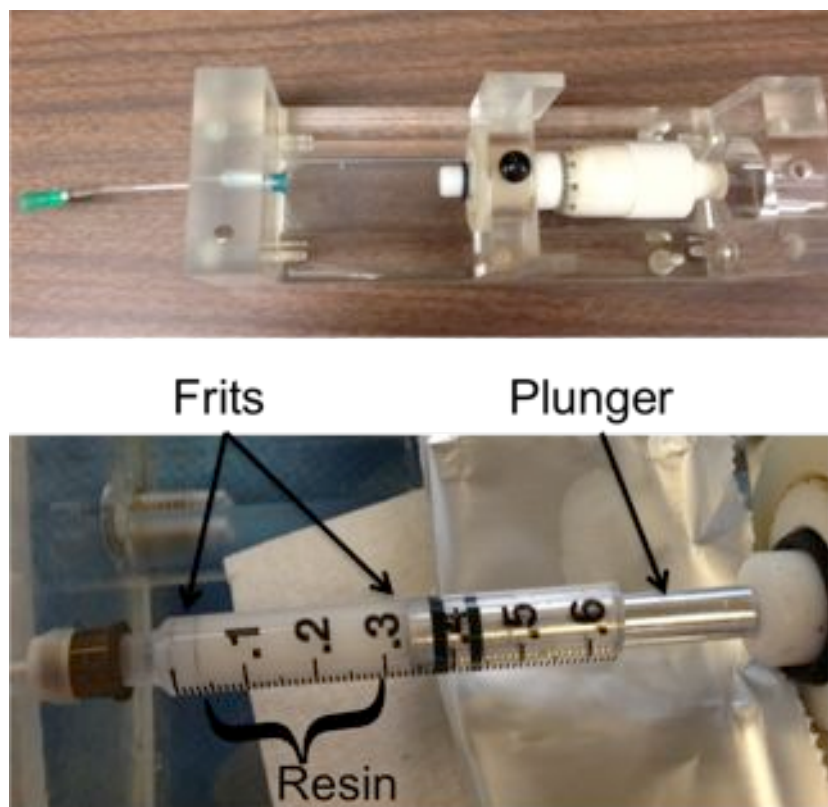


**Figure 3.3.** Images of equipment used for column compression studies.

using increasing ethanol concentrations at a flow rate of 0.2 mL/min. A syringe was then used to flow ethanol-LRWhite solutions with increasing LRWhite content (from 50% to 100% LRWhite) at a flow rate of about 0.5 mL/min. While remaining in the compression set-up, the column was then placed into a 45°C oven to cure for 24 hours. The cured sample was removed from the syringe and taken to the Advanced Microscopy facility to be ultramicrotomed and sliced into 0.5  $\mu\text{m}$  thick sections to be dried onto microscope slides. The slides were then stained with Electric Blue stain for optical imaging by adding concentrated, 0.22  $\mu\text{L}$  filtered stain solution to the microscope slide and allowing to adsorb for 15 minutes before removing with deionized water. This was repeated several times until the particles were visible using optical microscopy. Image J was used to determine the particle area for each particle within a designated section; from this the extraparticle void fraction could be determined.

### **3.2.2.2 Fouling of packed mini-column**

A mini-column was gravity packed with Fractogel TMAE Sample B and mechanically compressed to 30% using the micrometer adjuster. The mini-column was then subjected to multiple load, wash, elute, and clean in place steps according to a proprietary protocol mimicking the actual process. A pump was used to control the flow rate of the various solutions used in these steps. After completing these steps, the column was dehydrated using an increasing ethanol gradient at a flow rate of 0.2 mg/mL. The column was then embedded with LR White using the protocol described in the previous section.

### **3.2.3 Protein binding capacity studies**

The resin's binding capacity for BSA and Thyroglobulin was determined from batch experiments at 1.5 and 24 hours. For this purpose, the resin was buffer exchanged into the working buffer and then centrifuged in a micro-centrifuge filter tube to remove the extraparticle

fluid. The micro-centrifuge was set at 5000 rpm for five minutes and run for two cycles with the excess fluid removed in between each cycle. The density of the hydrated resin was then determined to be 0.97 g/mL with a pycnometer. This value was used to convert the resin mass,  $M_{resin}$ , determined by weighing to the volume of particles,  $V_{resin}$ . The hydrated, filter-centrifuged particles were then placed in 1.5 or 3 mL vials containing protein solutions with different initial concentrations  $C_0$ , and gently rotated end-over-end in a rotator at a few rpm. Samples of the supernatant liquid were then taken after 1.5 and 24 h of rotation and analyzed spectrophotometrically with a NanoVue™ UV spectrophotometer (GE Healthcare). Extinction coefficients of 0.67 and 1.04 M<sup>-1</sup> cm<sup>-1</sup> for BSA and Thyroglobulin, respectively, were used to determine the residual protein concentration,  $C$ . Finally, the following material balance was used to determine the adsorbed protein concentration (Stone and Carta, 2007):

$$q = \frac{V}{V_{resin}}(C_0 - C) \quad (3.1)$$

where  $V$  is the protein solution volume,  $V_{resin}$  is the volume of hydrated particles, and  $C_0$  and  $C$  are the initial and final protein concentrations in solution, respectively.

### 3.2.4 Batch adsorption kinetics

The kinetics of protein adsorption was determined from batch uptake measurements made with the resin particles suspended in a protein solution in a vessel mixed with a paddle stirrer at about 300 rpm. A Cole-Parmer peristaltic pump recirculated the solution through a UV detector at 280nm (GE Healthcare, Model UV1) in order to determine the protein concentration as a function of time (Carta et al., 2005). A stainless steel 5- $\mu$ m pore filter was used to prevent resin particles from entering the UV detector. A schematic of the stirred-batch apparatus can be seen in Fig. 3.4. The volume of the protein solution was the same for all experiments (20 mL) while the protein concentration was varied between 0.2 and 2 mg/mL for both BSA and

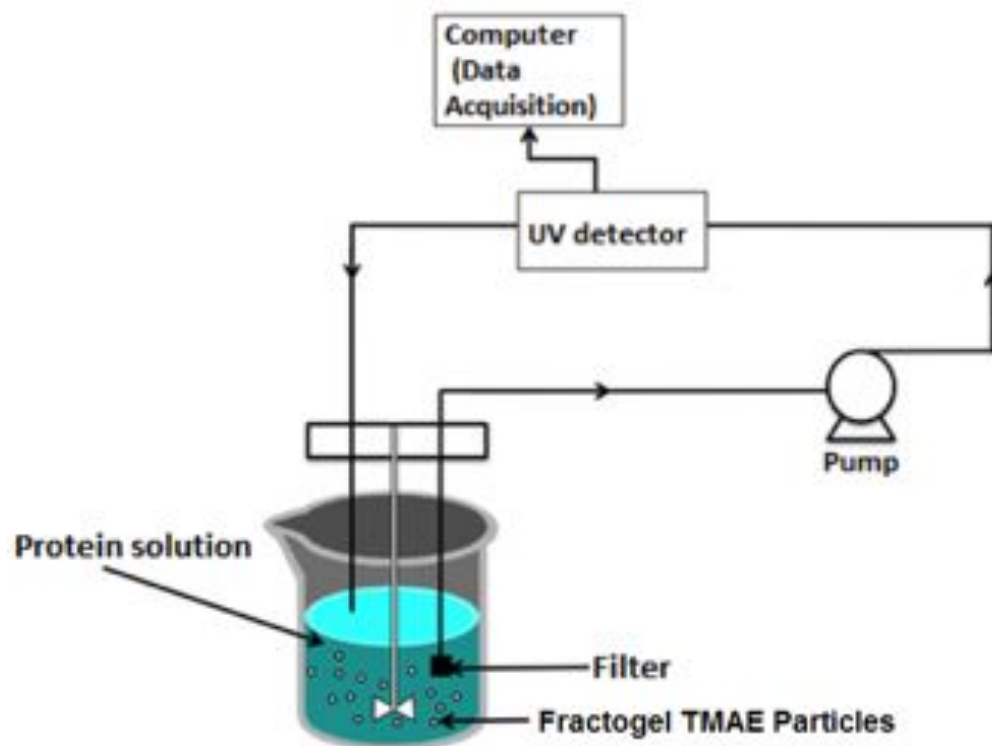


**Figure 3.4.** Schematic of stirred-batch apparatus.

Thyroglobulin. The amount of resin used in each experiment was adjusted, based on knowledge of the binding capacity, to achieve a 50% change of the protein concentration over the course of the experiment. A mass balance was used to determine the amount of protein adsorbed by the resin at each time. The final protein concentration was checked by allowing the solution to settle once at equilibrium and obtaining a final protein concentration by sampling and determining the final UV absorbance off-line with the NanoVue<sup>TM</sup> spectrophotometer.

A rate model, assuming that pore diffusion within the particles in series with an external film mass transfer resistance controls the adsorption kinetics, was used to extract an effective apparent pore diffusivity from the data by fitting the batch adsorption curves to calculated ones. The model, which assumes that the protein adsorption isotherm is rectangular and which takes into account the particle size distribution of the resin, is given in Stone and Carta (2007). The external film mass transfer coefficient was estimated based on a Sherwood,  $Sh = k_f \bar{d}_p / D_0$ , equal to 30 based on previous determinations for similarly sized particles in the same stirred vessel and under similar agitation conditions (Armenante and Kirwan, 1989).

### **3.2.5 Confocal laser scanning microscopy**

Confocal laser scanning microscopy was used to examine the movement of adsorbed protein within individual Fractogel TMAE particles. This information complements the batch uptake kinetics measurement, but is expected to provide greater insight regarding transport mechanisms. In CLSM, the concentration of a fluorophor present in a transparent three-dimensional matrix is obtained by collecting the fluorescence emitted from a thin (0.5 – 1.5  $\mu\text{m}$ ), optical section of the matrix. In order to utilize this technique to measure protein adsorption in chromatographic particles, three major requirements must be met:

1. The protein must be conjugated with a fluorescent dye and the dye must not interfere with protein binding to the resin;
2. The concentration of the dye-conjugated protein within the particle must be sufficiently low to prevent significant absorption of the excitation light; and
3. The particles must be sufficiently transparent to allow excitation and emitted light to pass through.

These three requirements were met as discussed in the following sections.

### **3.2.5.1 Fluorescent labeling of proteins**

Fluorescent conjugates of purified BSA monomer and of Thyroglobulin were obtained with Rhodamine Red<sup>TM</sup>-X and Rhodamine Green<sup>TM</sup>-X succinimidyl ester amine-reactive dyes, respectively. As shown previously in Table 3.1, these dyes have non-overlapping excitation and emission maxima, so that they can also be used in two-component adsorption experiments. Protein conjugation to these dyes was conducted using a modified protocol based on the dye manufacturer recommended procedure. Protein solutions of approximately 10 mg/mL were prepared in a 500 mM sodium bicarbonate solution with pH adjusted to 8.5 using sodium carbonate. Partial deprotonation of primary amine groups occurs at this slightly alkaline pH allowing the reaction to take place between the protein and the amine reactive dye. The dye-to-protein molar ratios used were 1:3 and 3:1 for BSA and Thyroglobulin, respectively. The molar ratio is greater for Thyroglobulin because there are more sites for the dye to attach to due to the size of the protein; therefore, by keeping the mass ratio the same for the two proteins (the molecular mass of Thyroglobulin is about 9 times that of BSA) a similar labeling ratio is expected. Once the desired quantity of dye was added to the protein solution, the vial was wrapped in aluminum foil and mixed for 1 hour to allow the reaction to occur. A size exclusion

chromatography column was used to simultaneously buffer-exchange the protein into the working buffer and separate the labeled protein from residual dye.

The average molar labeling ratios in the SEC product fraction were determined by also measuring the absorbance at the wavelength of each dye's absorbance maximum according to the following equations:

$$C_{\text{dye}} = \frac{A_{\text{dye@}\lambda_{\text{max}}}}{\epsilon_{\text{dye@}\lambda_{\text{max}}}} \quad (3.2)$$

$$C_{\text{total protein}} = \frac{A_{280\text{nm}} - A_{570\text{nm}} CF_{280\text{nm}}}{\epsilon_{\text{protein@}280\text{nm}}} \quad (3.3)$$

$$\text{Molar labeling ratio} = \frac{C_{\text{dye}}}{C_{\text{total protein}}} = \frac{C_{\text{labeled}}}{C_{\text{total protein}}} \quad (3.4)$$

where  $A$  is the absorbance in a 1 cm cell and  $\epsilon_{\text{dye}}$  and  $\epsilon_{\text{protein}}$  are the dye and protein molar extinction coefficients, respectively. The former were 120,000 and 68,000  $\text{M}^{-1}\text{cm}^{-1}$  for the Red and Green dyes, respectively, as reported by the dye manufacturer, while the latter were found to be 44,000 and 690,000  $\text{M}^{-1}\text{cm}^{-1}$  for BSA and Thyroglobulin, respectively (Tarutani and Shulman, 2002; Thermo Scientific, 2008). A correction factor,  $CF_{280\text{nm}}$ , is needed to account for the absorption of dye at a wavelength of 280 nm for the red and green dyes. Correction factors of 0.17 and 0.28 correspond to the Red and Green dyes respectively. All  $A$  measurements were made with the Nanovue<sup>TM</sup> instrument. Total protein concentrations in the SEC product fractions were between 4 and 5 mg/mL while the molar labeling ratios were 0.10 and 1.3 mol dye/mol of protein for BSA and Thyroglobulin, respectively.

Linear gradient elution (LGE) experiments were conducted to determine the effects, if any, of fluorescent labeling on protein binding (Perez et al., 2011). Since chromatographic retention in LGE is sensitive to protein surface interactions, these experiments can be used to

ascertain whether or not the fluorescently labeled protein will behave like the native one. For this purpose, the Fractogel TMAE resin (Sample B) was packed in a 0.5 x 5 cm Tricorn column operated at a flow rate of 0.5 mL/min with an AKTA Explorer 10 unit. Separate 100  $\mu$ L injections of the native protein and of the conjugated protein SEC product fraction were made and eluted with with a linear salt gradient of 0 M to 0.5 M NaCl in 20 column volumes in Tris buffer at pH 8.5. Figure 3.5 shows the results for both BSA monomer and Thyroglobulin. In comparing the results for native protein and labeled protein, there is no significant difference between the two confirming that the dye-conjugation does not alter the protein-surface interactions that are responsible for retention and, thus, binding, in the Fractogel TMAE resin.

### 3.2.5.2 Avoiding fluorescence attenuation effects

In order to minimize the amount of excitation light absorbed as the laser beam passes through the particle in a CLSM experiment, the dye-conjugated samples were further diluted with unlabeled protein to attain a final dye-to-protein molar ratio of 1:40. If a significant fraction of the excitation light is absorbed, the fluorescence emitted will be attenuated. For a fully saturated adsorbent particle, attenuation will be greater near the particle center (where the optical path is longer) than near the periphery (where the optical path is shorter) resulting in distorted images that would require extensive manipulation to correct for this effect (Dziennik et al., 2003). The extent of dilution needed can be estimated as follows. According to the Lambert-Beer's law, attenuation of monochromatic excitation light passing through an absorbing sample is described by the following equation:

$$\frac{I_{ex}}{I_{ex,0}} = \exp(-\varepsilon_{dye} \ell C_{dye}) \quad (3.4)$$

Where  $I_{ex}$  is the intensity of the transmitted light,  $I_{ex,0}$  is the intensity of the incident light,  $\ell$  is the optical path length,  $\varepsilon_{dye}$  is the dye molar extinction coefficient, and  $C_{dye}$  is the dye molar

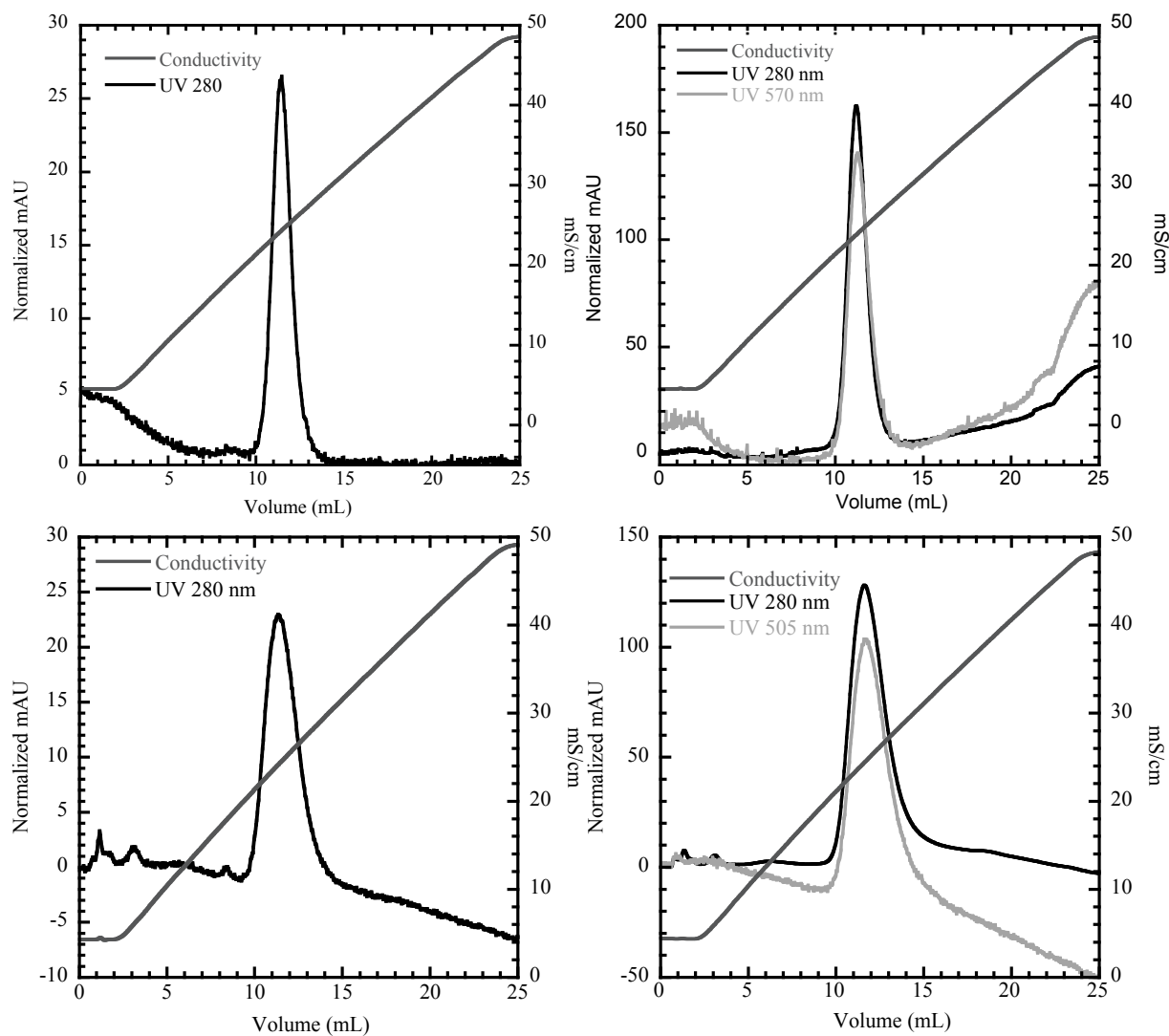


**Figure 3.5.** Gradient elution analyses of native and dye-conjugated proteins on a Fractogel TMAE column (Sample B) at pH 8.5. Top panels: BSA native and labeled using Rhodamine Red<sup>TM</sup>-X. Bottom panels: Thyroglobulin native and labeled using Rhodamine Green<sup>TM</sup>-X.

concentration in the matrix. Further, assuming that the fluorescence emitted,  $I_{em}$ , and collected by the confocal microscope objective is directly proportion to  $I_{ex}$ , we have:

$$\frac{I_{em}}{I_{ex,o}} = k_{dye} \frac{I_{ex}}{I_{ex,o}} = k_{dye} C_{dye} \exp(-\epsilon_{dye} \ell C_{dye}) \quad (3.5)$$

Figure 3.6 shows plots of this equation as a function of protein concentration in the matrix in mg/mL for BSA conjugated with Rhodamine Red ( $\epsilon_{ex}=120,000 \text{ M}^{-1}\text{cm}^{-1}$ ) at low and high labeling ratios. Since the largest Fractogel TMAE particles are around  $100 \mu\text{m}$ ,  $\ell=50 \mu\text{m}$ , which corresponds to the center of the particle, was used for these calculations. As seen from these graphs, a 1:1 dye to protein ratio would give a highly non-linear relationship between emitted light and protein concentration, resulting in substantial aberration of the images. However, a 1:40 ratio gives a linear relationship for protein concentrations up to at least 250 mg/mL. Since the actual adsorbed protein concentration in the Fractogel TMAE particles is not expected to exceed this value, the 1:40 dilution appears to be adequate. The upper limit of dilution depends, of course, on the signal-to-noise ratio of the confocal microscope set-up, which can be determined empirically.

### 3.2.5.3 Overcoming the limitation of transparency of Fractogel TMAE

Fractogel TMAE HiCap (m) is a somewhat opaque resin; therefore, substantial absorption and scattering of the emitted light occurs. However, as shown by Perez et al. (2011) this problem can be overcome by immersing the particles in a solution whose refractive index matches that of the particles. As in our prior work, sucrose solutions were used for refractive index matching (Perez et al., 2011). Various percentages of sucrose were tested to match the refractive index, with 30% sucrose being the closest match to the refractive index of Fractogel TMAE HiCap (m). A solution containing 30% sucrose has a refractive index of  $n=1.3812$

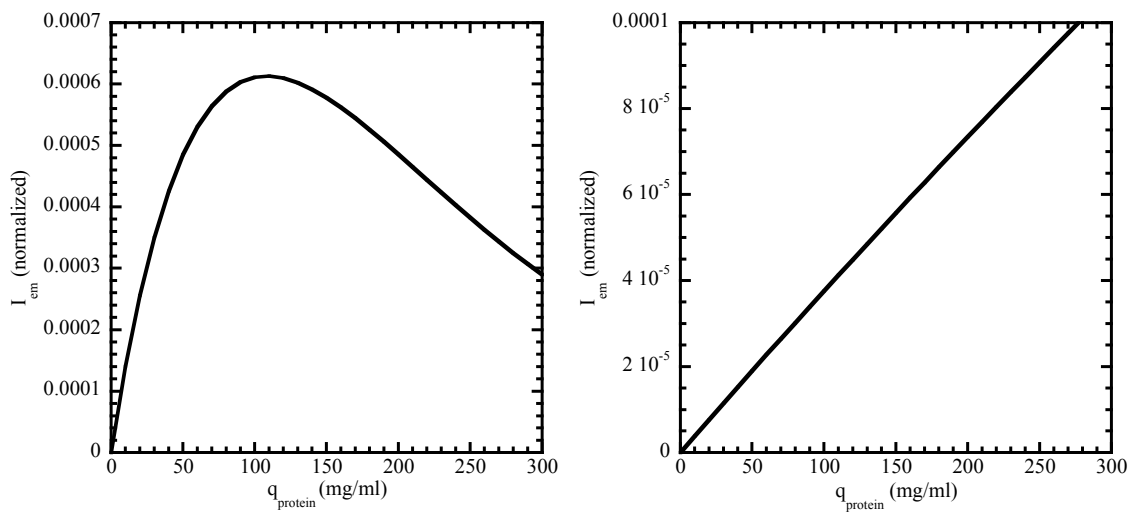


**Figure 3.6.** Predicted relationship between emitted fluorescence for Rhodamine Red labeled BSA as a function of protein concentration at the center of a 100  $\mu\text{m}$  particle for 1:1 dye-to-protein ratio (left) and 1:40 dye-to-protein ratio (right).

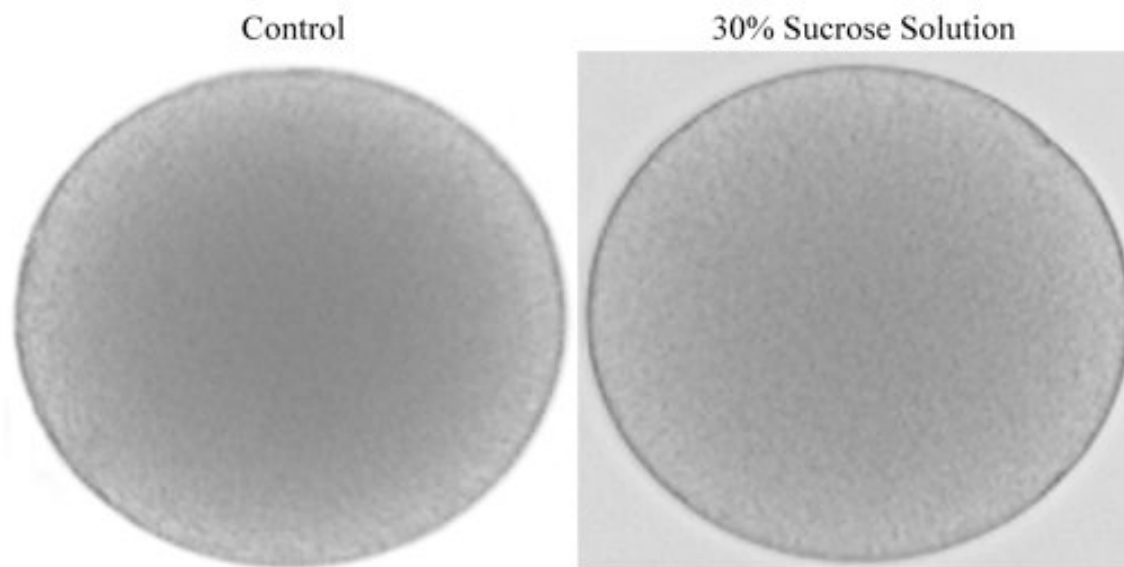
(<http://www.refractometer.pl/refraction-datasheet-sucrose>). When the resin particles are immersed in 30% sucrose solution, they appear nearly transparent when observed with a standard optical microscope as seen in Fig. 3.7.

Figure 3.8 shows the CLSM images and concentration profiles of Fractogel TMAE particles equilibrated in buffer and 30% sucrose solution. When immersed in 30% sucrose, the fluorescence intensity profile within the particle obtained for particles completely saturated with BSA is nearly flat; meaning the emission of fluorescence from the center of the particle can be collected.

#### **3.2.5.4 CLSM measurements**

Transient CLSM adsorption experiments were conducted using protein solutions with an overall 1:40 labeling ratio. Resin particles were filter-centrifuged to remove excess liquid and placed in a gently rotated vial with an excess of protein solution whose volume was chosen to ensure that the protein concentration did not vary by more than 10% during the experiment. The protein concentrations under consideration were 0.2 and 0.5 mg/mL. Small samples of the resin were removed from the vial at periodic intervals using a pipette and placed in a microfilter centrifuge tube at 10,000 rpm for 30 seconds to remove the supernatant. The particles were then immersed in 40  $\mu$ L of 30% sucrose solution and placed on a microscope slide to be imaged using CLSM. The effect of sucrose was also considered by obtaining CLSM images for particles immersed in a using a 0.2 mg/mL BSA solution containing 30% sucrose.

For two component measurements, the particles were first placed in a 0.2 mg/mL Thyroglobulin solution where images were taken periodically over 1.5 hours. The particles were then removed from the Thyroglobulin solution via centrifugation, immersed in TRIS buffer, and



**Figure 3.7.** Optical Images of Fractogel TMAE HiCap (m) when immersed in TRIS buffer solution (left) and a 30% sucrose solution (right).

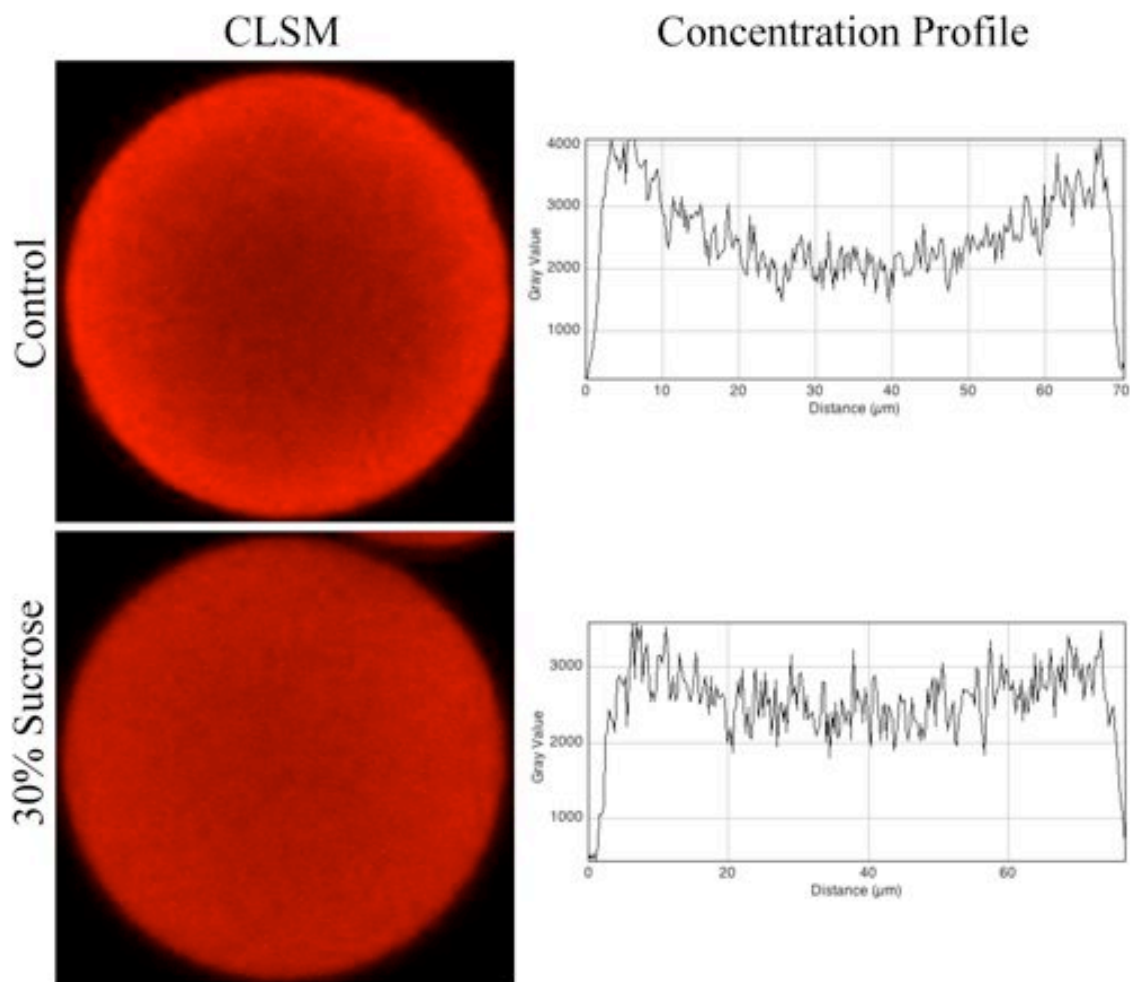


**Figure 3.8.** CLSM images and fluorescence intensity profiles of equatorial sections of Fractogel TMAE particles saturated with fluorescently labeled BSA monomer and immersed in TRIS buffer (top) and in 30% sucrose solution (bottom).

placed into a 0.2 mg/mL BSA solution. The particles were then periodically removed via centrifugation, immersed in 30% sucrose solution, and imaged using CLSM.

In all cases, vertical scanning of the particles was conducted to obtain equatorial images by finding the largest section of visible particle. Image J was then used to analyze the concentration profile by drawing a horizontal line through the center of the particle and using the software's plot profile function. The program was also used to determine the diameter of the particles by measuring the length of the horizontal line.

## Chapter 4. Results for Virgin Resin Samples

### 4.1 Inverse size exclusion chromatography

The pore size of Fractogel TMAE was obtained by analyzing the elution peaks of various molecular weight dextran standards, glucose, and three un-retained proteins. The radii of the dextrans were estimated through the correlation of Hagel et al. (1996) while the protein radii were estimated from the Stokes-Einstein equation using the diffusivities reported by Tyn and Gusek (1990). The iSEC chromatograms are shown in Fig. 4.1a and b, for the dextrans and proteins, respectively. The results show that while glucose gains access to a large fraction of the particle volume, the higher molecular mass dextrans are substantially excluded. As seen in Fig. 4.2, the retention volumes for dextrans and un-retained proteins are very similar when compared at the same  $r_s$  value indicating that the exclusion effects seen are due to size alone.

In order to determine the reproducibility of the iSEC measurements for different resin lots, the elution peaks of various weight dextrans and glucose were analyzed for both Samples A and B. Figure 4.3 shows the corresponding iSEC chromatograms using a low ionic strength buffer. Insignificant differences were seen in the elution peaks of the dextran probes when comparing the two resin lots indicating the consistency of properties of different production lots.

A moment analysis was conducted to determine the average retention volume,  $V_R$ . In turn,  $V_R$  was used to calculate a distribution coefficient,  $K_D$ , according to the following equation:

$$K_D = \frac{V_R - V_o}{V_c - V_o} \quad (4.1)$$

where  $V_o$  and  $V_c$  are the extraparticle void volume and total column volume, respectively. The former was assumed to be equal to the retention volume of dextran with 2,000 kDa molecular mass. Since larger probe molecules are excluded to a greater extent,  $K_D$  is theoretically related to the ratio of probe radius,  $r_s$ , and average pore radius,  $r_{pore}$ . In general, a complex distribution of

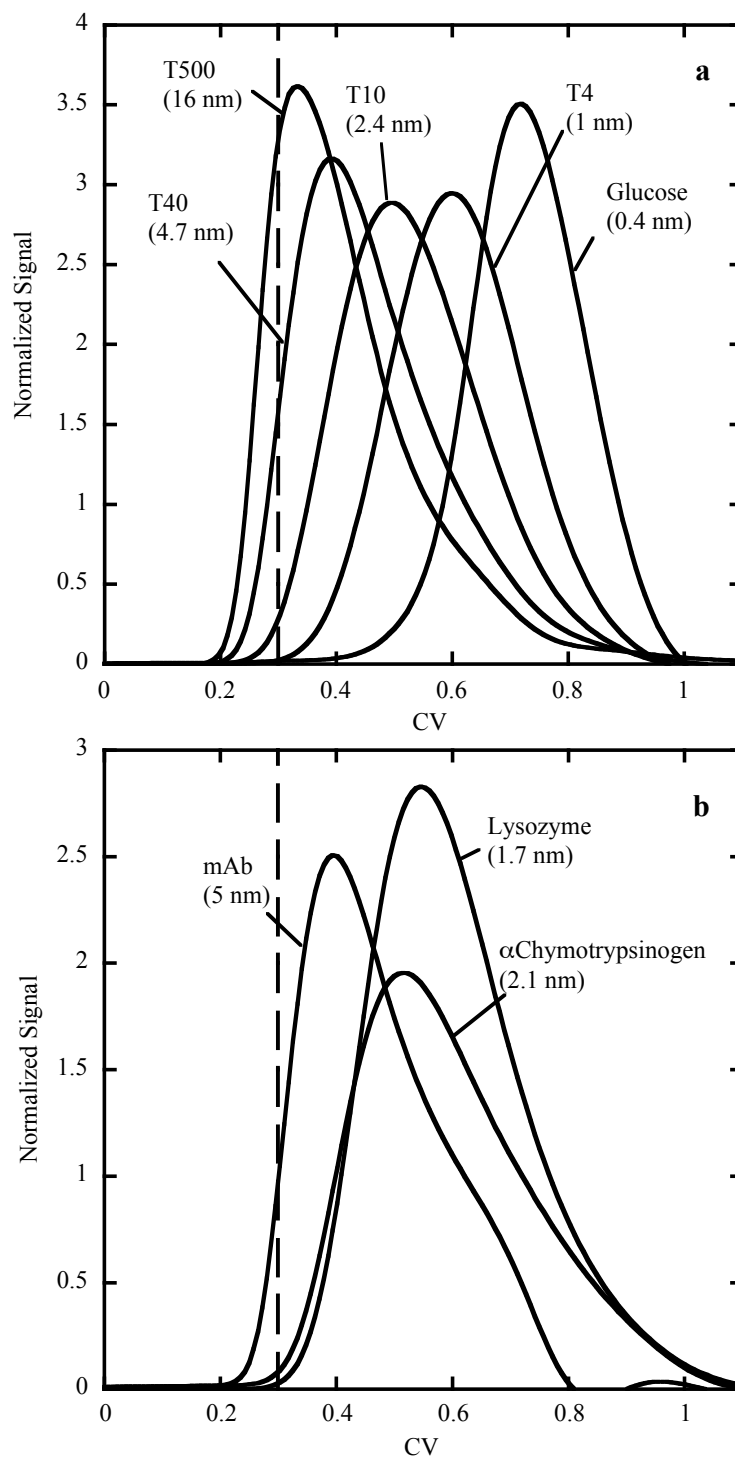


**Figure 4.1.** Inverse size exclusion results for (a) dextran standards and (b) un-retained proteins for Sample B. The dashed line represents the retention volume of T2000.

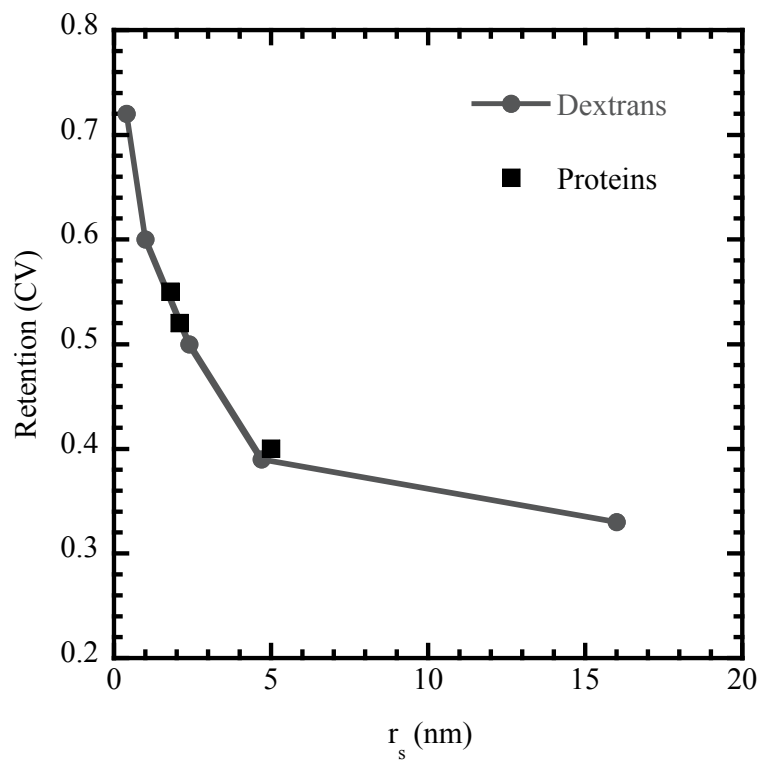


**Figure 4.2.** Comparison of iSEC retention volumes at the peak maxima as a function of molecular radius for dextran standards and un-retained proteins.

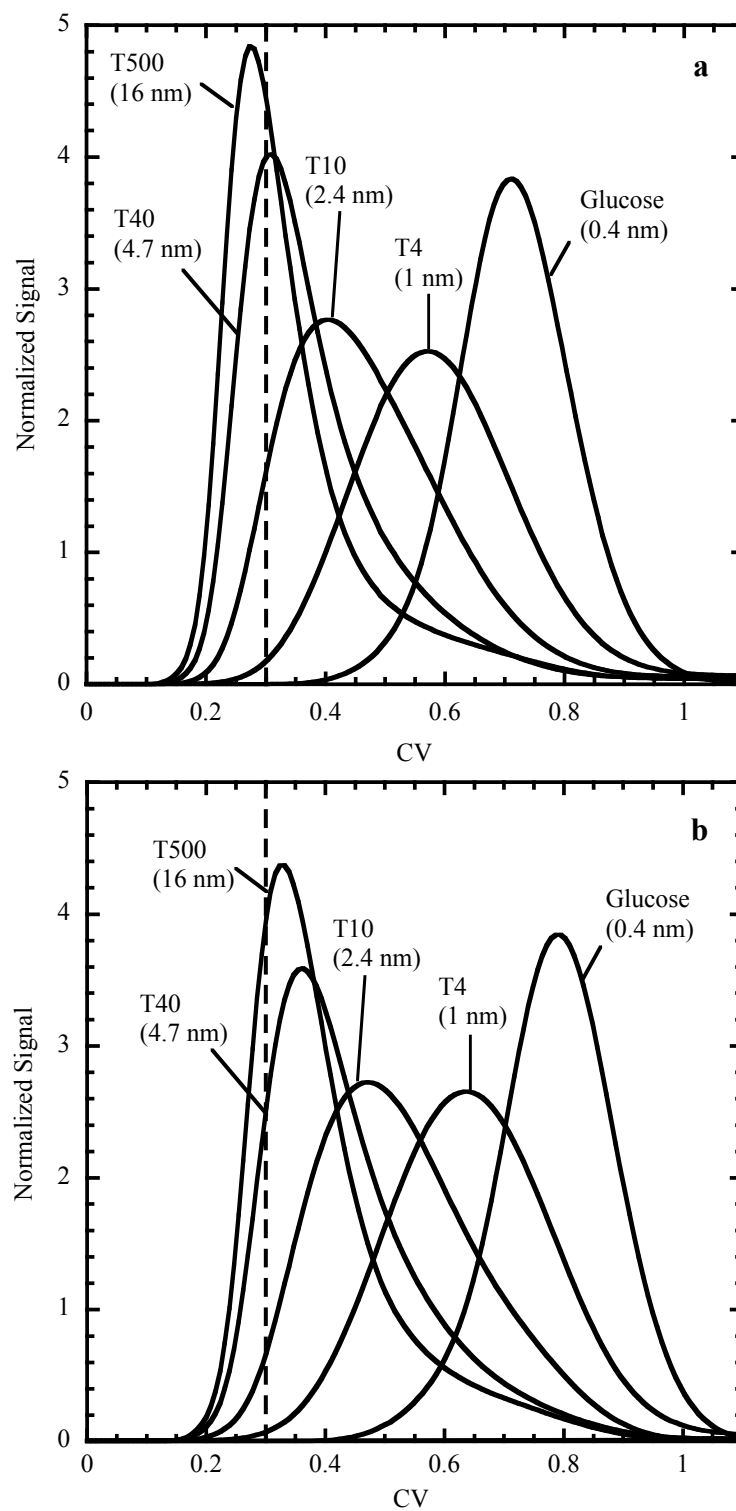


**Figure 4.3.** Inverse size exclusion results for two lots of Fractogel TMAE, (a) Sample A and (b) Sample B, where the dashed line represents the retention volume of T2000.

pore sizes can be expected. Two simple models, however, can be considered as follows. The first is obtained when all the pores are assumed to have the same size. In this case,  $K_D$  is given by:

$$K_D = \varepsilon_p \left( 1 - \frac{r_s}{r_{pore}} \right)^2 \quad (4.2)$$

The second model is obtained when the distribution is assumed to be bimodal with two characteristic pore radii  $r_{pore,M}$  and  $r_{pore,m}$ . In this case,  $K_D$  is given by:

$$K_D = \varepsilon_M \left( 1 - \frac{r_s}{r_{pore,M}} \right)^2 + \varepsilon_m \left( 1 - \frac{r_s}{r_{pore,m}} \right)^2 \quad (4.3)$$

where  $\varepsilon_M$  and  $\varepsilon_m$  are the porosities corresponding to  $r_{pore,M}$  and  $r_{pore,m}$ , respectively. The total porosity,  $\varepsilon_p$ , is thus given by:

$$\varepsilon_p = \varepsilon_M + \varepsilon_m \quad (4.4)$$

Figure 4.4 shows a comparison of eqs. 4.2 and 4.3 with the experimentally determined  $K_D$ -values. The model parameters determined by data fitting for both cases are summarized in Table 4.1. The single pore size model, eq. 4.2, could only fit the data for glucose and smaller dextrans. Thus, the higher molecular mass dextran data were omitted from the fit. However, the bimodal pore distribution model, eq. 4.3, could accurately fit the whole set of data. Since the model has many parameters, in order to fit the data, we assumed that the distribution arises because a fraction  $\varepsilon_M/\varepsilon_p$  of the large pores of the backbone matrix (which, according to the manufacturer of the resin, average in radius at 40 nm) is unfilled with tentacles and is thus accessible by the larger dextrans. The remaining fraction,  $\varepsilon_m/\varepsilon_p$ , is assumed to be filled with tentacles which appear to exclude all but the smaller dextrans. Since  $r_{pore,M}=40$  nm, the remaining parameters  $\varepsilon_M$ ,  $\varepsilon_m$ , and  $r_{pore,m}$  could be determined by data fitting.

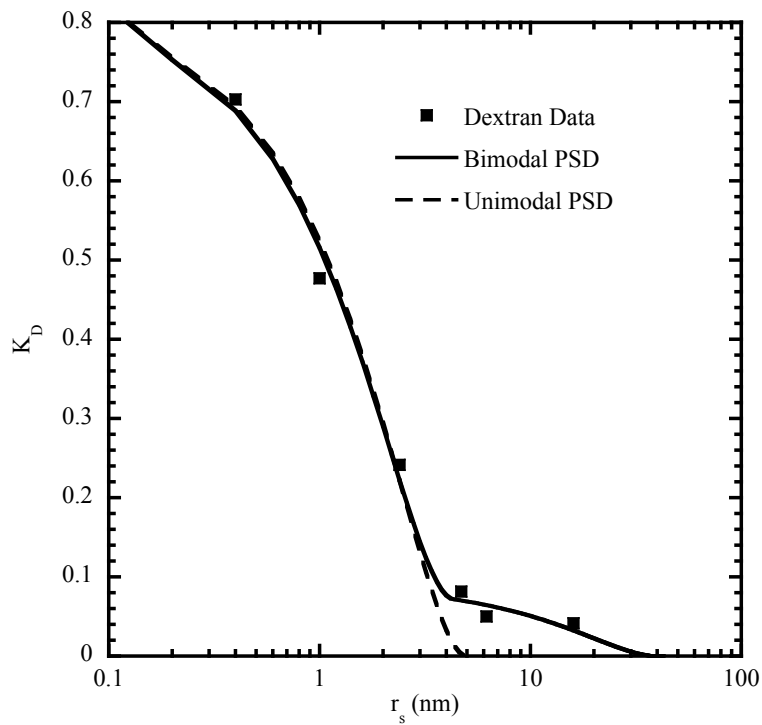


**Figure 4.4.** Comparison of experimental and theoretical  $K_D$ -values for Sample B based on unimodal and bimodal pore size distribution models.

The parameters determined in this manner are consistent with the presence of only a small fraction of large open pores. Most of the porosity is associated with a small pore size on the order of 4 to 5 nm in radius. Such pores have been found in other materials that contain charged grafted polymers for a gel-type structure within the resin matrix (Stone and Carta, 2007; Stone et al., 2009; Perez et al., 2011).

**Table 4.1.** Parameters obtained using unimodal and bimodal models for inverse size exclusion data.

<b>Unimodal</b>	$\varepsilon_p$	$r_{pore}$ (nm)			
	0.82	5			
<b>Bimodal</b>	$\varepsilon_{p, total}$	$\varepsilon_M$	$r_{pore,M}$ (nm)	$\varepsilon_m$	$r_{pore,m}$ (nm)
	0.82	0.09	40	0.74	4.3

## 4.2 Transmission electron microscopy

Transmission electron microscopy was used to observe the internal structure of the adsorbent and determine the effects of column mechanical compression. Figure 4.5 shows electron micrographs of particles from two different lots (Samples A and B) of Fractogel TMAE at different magnifications. The dark regions of the images are the resin backbone, and the light grey regions are the LRWhite embedding resin. The bright white spots within the images are due to imperfections created during embedding and sectioning. The distribution of pore size can be seen through the low magnification images (5k, Fig. 4.5 a and c) where both large and small pores are uniformly distributed across the particle radius. Higher magnification images (10k, Fig. 4.5 b and d) reveal that the particles have a microgranular structure defining a network of discrete pores. No tentacles or gel phase is visible. This is likely a consequence of the fact that their density is too low to be evident against the background of the embedding resin.

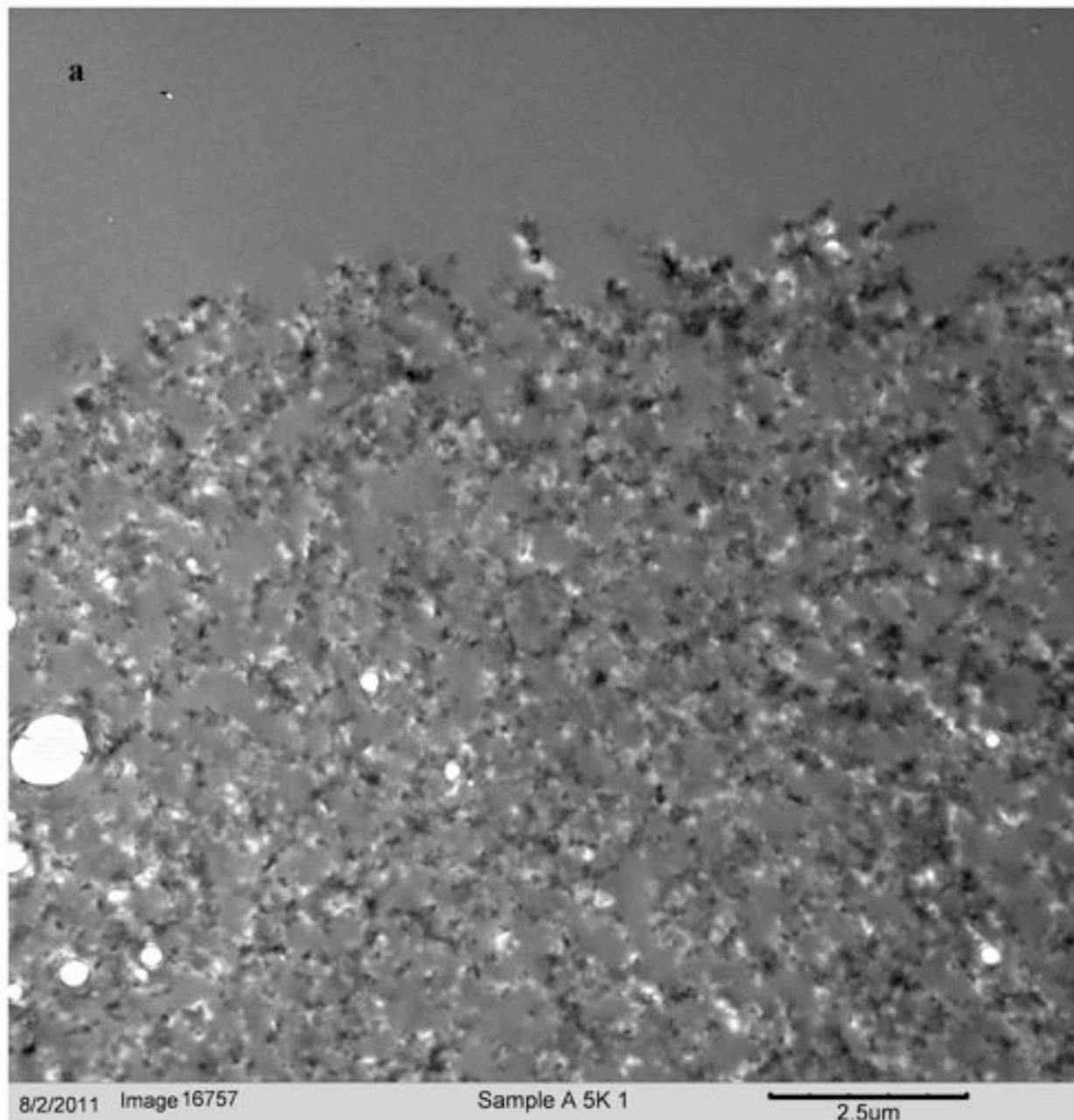


**Figure 4.5.** Electron micrographs of Fractogel TMAE HiCap (m). TEM used to obtain imaging of interior structure. (a) 5k Image of Sample A at the edge (b) 10k at the center of the particle; (c) 5k Image of Sample B at the edge, and (d) 10k at the center of the particle.

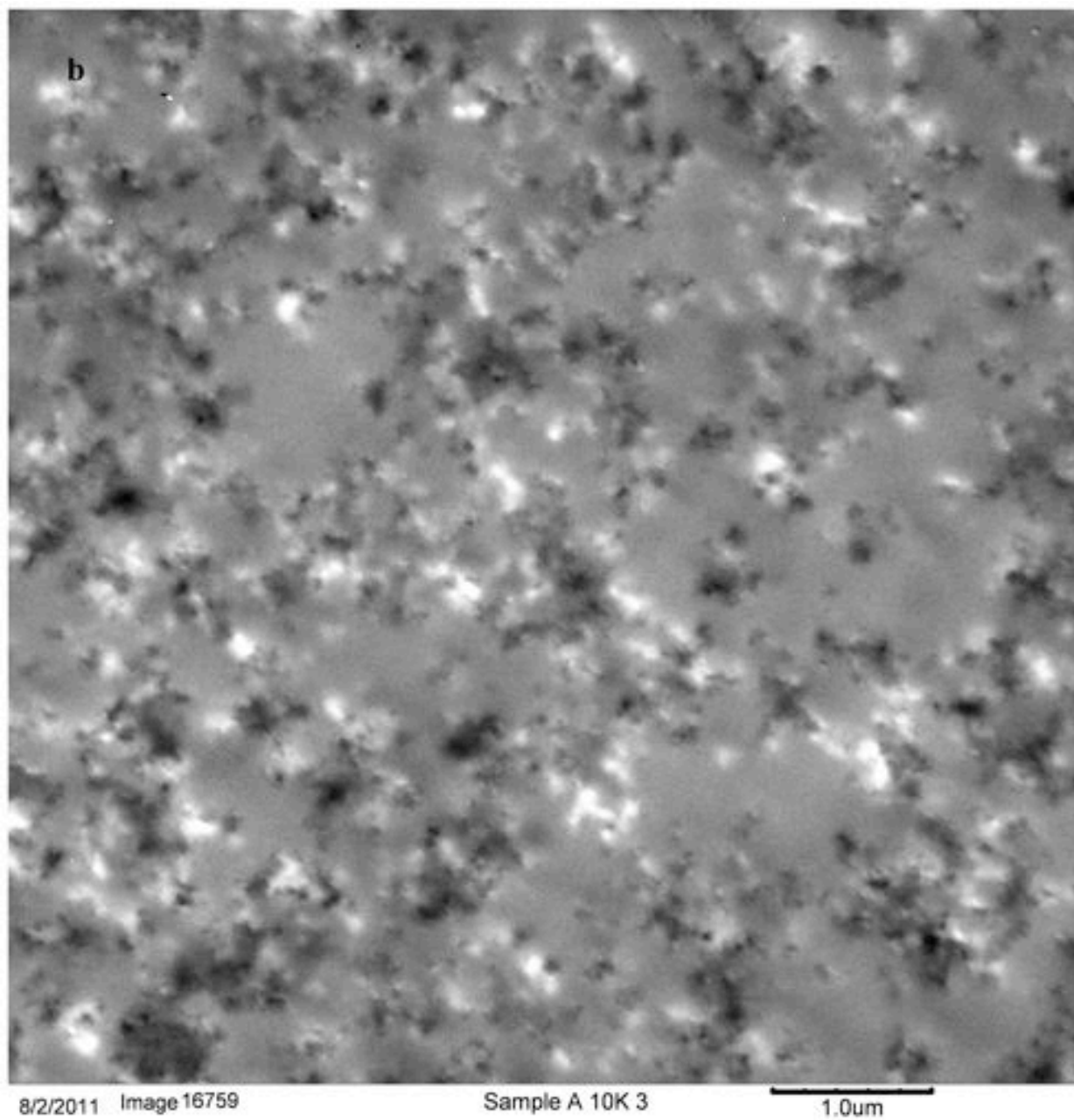


**Figure 4.5.b.**

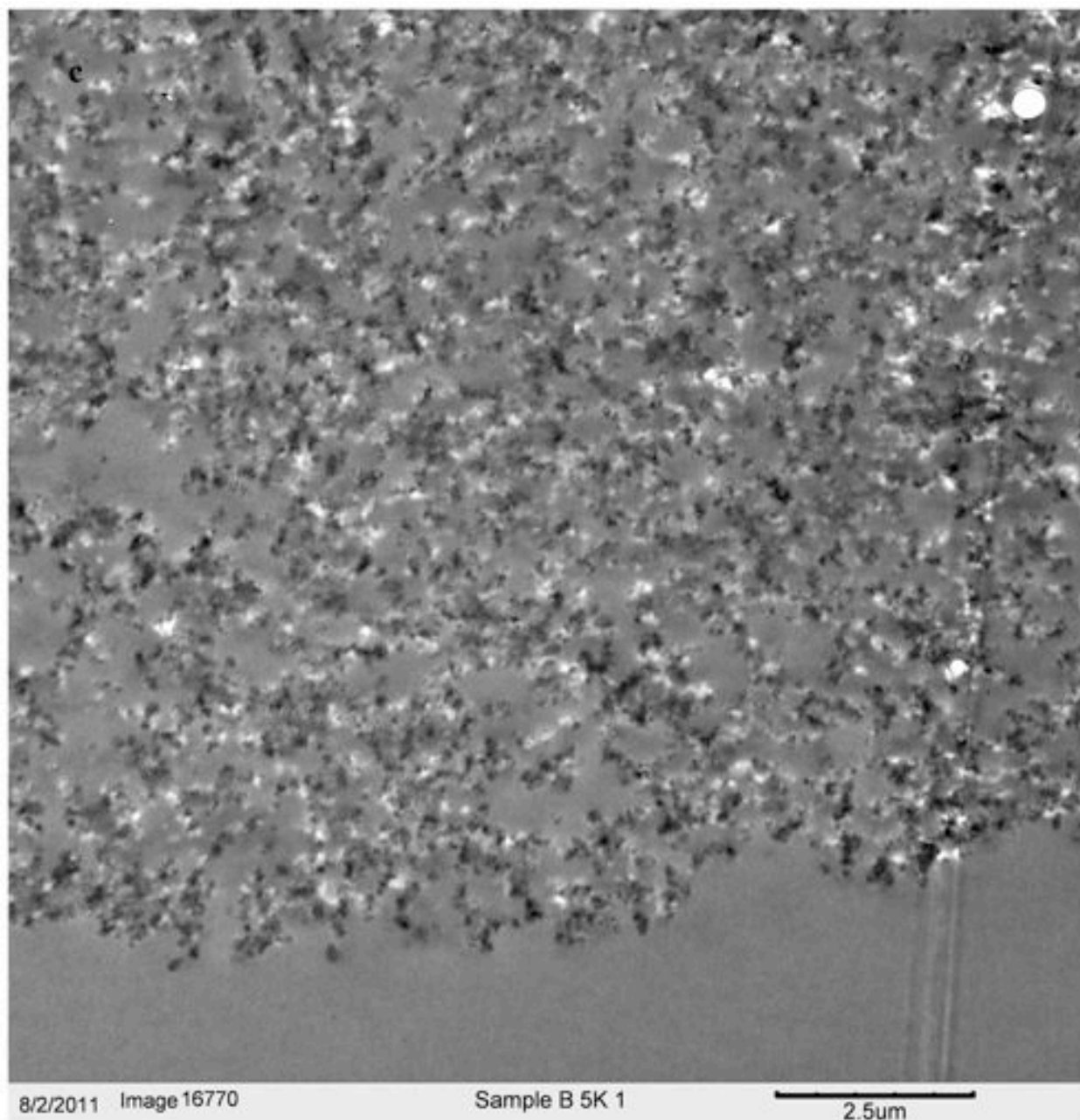


**Figure 4.5.c.**

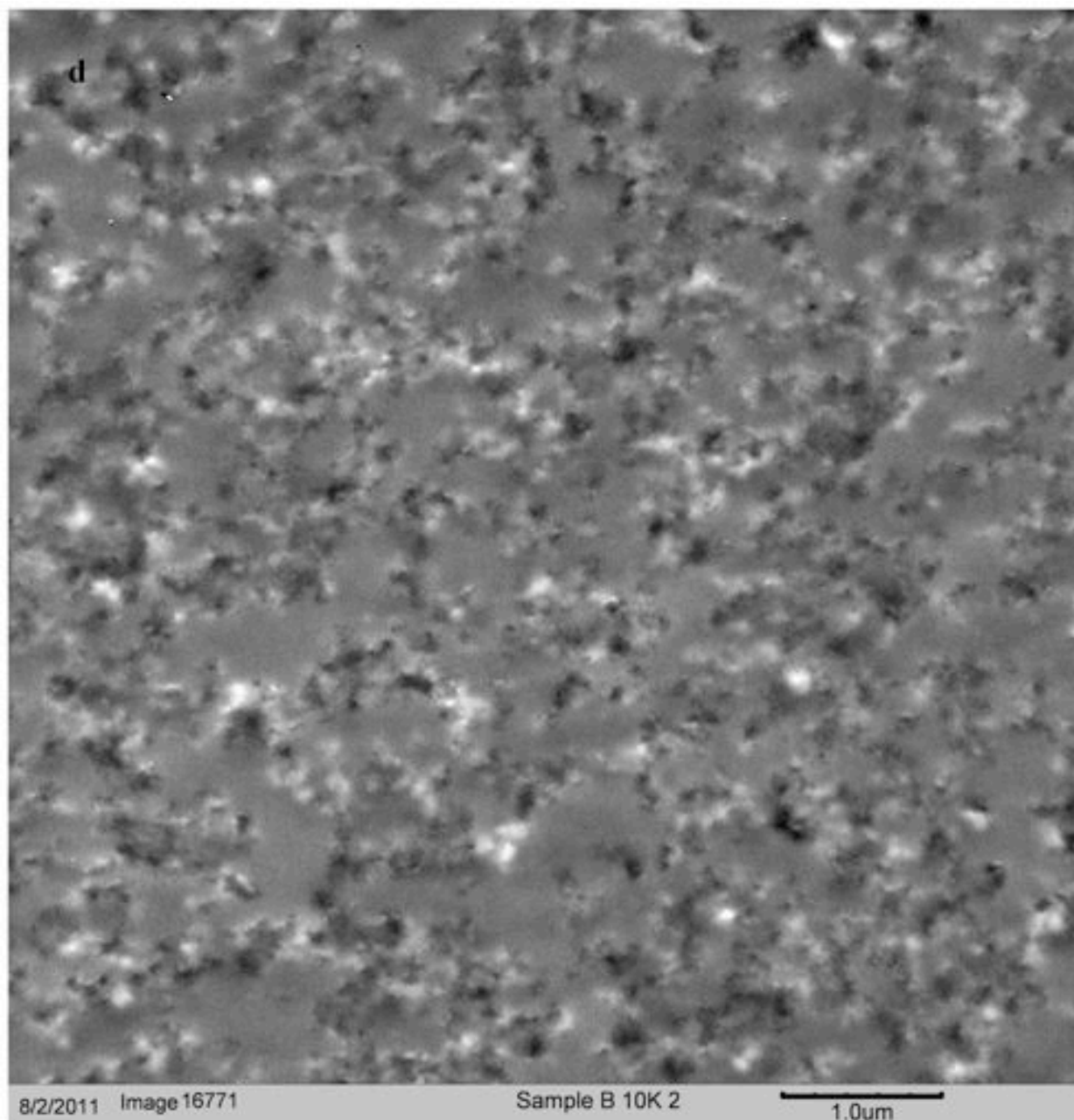
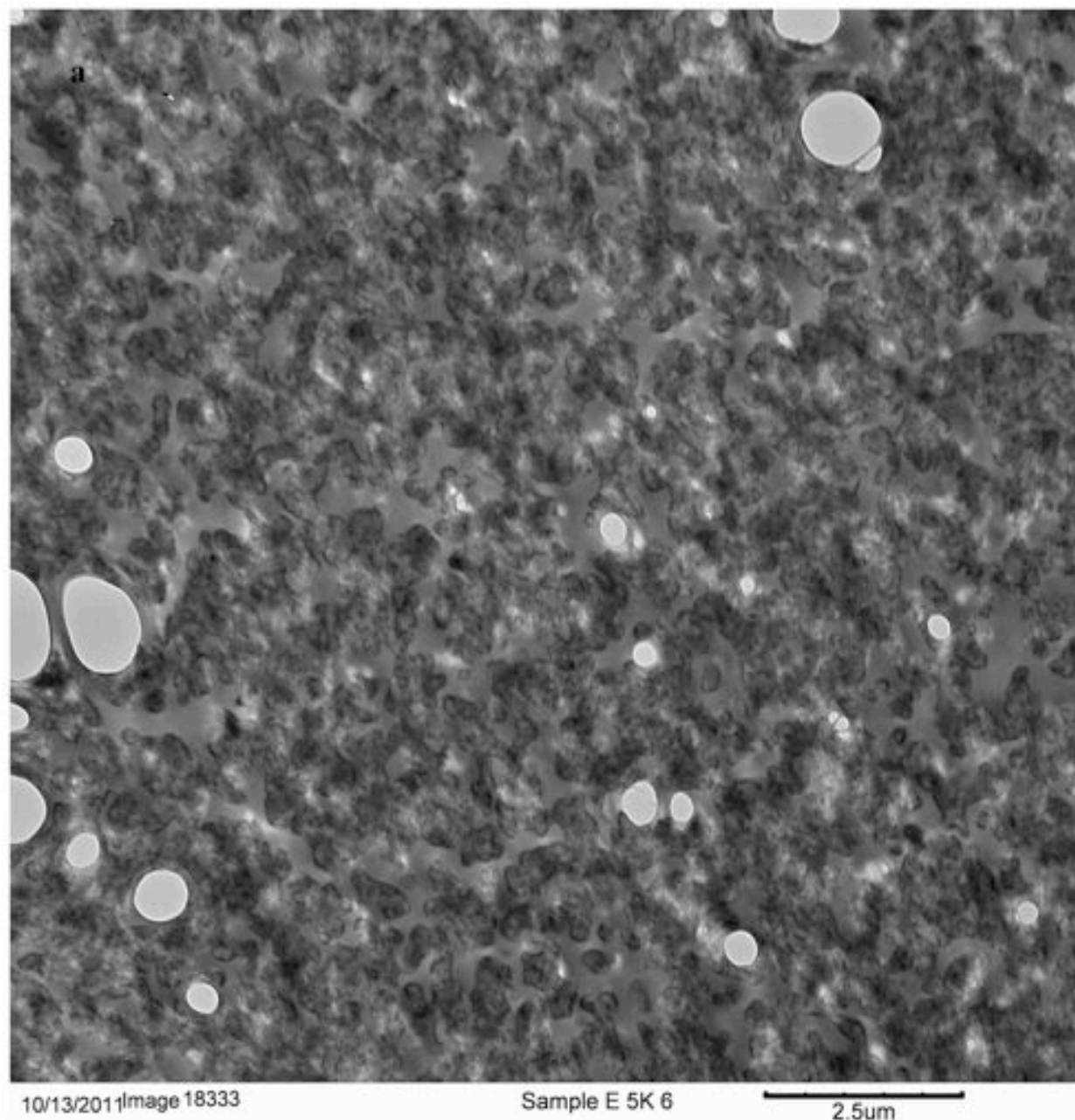


**Figure 4.5.d.**

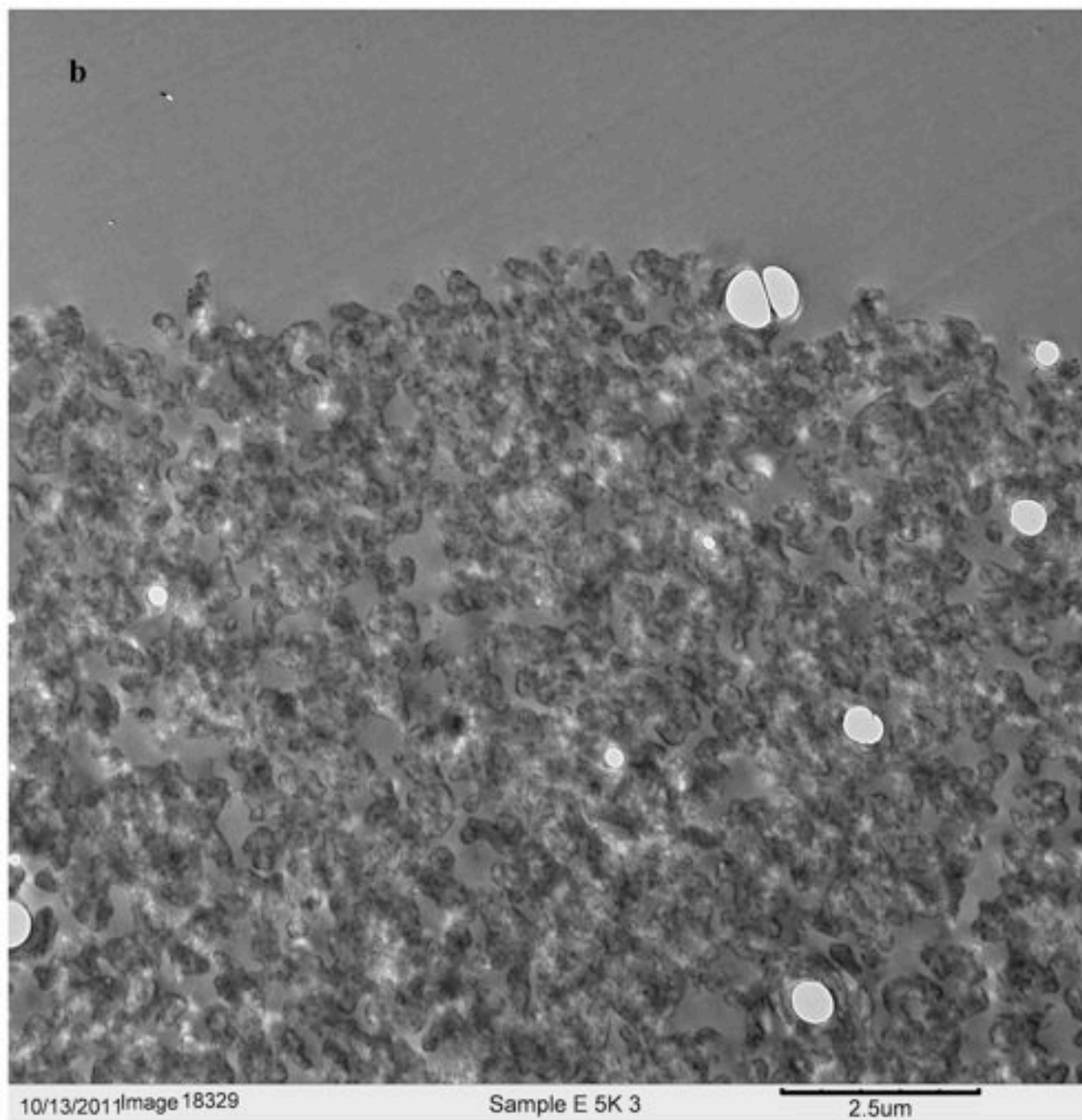
Figure 4.6 shows representative images of Sample B saturated with BSA. The effect of saturation can be seen through low magnification images (Fig. 4.6, a and b), where the matrix takes on a globular-like appearance. This suggests that BSA is not merely adsorbed on the pore wall. A closer look at the effect of BSA saturation can be seen through the higher magnification image (Fig. 4.6, c). A clear difference is seen when comparing this image to that obtained for the virgin resin (Fig. 4.5b and d). Most of what originally seemed like empty space now appears to be mostly filled with protein.

Figure 4.7 shows optical microscopy images of sections of the mini-column obtained as described in Section 3.2.2.1. The sections were 0.5  $\mu\text{m}$  in thickness and each of the sections shown was taken from the center of a mechanically compressed packed bed that had been embedded with LR White. The sections are representative of the packing of particles within a compressed column when looking in the direction of flow. The set of compression images show areas where many of the particles are in direct contact with one another. Although there is a large quantity of particles touching within the cross-sectional view of the column, there are also a significant amount of areas where resin beads are not touching, creating channels to allow flow through the column. Differences in the extraparticle void fraction are not readily apparent from the optical images, yet once quantified using Image J the effect of compression is clear as discussed below.

The extraparticle void fraction,  $\epsilon$ , was estimated from the optical microscopy images as follows. A section of known area was cropped within the image using Image J. Within this section, the individual particle area was determined by fitting a circle-drawing tool to the particle perimeter, and utilizing the measurement function built into the program. Non-circular particles were accounted for by using a lasso drawing tool, where the perimeter of the particle could be



**Figure 4.6.** Electron micrographs of Fractogel TMAE Sample B saturated with BSA. (a) 5k magnification image at the center of the particle, (b) 5k magnification image at the edge of the particle, and (c) 10k magnification image at the edge of the particle.



**Figure 4.6.b.**

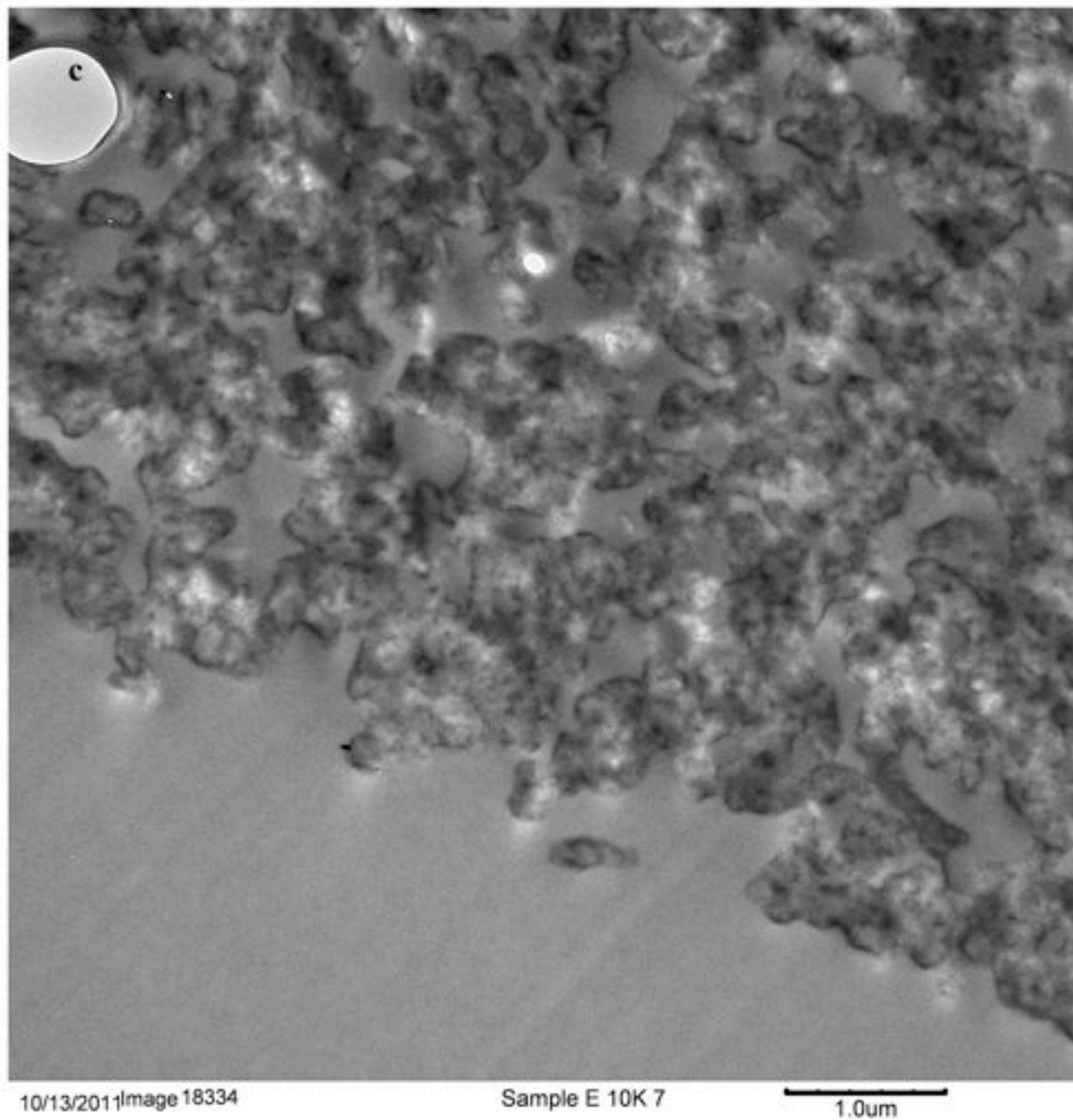
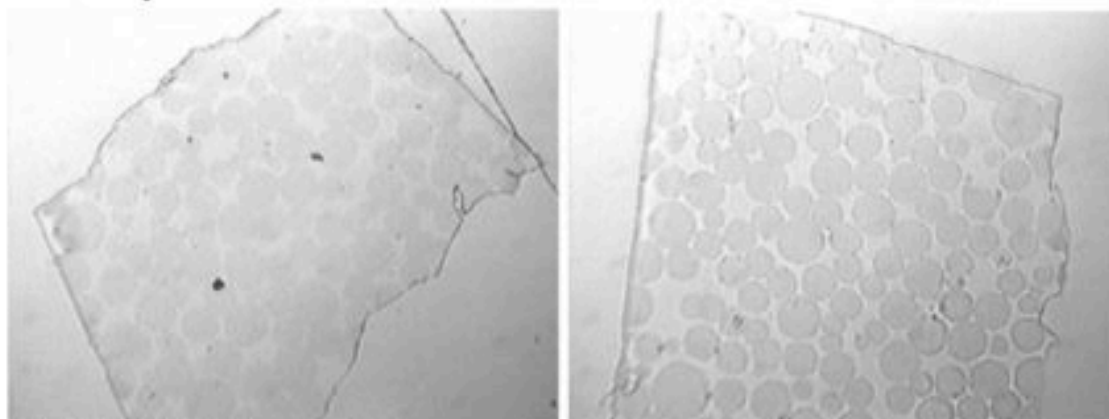
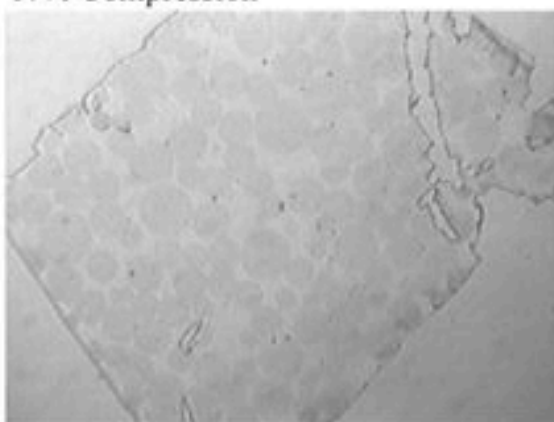


**Figure 4.6.c.**

10% Compression



17% Compression



30% Compression

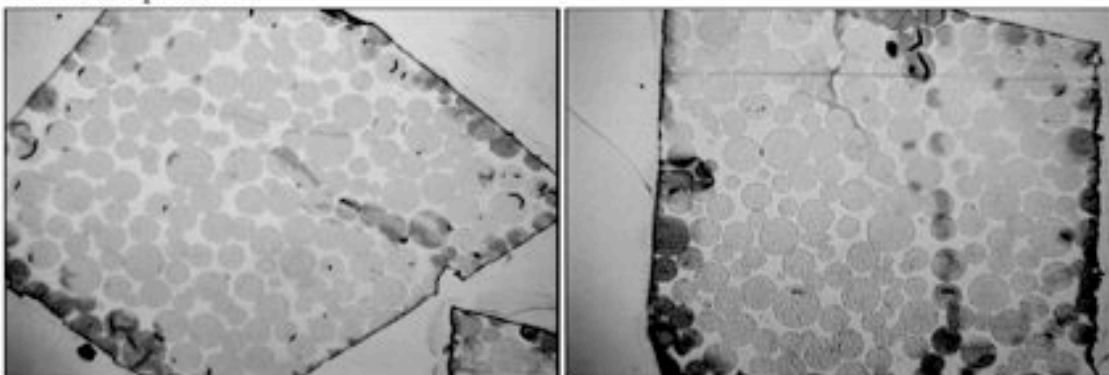


**Figure 4.7.** Optical images of mini-columns mechanically compressed to 10, 17 and 30% compression, embedded with LR White, dried onto microscope slides and stained using electric blue.

drawn and the area was calculated using the same measure function. The particle areas were then summed and divided by the total area of the cropped section to determine  $\varepsilon$ . The results are shown in Fig. 4.8. As seen from this figure,  $\varepsilon$  decreases as the bed compression increases.

Two different models were used in an attempt to describe these results. The first model assumes there is no change in the particle volume. In this case,  $\varepsilon$  can be written as follows (Stickel and Fotopoulos, 2001):

$$\varepsilon = \frac{\varepsilon_o - \lambda}{1 - \lambda} \quad (4.5)$$

where  $\varepsilon_o$  and  $\varepsilon$  are the initial and final extra particle porosities and  $\lambda$  is the average compression in the packed bed. As seen in Fig. 4.8, this model does not provide an adequate description of the data indicating that the particle volume may change when the bed is compressed. The second model is empirical and is given by the following relationship:

$$\varepsilon = \varepsilon_o - m\lambda \quad (4.6)$$

where  $m$  is related to the resin's elasticity. This equation accurately fits the data for the compression ratios under consideration. It should be noted, however, that the sections of the column analyzed were taken from the center of the column and compression may vary top to bottom and radially, thus,  $\lambda$  may vary throughout the column.

From the quantitative analysis of the optical images shown in Fig. 4.7, it is evident that under compression the resin particle's volume changes, and therefore the interaction between individual particles within the compressed bed was taken under consideration. Within the mechanically compressed packed bed, regions of particle contact are supplemented by open regions, which allow flow through the column. Fig. 4.9a and b show electron micrographs of the mini-column subjected to 30% mechanical compression, and are representative of areas seen in the optical images where particles are and are not touching within the packed bed. A closer look

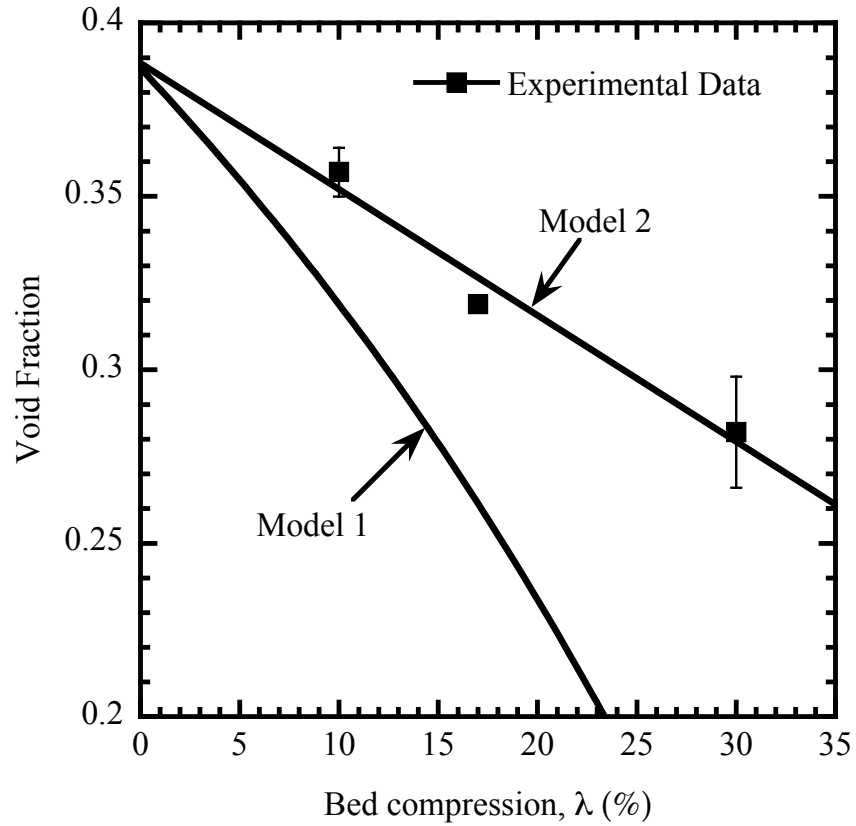


**Figure 4.8.** Comparison of experimental and theoretical  $\varepsilon$ -values based on two compressibility models as described in eqs. 4.5 and 4.6.

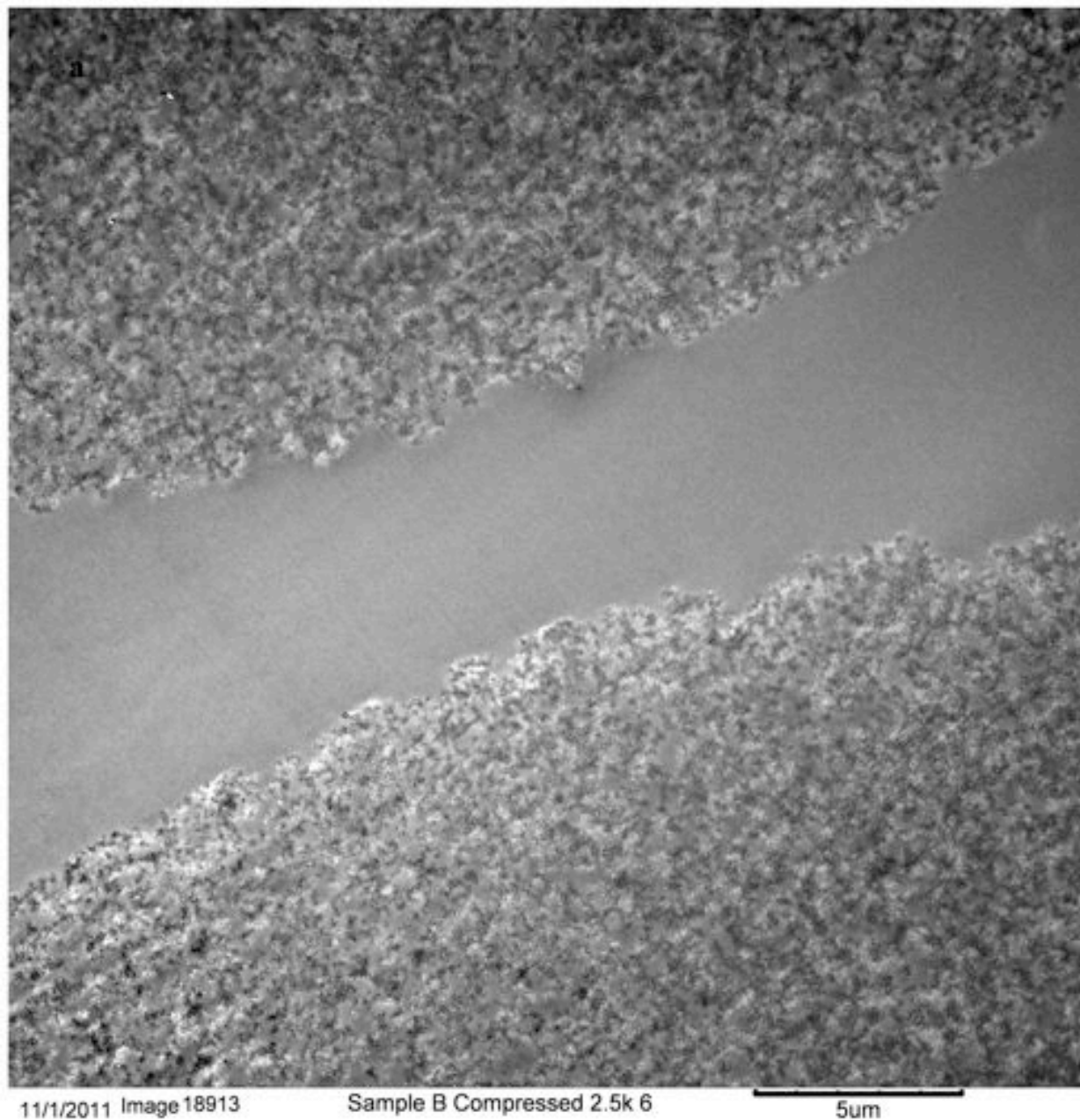


**Figure 4.9.** Representative electron micrographs of Fractogel TMAE HiCap (m) within a 30% mechanically compressed column. Low magnification images of two particles in (a) close contact and (b) touching. Higher magnification images of two particles touching are shown at (c) 5k with (d) a 10k close up of the area of contact.

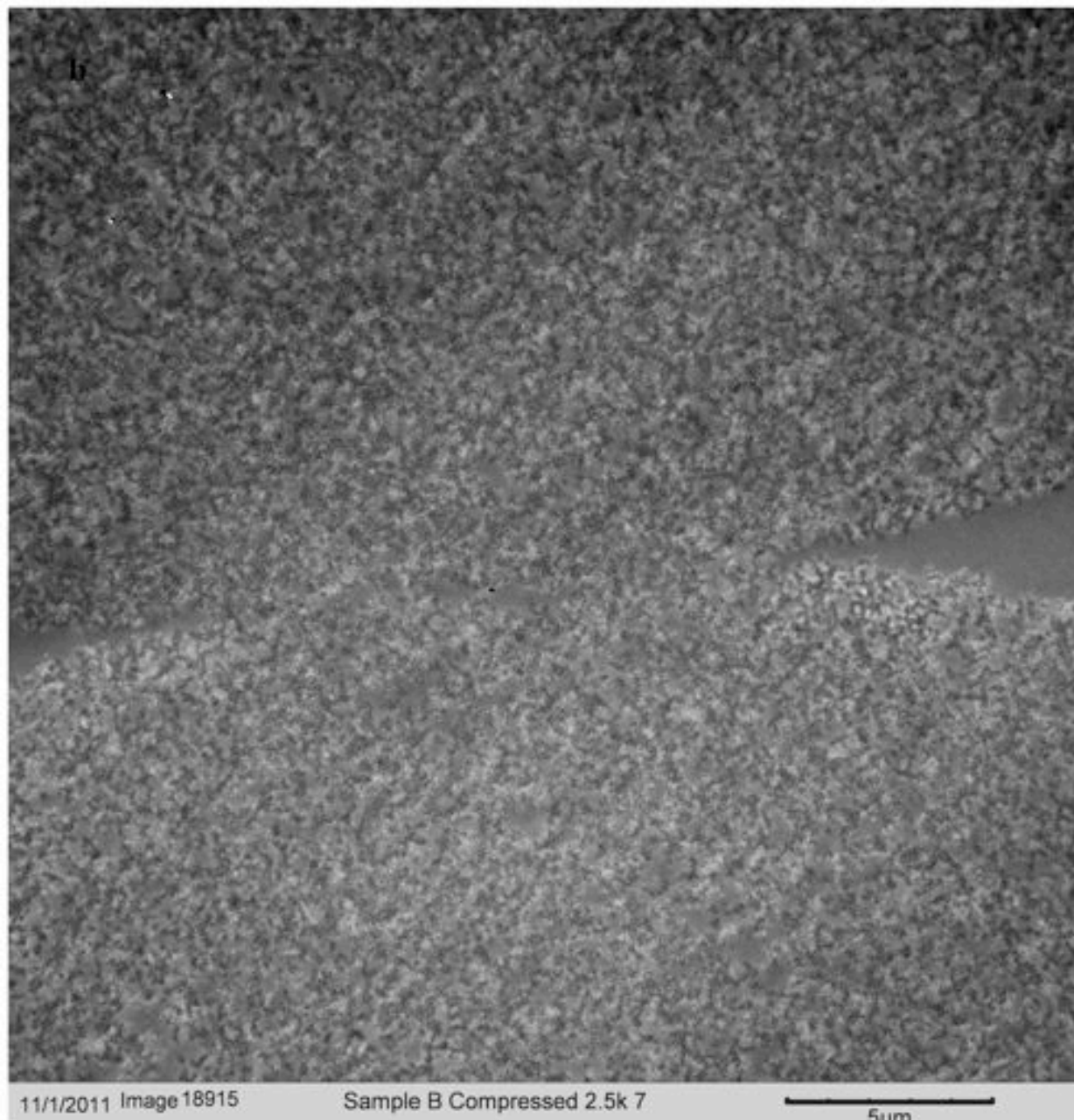


**Figure 4.9.b.**

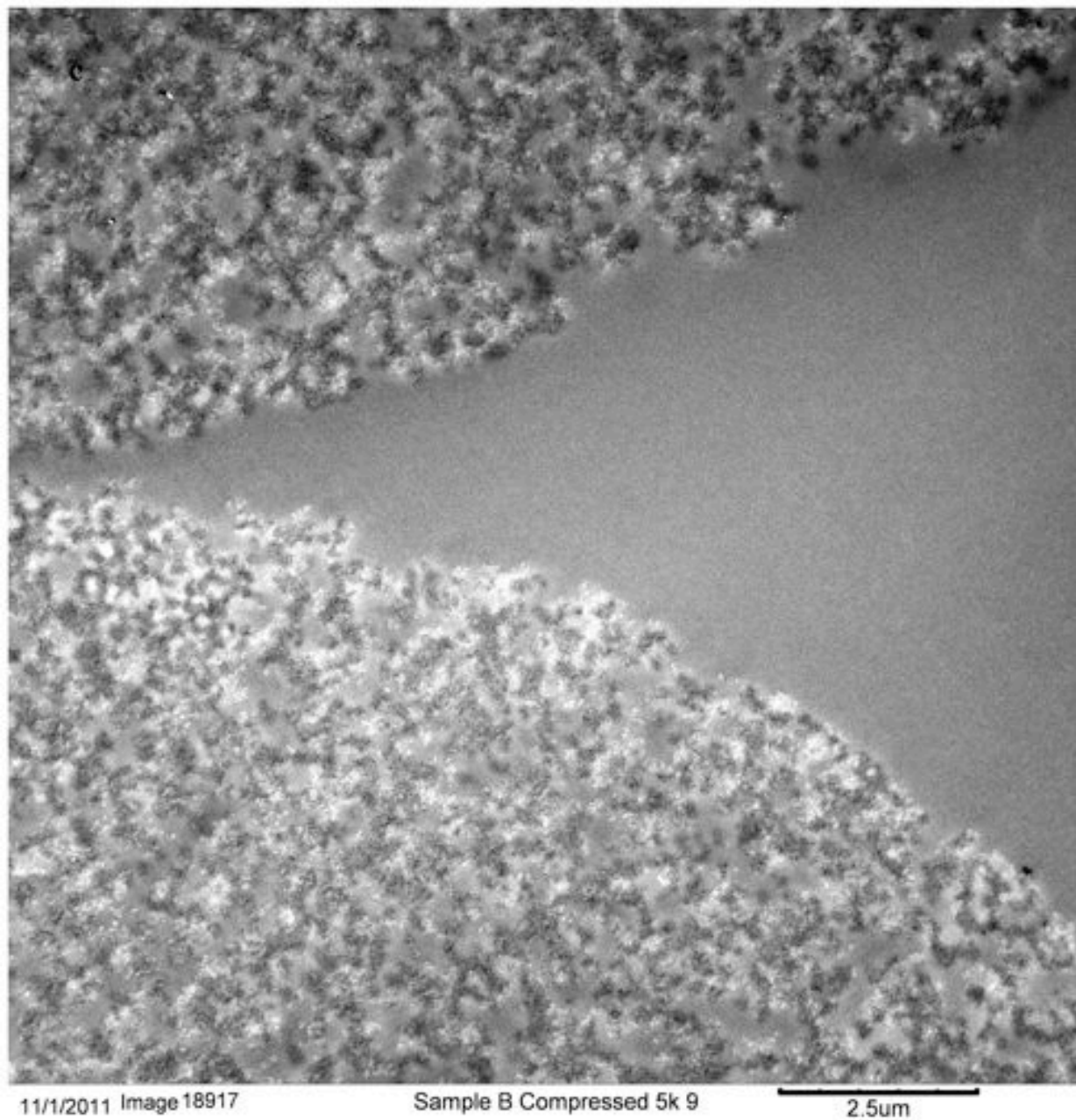


**Figure 4.9.c.**

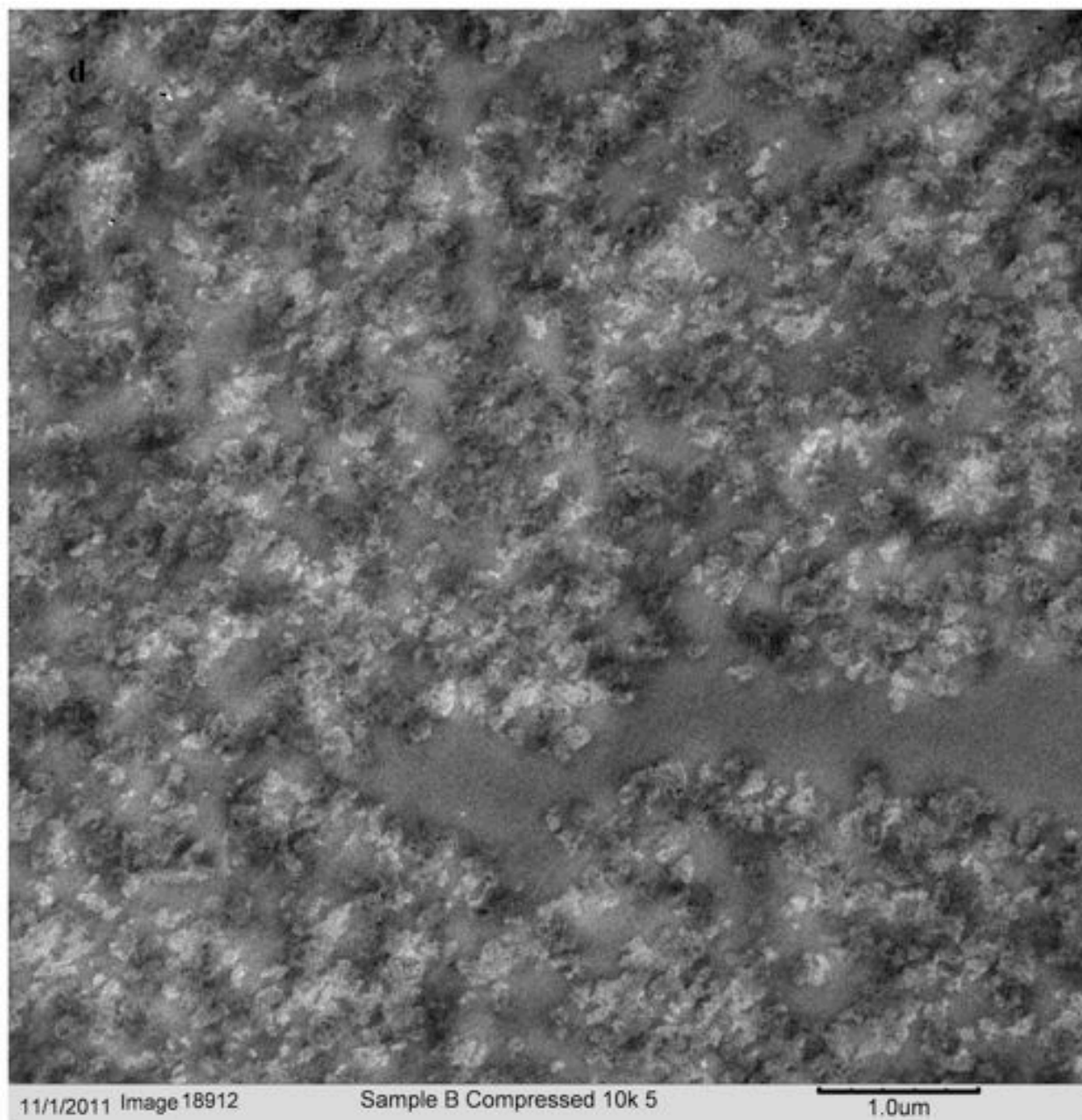


**Figure 4.9.d.**

at an area in the column where two resin particles come into contact can be seen in the electron micrographs shown in Fig. 4.9c and d. From these images, it is evident that under compression, individual particle edges are virtually indistinguishable when in direct contact. This suggests minimal flow in regions where particles are touching.

### 4.3 Protein binding capacity studies

Adsorption studies were conducted for 1.5 and 24 hours to determine the resin's binding capacity for BSA and Thyroglobulin. These proteins were chosen as models for small (BSA) and large (Tg) proteins encountered in actual applications. Figure 4.10 shows the amount of each protein bound as a function of protein concentration. For BSA (Fig. 4.6a) similar capacities and nearly rectangular isotherms are obtained at both time scales. A fit of the 24-hour data according to Langmuir's isotherm equation is also shown in Fig. 4.10. This equation is as follows:

$$q = \frac{q_m KC}{1 + KC} \quad (4.7)$$

where  $q$  is the concentration of bound protein,  $q_m$  is the maximum binding capacity,  $K$  is an equilibrium constant, and  $C$  is the protein concentration in solution. For BSA, the fitted parameter values are  $q_m=178\pm 1$  mg/mL of particle and  $K=95\pm 11$  mL/mg.

The results for Thyroglobulin are quite different. The amount of protein adsorbed varies with protein concentration even at 24 hours, and substantial differences exist between 1.5 and 24 hour measurements. These differences are likely caused by strong diffusional limitations caused by the large size of Thyroglobulin compared to BSA. As shown by Yang et al. (2002) for other anion exchangers, the equilibrium binding capacity achieved using Thyroglobulin can be comparable to that for smaller proteins for very long time scales. Significant differences are seen in the protein adsorption rate, however, with the equilibrium binding capacity of a small protein

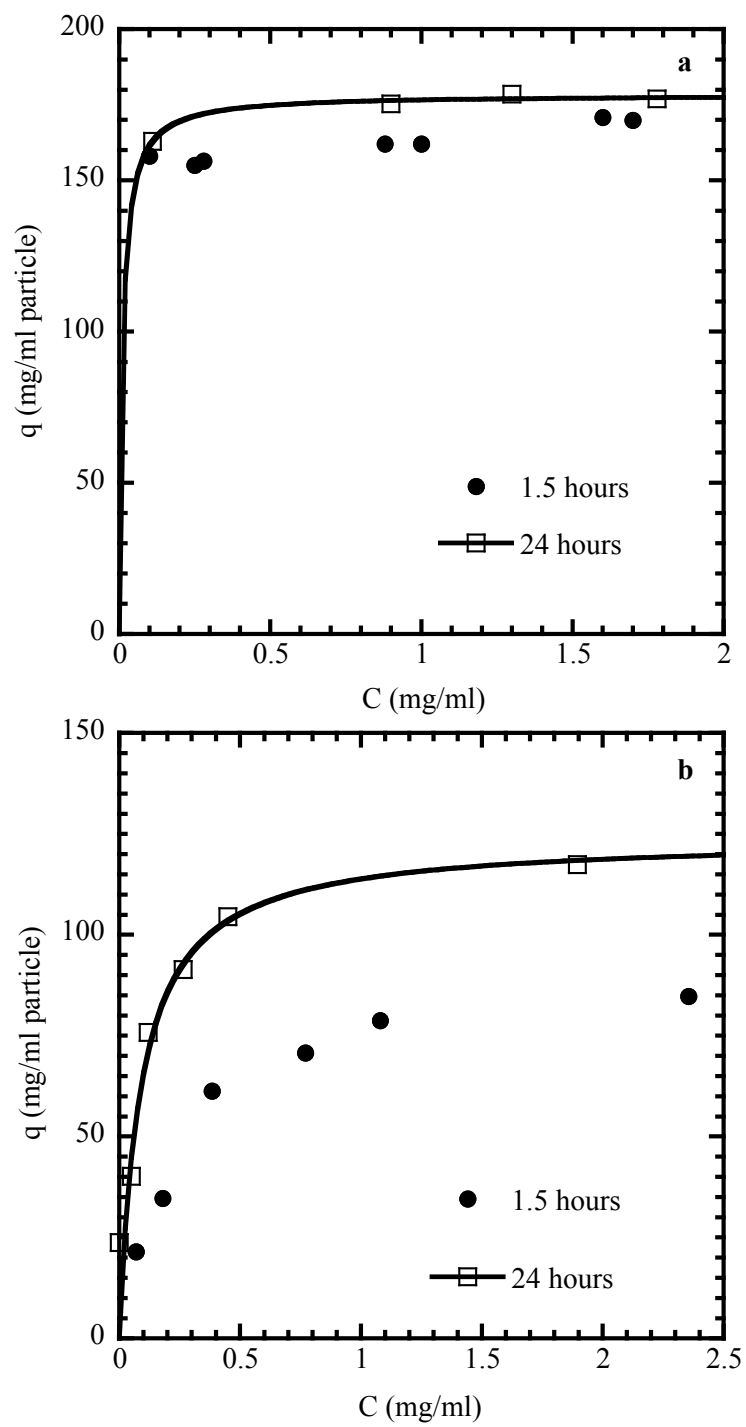


**Figure 4.10.** Single component adsorption isotherms for Sample B for (a) BSA and (b) Thyroglobulin.

occurring within 1 hour in comparison to approximately 120 hours for Thyroglobulin. For our data, the fitted parameters of the Langmuir isotherm obtained for the 24 hour Thyroglobulin data are  $q_m=124\pm 12$  mg/mL of particle and  $K=11\pm 4.3$  mL/mg. The smaller  $K$  value is likely a result of the fact that the experiment may not have reached equilibrium.

#### 4.3.1 Batch adsorption kinetics

Batch adsorption studies were conducted to determine the protein adsorption kinetics for both BSA and Thyroglobulin. Figure 4.11 shows the batch uptake curves for BSA and Thyroglobulin at different initial protein concentrations. In the case of BSA, the rate of adsorption increases significantly as the protein concentration in solution increases. However, nearly the same ultimate binding capacity is attained for long times at both 0.2 and 0.5 mg/mL initial concentration. This ultimate capacity is very comparable to the value obtained after 1.5 h of contact with the resin, but about 10% lower than the 24 h values given in Section 4.3. These results show that most of the binding capacity, up to about 160 mg/mL, is attained quickly while the remaining capacity, up to 178 mg/mL, is attained only very slowly. The difference of about 18 mg/mL could be due to protein binding in very small pores, where BSA diffusion is very highly hindered. As discussed in Section 2.1.2, the pore diffusion model, assuming that the real isotherm is rectangular, was fitted to these experimental data. Both the binding capacity,  $q_m$ , and the effective pore diffusivity,  $D_{e,app}$ , were fitted. These values are summarized in Table 4.2. The external mass transfer coefficient,  $k_f$ , was estimated based on a Sherwood number  $Sh=30$ , as discussed in Section 2.1.3. Figure 4.12 shows a comparison of experimental and calculated curves.

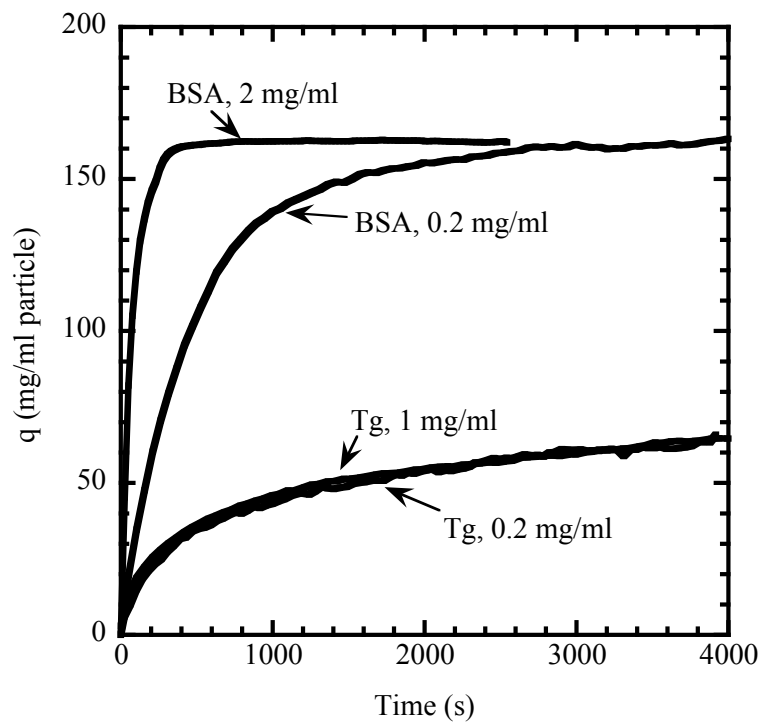


**Figure 4.11.** Batch uptake curves for purified BSA and Thyroglobulin at different initial protein concentrations.

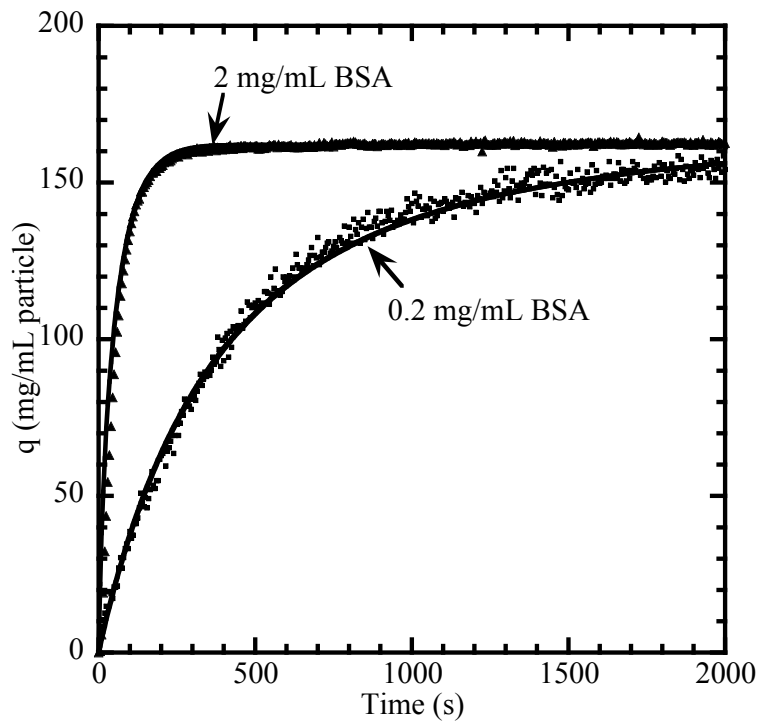


**Figure 4.12.** Batch uptake curves for BSA at different initial protein concentrations. The line shows the fitted curves obtained using the pore diffusion model.

**Table 4.2.** Parameters obtained by fitting the BSA uptake data with the pore diffusion model.

Initial Protein Concentration	Final Protein Concentration	$q_m$ (mg/mL particle)	$D_{e,app}$ ( $10^{-7}$ cm <sup>2</sup> /sec)	$D_{e,app}/D_o$	$k_f$ ( $10^{-3}$ cm/s)	$Bi$
2.0	1.02	160	15	2.5	2.5	5.9
0.2	0.04	155	40	6.8	2.5	2.1

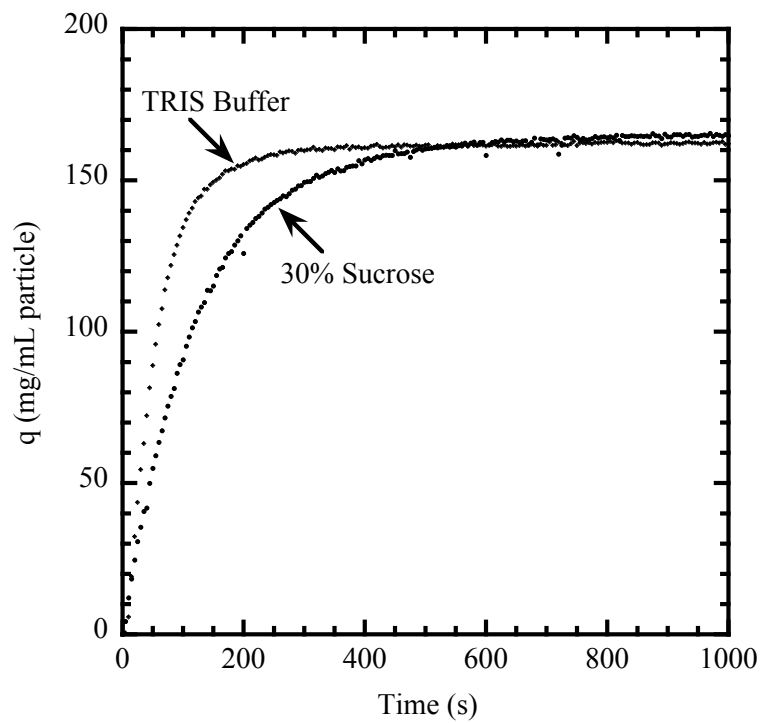
The parameters obtained from this fitting exercise reveal some interesting trends. Firstly, only small differences are seen for the binding capacities at different initial protein concentrations, which is consistent with very favorable binding and a rectangular isotherm behavior. Secondly, the effective pore diffusivity at 0.2 mg/mL is substantially higher than the value at 2 mg/mL, which is not consistent with ordinary pore diffusion. Thirdly, the ratio of effective pore diffusivity to free solution diffusivity is much higher than one, indicating that adsorption of BSA is much faster than could be predicted for ordinary diffusion in liquid-filled pores. Table 4.2 also gives the Biot number,  $Bi$ , calculated from the  $D_{e,app}$  and  $k_f$  values as noted in Section 2.1.3.  $Bi$  represents the ratio of intraparticle and extraparticle mass transfer resistances. In general, when  $Bi > 10$ , the external resistance is negligible (LeVan and Carta, 2007). However, in our case, the  $Bi$ -values are much less than 10, and close to one at low protein concentrations, indicating that BSA adsorption is actually largely controlled by the external resistance. This result suggests that a solid diffusion mechanism, driven by the total adsorbed concentration gradient in the particle is responsible for the rapid protein adsorption kinetics observed experimentally (Chen et al., 2002; Carta et al., 2005; Stone and Carta, 2007; Lenhoff, 2008). This trend has been seen for other polymer-grafted materials, where the small accessible pore size would generally suggest a diffusional hindrance, yet high protein adsorption is observed indicating the importance of transport in the functionalized tentacles (Stone and Carta, 2007; Perez et al., 2011; Lenhoff, 2011).

Figure 4.11 shows the batch uptake curves for two initial Thyroglobulin concentrations. As previously discussed, the diffusional hindrance due to the molecular size of the protein extends the time to achieve the equilibrium binding capacity. For the concentrations under consideration, the batch uptake curves are nearly identical, indicating that the external mass transfer resistance does not affect the overall process of Thyroglobulin adsorption. The binding capacity achieved during the experimental time frame was 65 mg/mL of particle. This value is comparable to that obtained for the 1.5-hour adsorption isotherms, but is only 47% of the binding capacity observed at 24-hours.

The effect of sucrose on protein adsorption was investigated to validate the CLSM set up. Figure 4.13 shows the adsorption of 2 mg/mL BSA in Fractogel TMAE using a standard buffer solution and one made up of 30% sucrose. The difference in the adsorption of BSA is found to be proportional to the viscosity of the solution, with the relative viscosity of a 30% sucrose solution being 3.181 (Swindells et al., 1958). However, essentially the same capacity is attained.

#### **4.4 Confocal laser scanning microscopy**

Figure 4.14 shows representative CLSM images for the adsorption of 0.2 mg/ml BSA. BSA appears to diffuse rapidly to the particle center during the first few minutes after which the distribution of protein appears to be uniform within the particle. As shown by the batch adsorption data in Section 4.3.1, saturation requires over 30 min. The diffuse adsorption profile during the first few minutes suggests that protein migration within the individual resin beads is controlled by “solid diffusion”. The transport mechanism is further validated by the presence of flat protein concentration profiles after a few minutes of exposure to the protein solution indicating that the saturation of the particle surface occurs at a uniform rate thereafter. This result is congruent with the batch uptake data obtained for BSA monomer, where the dependence



**Figure 4.13.** Comparison of batch uptake curves for 2 mg/mL purified BSA using TRIS buffer and 30% sucrose solution.

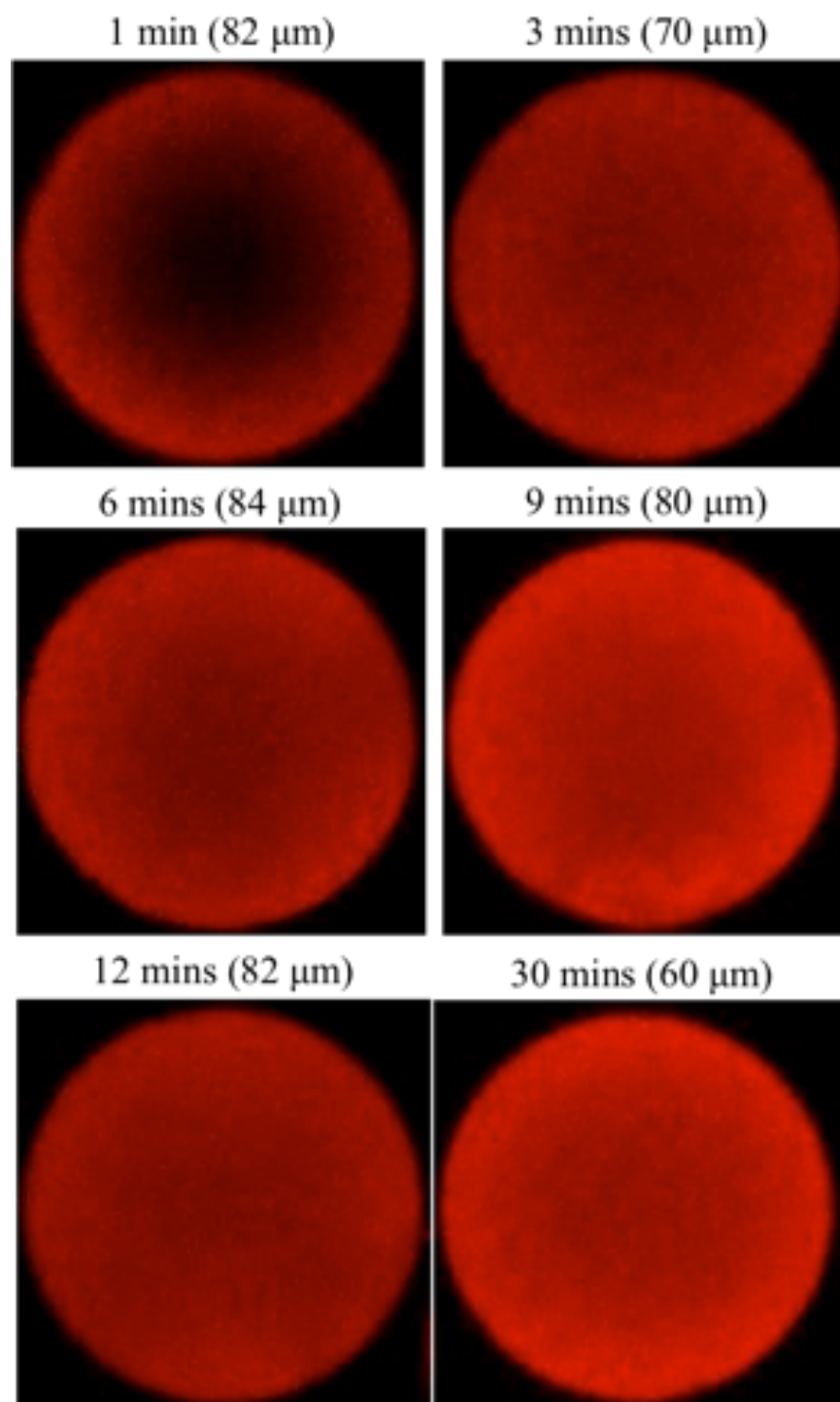


**Figure 4.14.** CLSM images of batch adsorption of 0.2 mg/mL BSA in Fractogel TMAE Sample B. The laser intensity was varied in order to avoid saturation of the CCD detector; up to 9 minutes an intensity of 2% was used, with an intensity of 0.8% thereafter.

of the diffusivity ratio and small  $Bi$  suggests solid diffusion with a large mass transfer resistance. Results for adsorption of 0.5 mg/mL BSA are given in Fig. 4.15. Since the images were taken at different time scales for the concentrations under consideration, a comparison of the adsorption rate cannot be made. It is evident, however, that in both cases BSA is rapidly adsorbed yielding flat concentration profiles within a few minutes of exposure to the protein solution.

The effect of viscosity on protein adsorption was investigated through the use of a 0.2 mg/mL BSA containing 30% sucrose. Figure 4.16 shows representative CLSM images for the adsorption of BSA from this solution. As seen from the batch uptake curves (Fig. 4.14), the adsorption from a viscous solution yields a slower adsorption rate, but the rate is still quite fast. This is also seen in the CLSM images, where flat concentration profiles are achieved in less than 6 minutes of exposure to the protein solution.

Representative CLSM images for batch mode transient adsorption using 0.2 mg/mL Thyroglobulin solution are shown in Figure 4.17. The protein concentration profiles are also smooth for these conditions. The rate of adsorption is much slower, however, when using this larger molecule; this is in agreement with the previous batch uptake results showing a much slower adsorption rate when compared to BSA. It is evident from observing the adsorption of Thyroglobulin over time that the large molecules create a band around the exterior of the particle, and then slowly make their way to the center. Complete saturation of the resin was unattainable within the 1.5-hour time frame of the experiment.

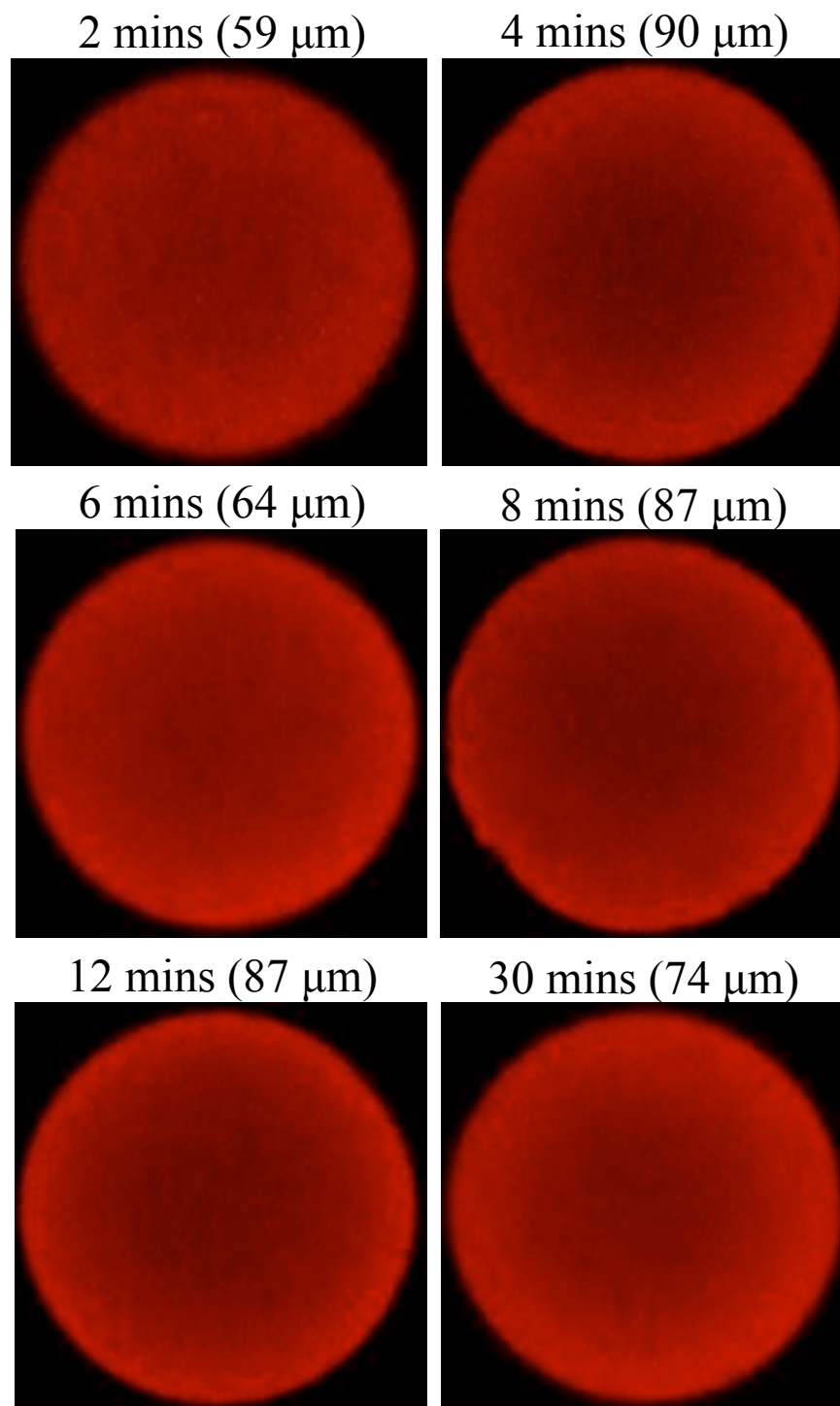


**Figure 4.15.** CLSM images of batch adsorption of 0.5 mg/ml BSA in Fractogel TMAE Sample B. The laser intensity was varied in order to avoid saturation of the CCD detector; up to 9 minutes an intensity of 2% was used, with an intensity of 0.8% thereafter. The individual resin bead diameter is shown in parentheses above each image.

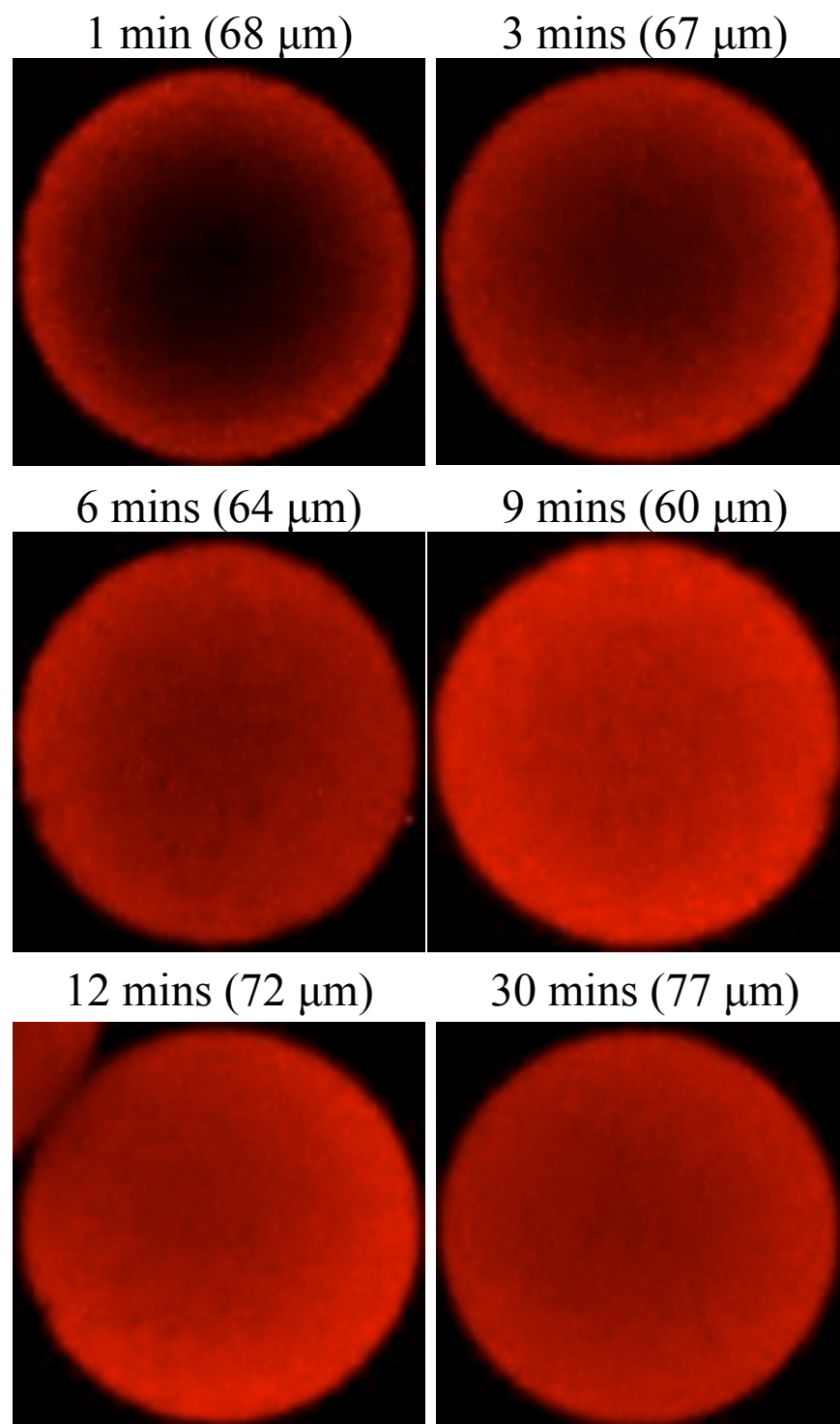


**Figure 4.16.** Batch adsorption CLSM images of 0.2 mg/mL BSA 30% sucrose solution using Fraactogel TMAE Sample B. The laser intensity was varied in order to avoid saturation of the CCD detector; up to 12 minutes an intensity of 4% was used, with an intensity of 2% thereafter. The individual resin bead diameter is shown in parentheses above each image.

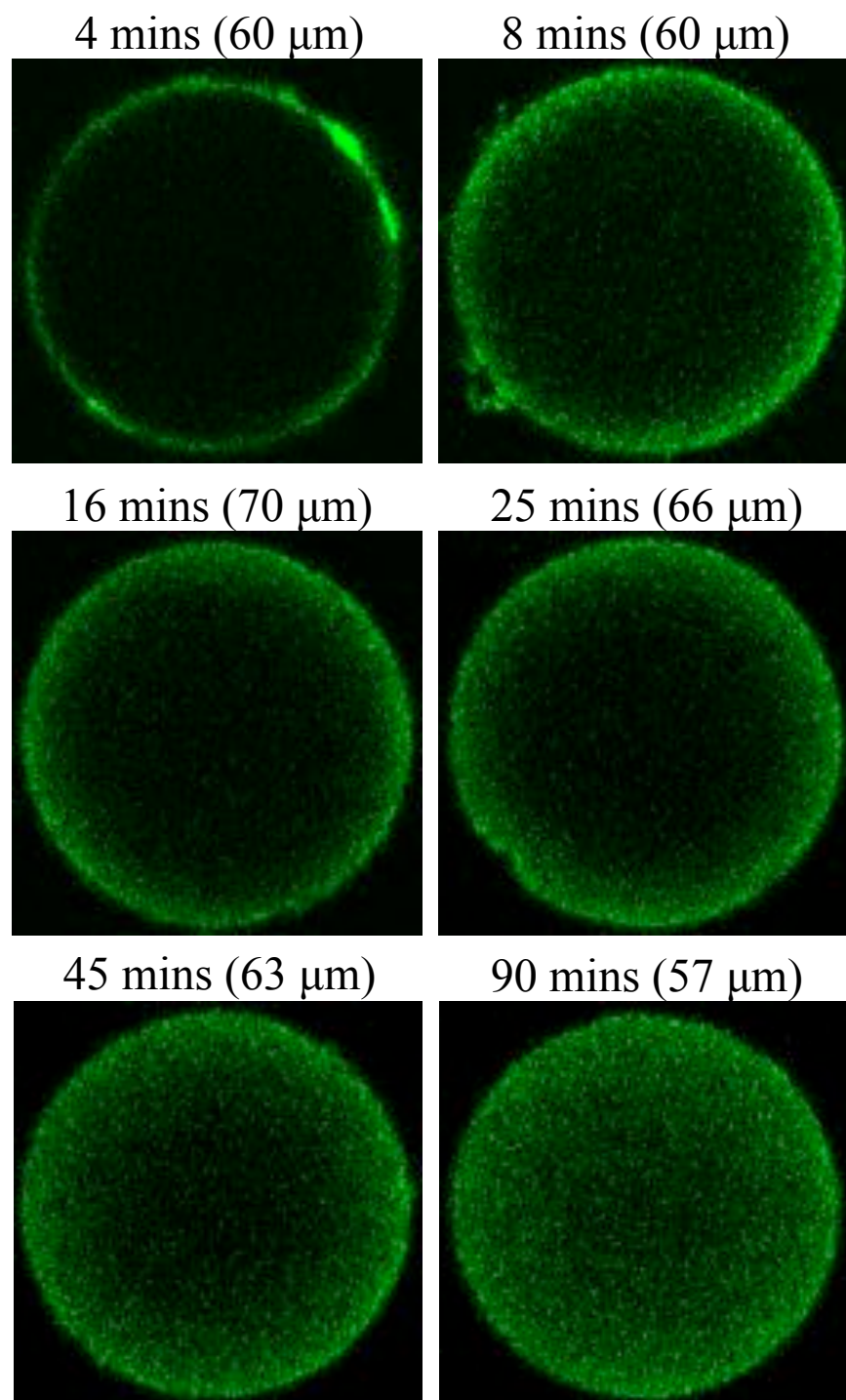


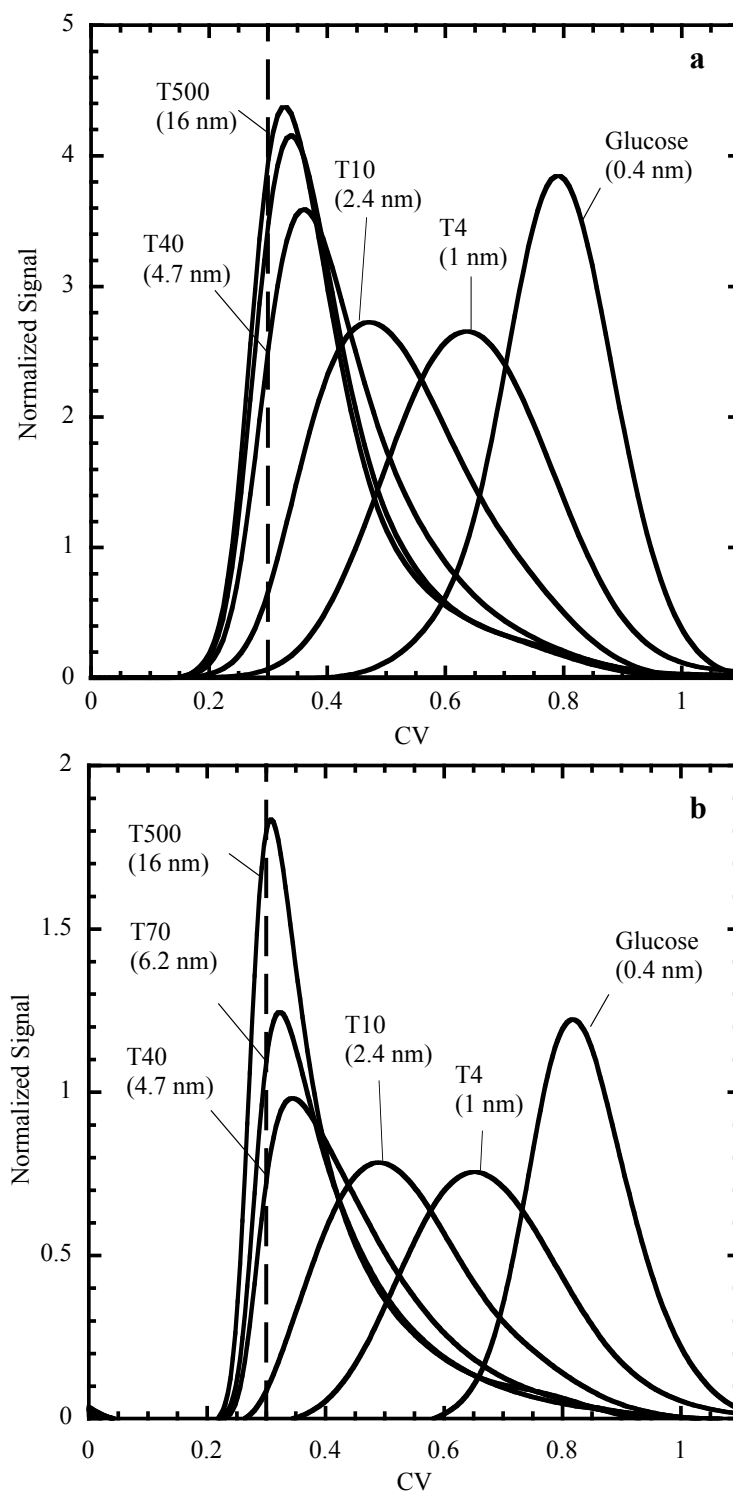
**Figure 4.17.** CLSM images of batch adsorption of 0.2 mg/mL Thyroglobulin in Fractogel TMAE Sample B. Each of the images shown was taken at an intensity of 19%. The individual resin bead diameter is shown in parentheses above each image.

## Chapter 5. Results for Fouled Resin Samples

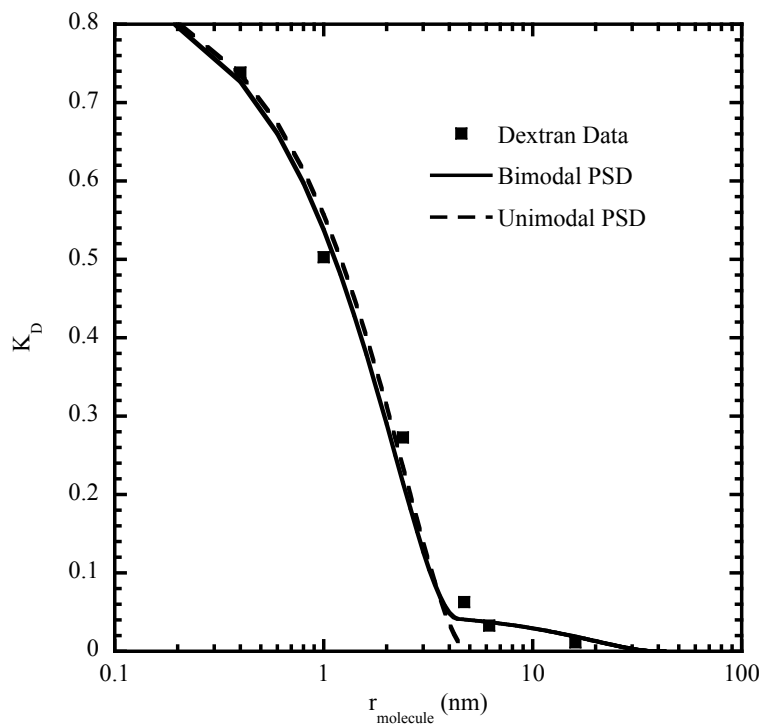
### 5.1 Inverse size exclusion chromatography

Figure 5.1 shows the iSEC chromatograms for glucose and dextran probes up to 500 kDa for both virgin and fouled resin samples. In comparing the two results, it is evident that there are only slight differences in the retention volume of the probes. A variance is seen in the breadth and height of the peaks. However, this is due to the difference in column volume and flow rate for the different samples. The residence time of the mobile phase was kept constant in both experiments. The results show that for both samples, glucose has access to a large fraction of the particle volume, with peak maximums at 0.80 and 0.82 column volumes for samples B and D, respectively. The higher molecular mass dextrans (40 kDa and higher), however, are substantially excluded. This result suggests that the foulant does not change the accessibility of the particle interior by these neutral molecules. In fact, there is almost no change in the retention volume of T4 and T10 dextrans.

Unimodal and bimodal models were used to determine the average pore radius for both resin samples as previously discussed in Section 4.1. Figure 5.2 shows a comparison of eqs. 4.2 and 4.3 with the experimental  $K_D$ -values for Sample D. The single pore size model was only able to accurately fit the low molecular weight probes, as previously seen when applied to experimental  $K_D$ -values for Sample B (Fig. 4.4). The bimodal pore distribution model accurately fit the whole set of data for both samples, indicating the presence of large and small pores throughout the resin matrices. Table 5.1 summarizes the model parameters determined by data fitting for both cases. The pore radii determined through the use of the bimodal model show insignificant differences between the two samples, with the majority of the porosity associated with small pores of approximately  $4.3 \pm 0.1$  nm in radius.



**Figure 5.1.** Inverse size exclusion results for Fractogel TMAE (a) Sample B – virgin and (b) Sample D – fouled. The dashed line represents the retention volume of dextran T2000. Both columns had an internal diameter of 0.5 cm and were ran at a flow rate of 0.5 mL/min. The lengths of the packed bed were 5.6 and 5.5 cm for Samples A and B, respectively.



**Figure 5.2.** Comparison of experimental and theoretical  $K_D$ -values for Sample D based on unimodal and bimodal pore distribution models.

**Table 5.1.** Parameters obtained for virgin (B) and fouled (D) samples using unimodal and bimodal models for inverse size exclusion data. Index (a) indicates the average pore radius reported by EMD Chemical for Fractogel TMAE.

<b>Unimodal</b>					
Sample	$\varepsilon_p$	$r_{pore}$ (nm)			
B	0.82	5			
D	0.87	4.4			

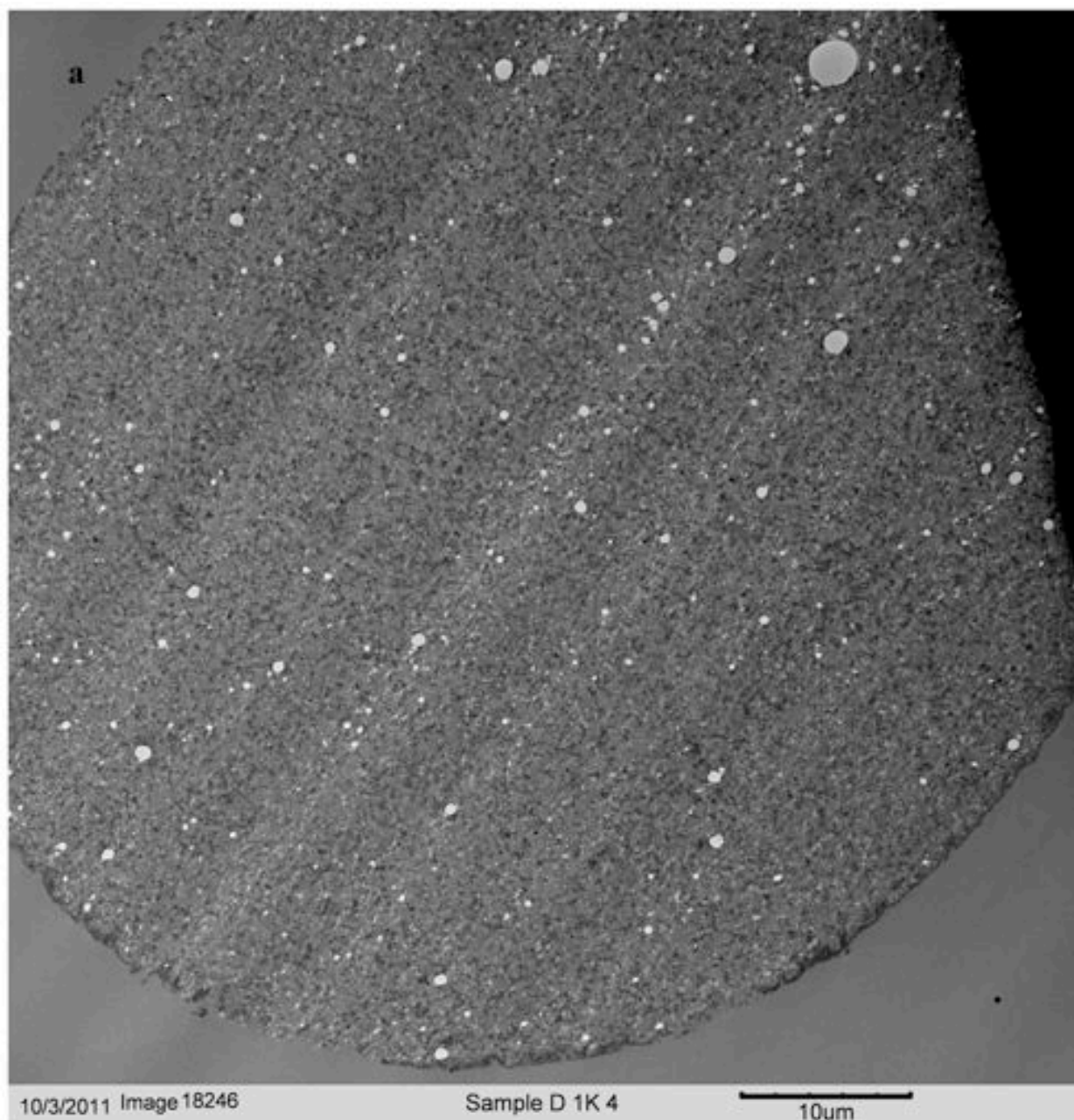
  

<b>Bimodal</b>					
Sample	$\varepsilon_{p,total}$	$\varepsilon_M$	$r_{pore,M}$ (nm)	$\varepsilon_m$	$r_{pore,m}$ (nm)
B	0.82	0.09	40 <sup>(a)</sup>	0.81	4.3
D	0.87	0.05	40 <sup>(a)</sup>	0.86	4.4

## 5.2 Transmission electron microscopy

Transmission electron microscopy was used to determine the location of foulant on Fractogel TMAE Sample D. Figure 5.3 shows electron micrographs at different magnifications for this sample. At low magnification (Fig. 5.3a), the presence of a denser skin layer covering a large percentage of the particle exterior surface can be seen. The high magnification image (Fig. 5.3b) of a fouled area at the edge of the particle shows that the dense layer is about 0.5  $\mu\text{m}$  in thickness. However, the images at the center of the particle (Fig. 5.3c) looks almost identical to that of the virgin resin (Fig. 4.5) indicating that no fouling occurs within the particle itself.

The previous TEM images of Sample D were for particles that were initially packed in a column, subjected to multiple operating cycles, unpacked, and then embedded. The discontinuous nature of the skin layer was thus investigated by imaging a mechanically compressed, fouled mini-column embedded (without unpacking) as discussed in Section 3.2.2.2. It is hypothesized that the regions apparently devoid of foulant are where particles were originally in contact with each other in the packed bed. Figure 5.4 shows representative TEM images of the fouled mini-column. Black and white arrows emphasize areas where the foulant is and is not present on the particle surface. Not only is the skin layer absent where the particles



**Figure 5.3.** Transmission electron micrographs of Fractogel TMAE HiCap (m) Sample D. (a) Image of particle at 1k magnification showing a denser skin layer over a substantial portion of the particle exterior; (b) 10k image showing structure of dense skin layer, about 0.5  $\mu\text{m}$  thick, at particle exterior surface; (c) 10k image of particle interior showing no evidence of foulant.

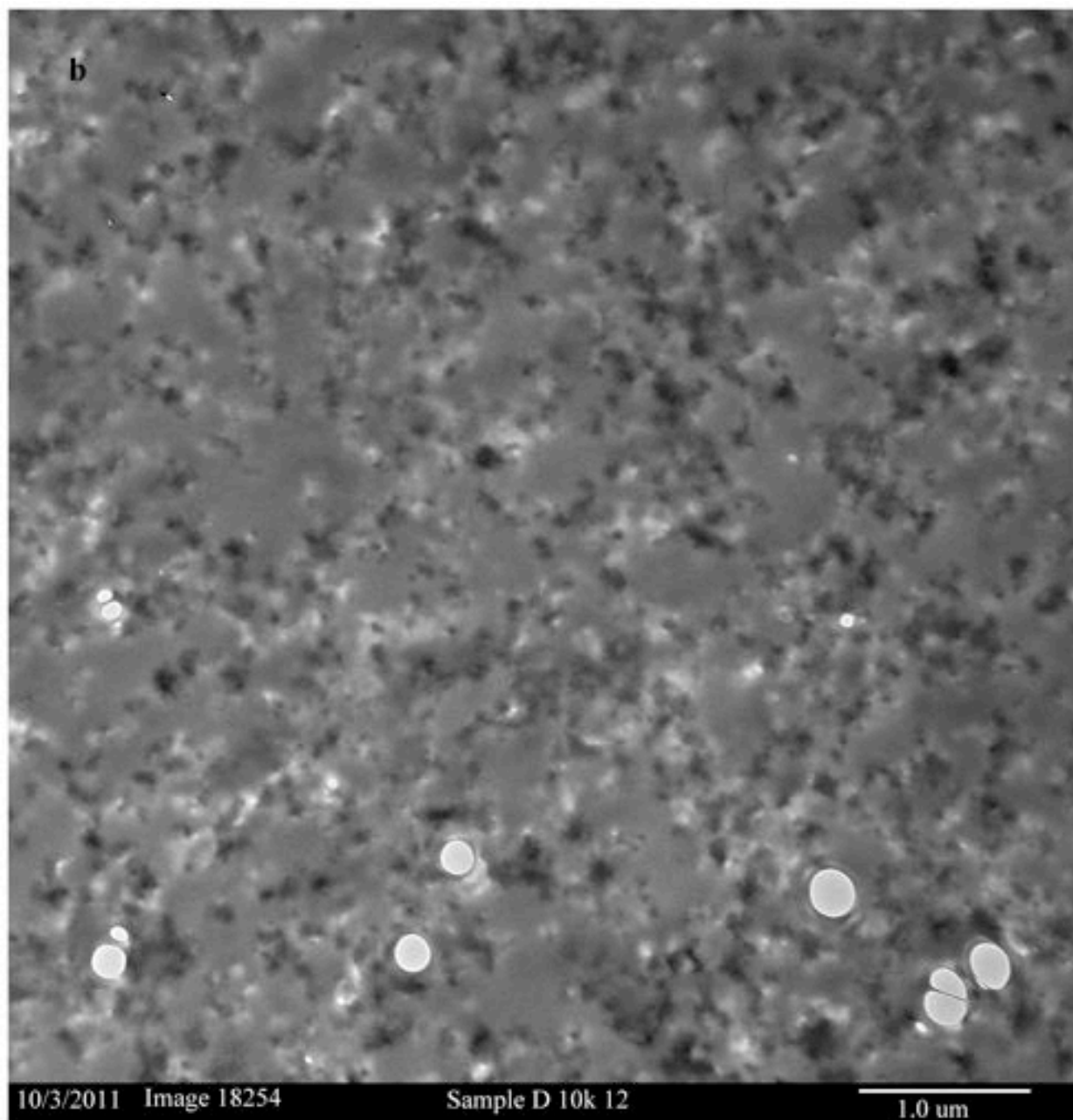
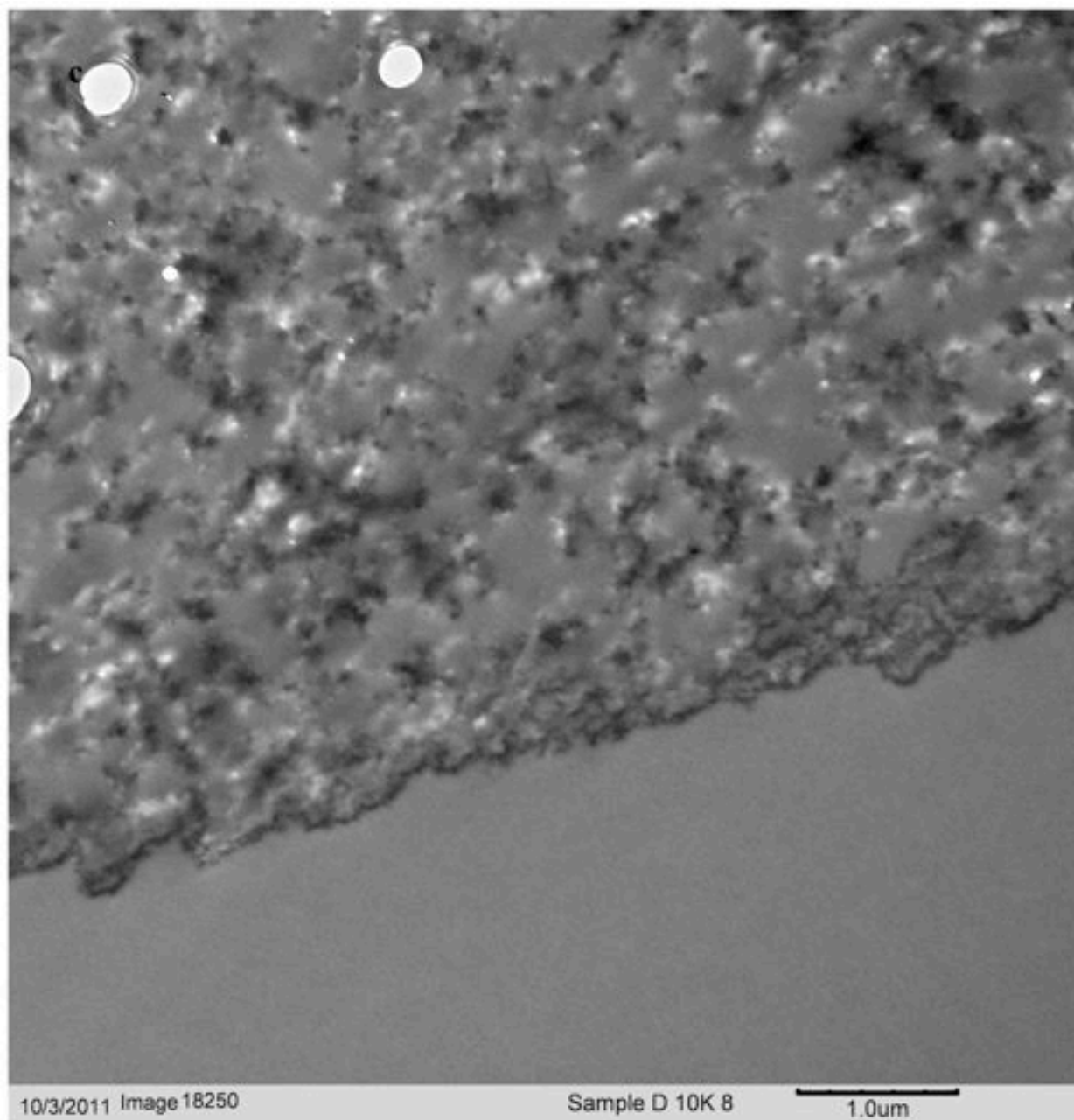
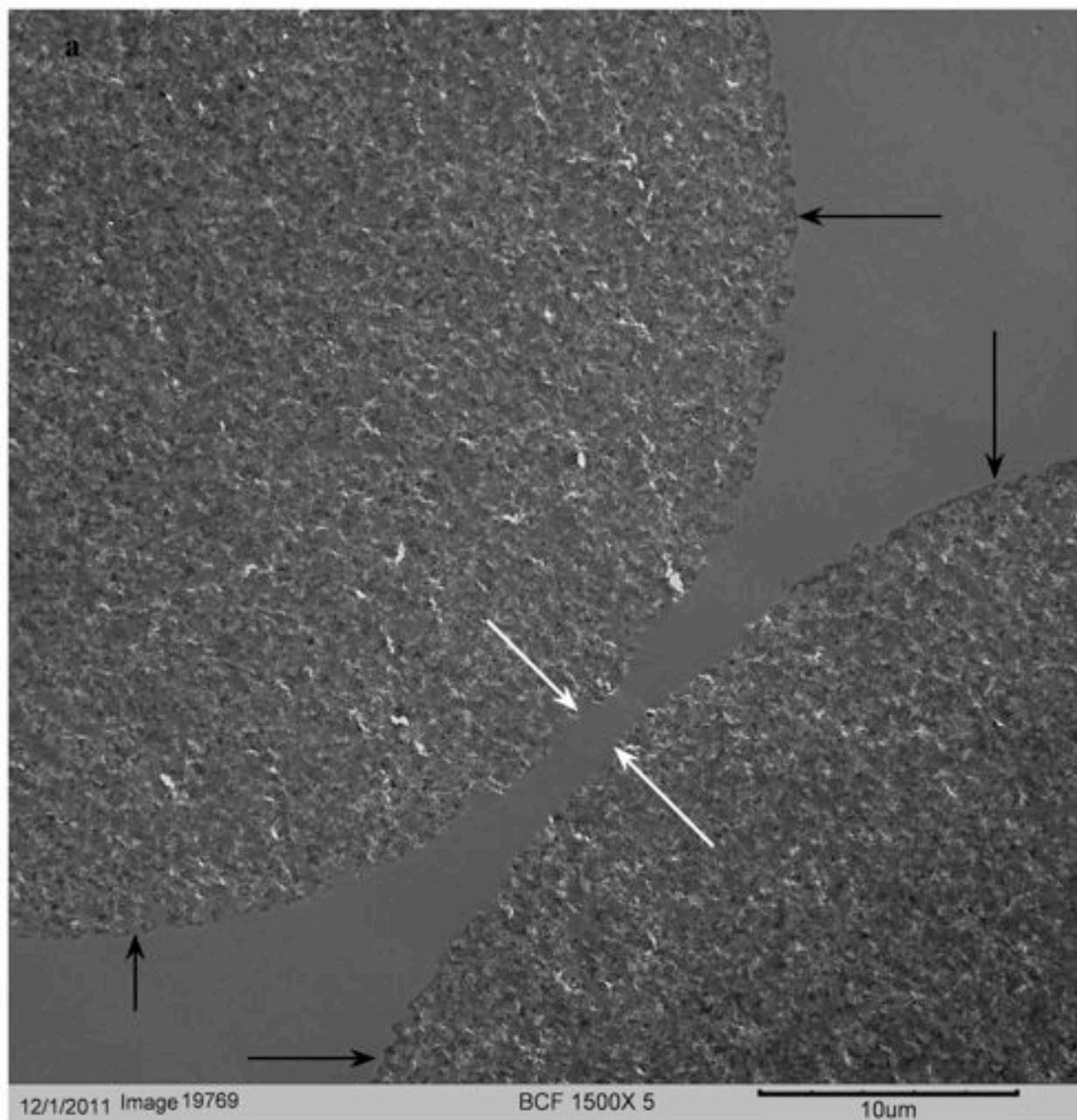


Figure 5.3.b.



**Figure 5.3.c.**



**Figure 5.4.** TEMs of Fractogel TMAE Sample B particles packed into a mini-column, mechanically compressed 30%, and fouled as discussed in Section 3.2.2.2. The black and white arrows highlight the fouled and clean areas, respectively. (a) Particles in close proximity; (b) particles in contact with each other; (c) high magnification image of particles in contact with each other; (d) high magnification image of the particles in (c); (e) high magnification image of exposed particle surface.

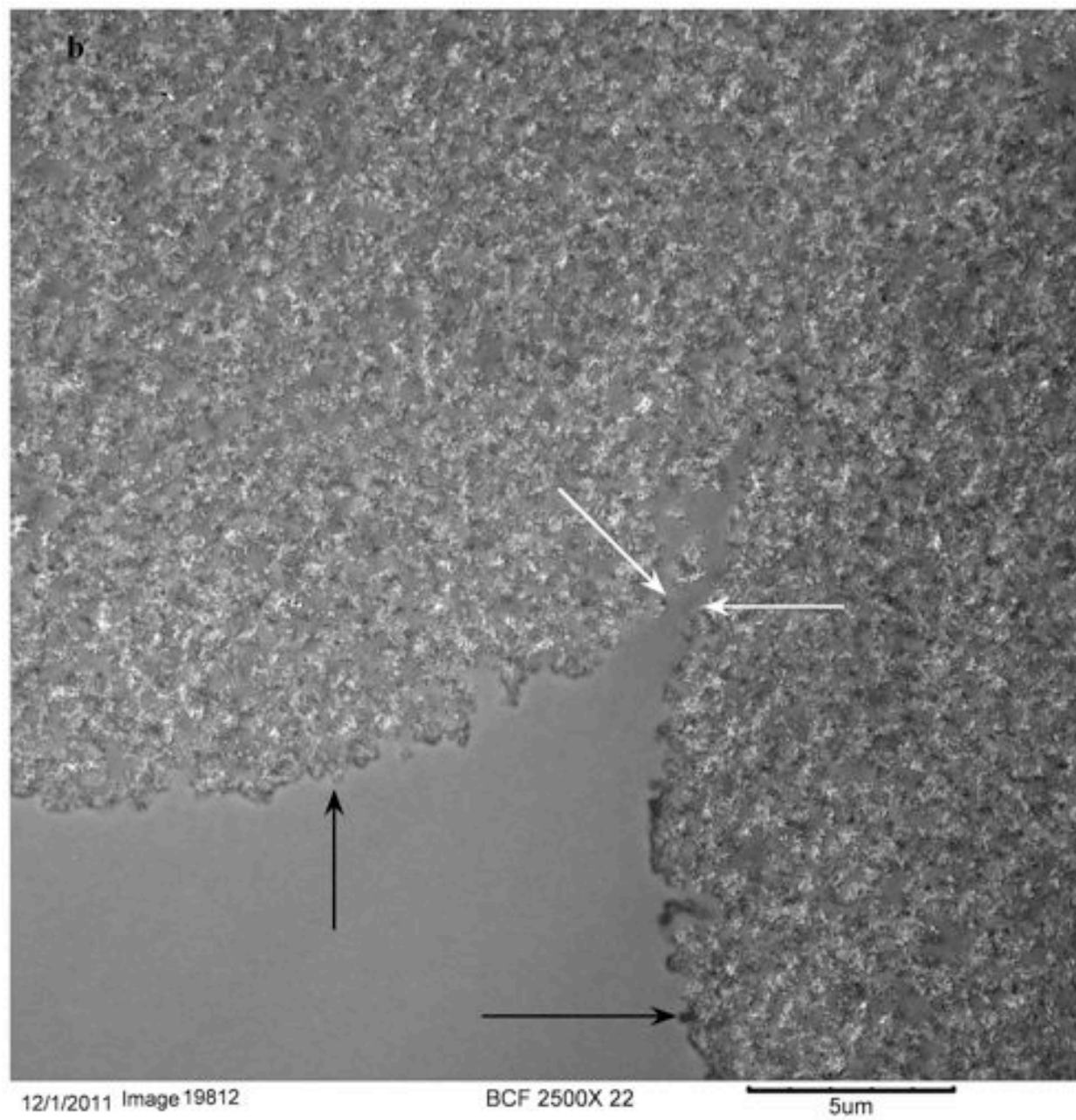


Figure 5.4.b.

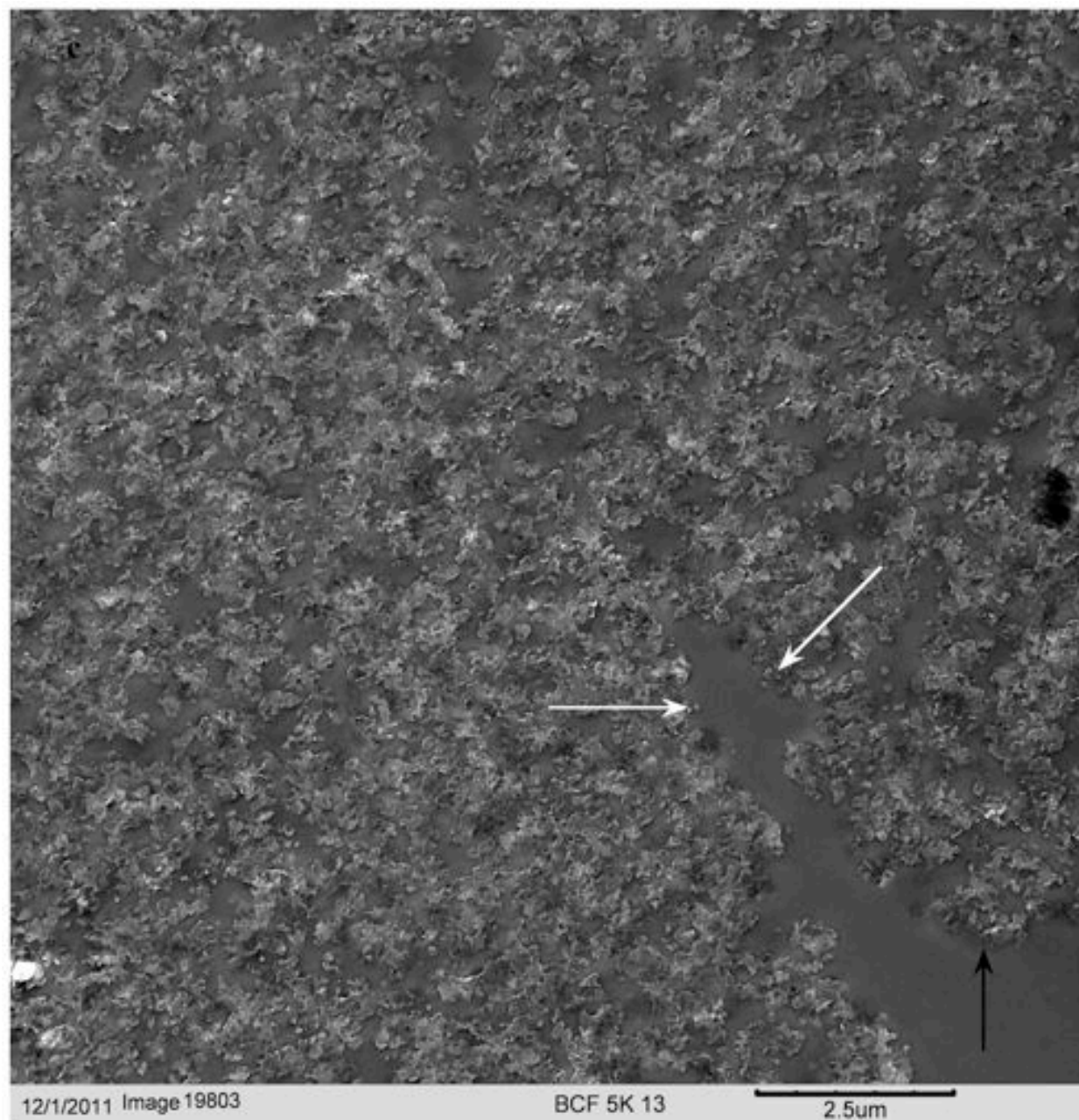
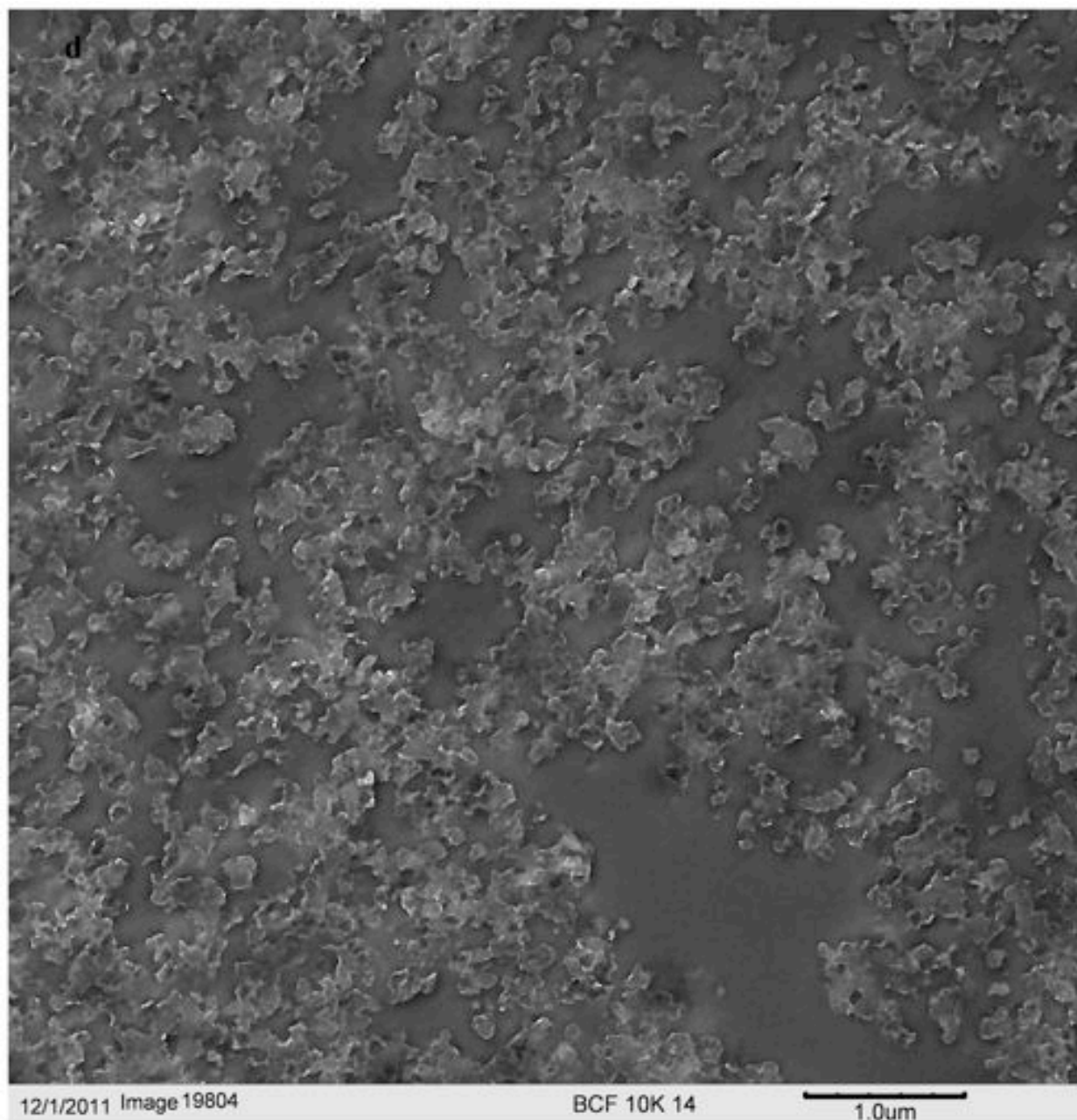


Figure 5.4.c.



**Figure 5.4.d.**

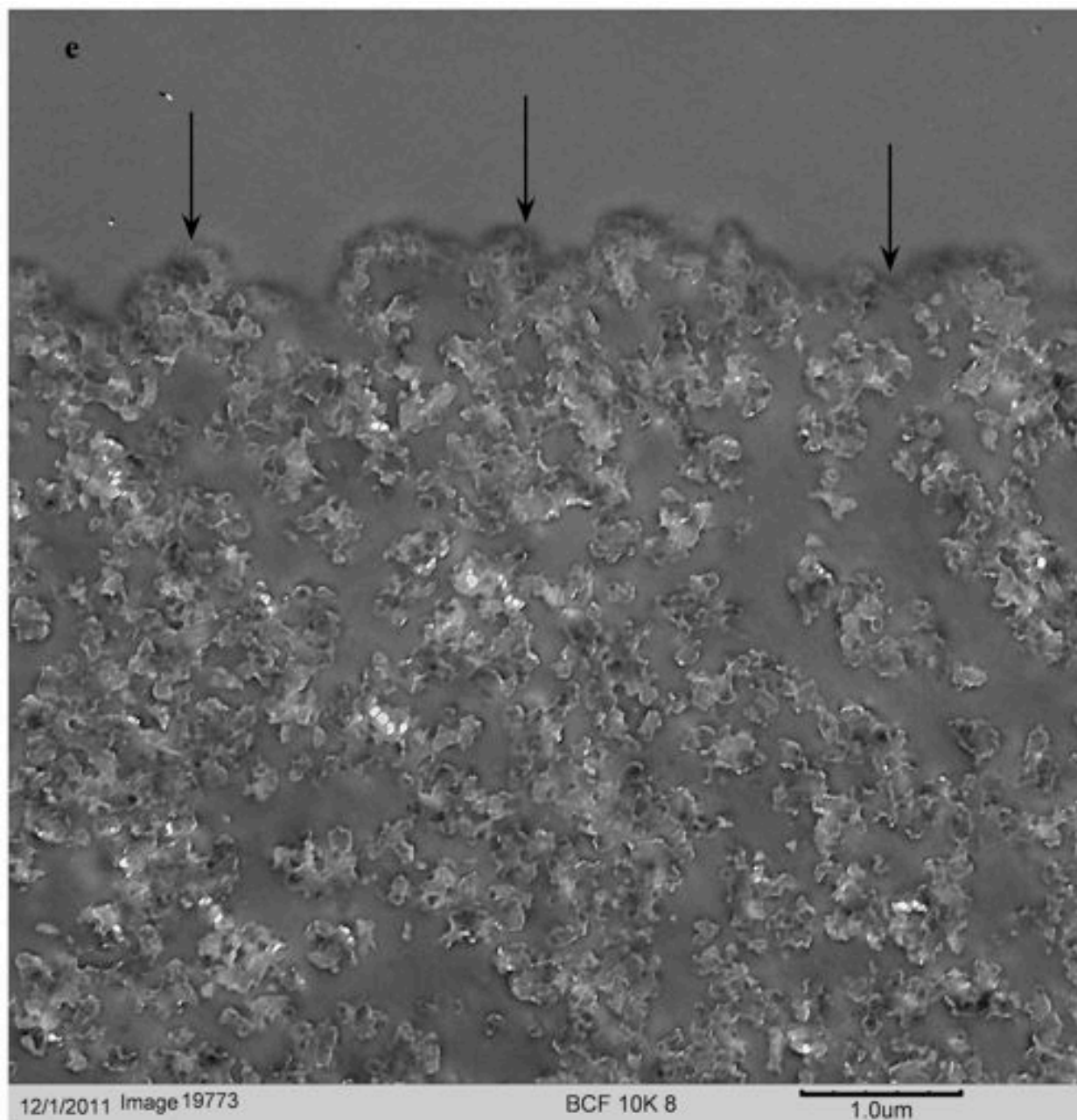


Figure 5.4.e.

are in contact with each other, but it is also minimized in regions where particles are in close proximity. The surface skin can be seen through high magnification images at the exposed edge of the particle (Fig. 5.4e), and is comparable to the skin layer present in Sample D.

In order to determine the nature of the skin layer, Sample D particles that had been subjected to a protease treatment designed to break down proteinaceous matter were obtained from Pfizer, Inc. Figure 5.5 shows electron micrographs of the protease treated sample at both 5k and 10k magnifications. Both magnifications show the absence of a skin layer indicating that the foulant consists of proteinaceous matter, which is removed by digestion with protease.

### 5.3 Protein binding capacity studies

The protein binding capacity obtained was determined to assess the effect of fouling after protein exposure for 1.5 hours. Figure 5.6 compares the binding capacities for Samples B and D for (a) purified BSA and (b) Thyroglobulin. Although equilibrium was likely not established for Tg, the Langmuir isotherm equation (eq 4.7) was still fit to the data and calculated lines are shown in the graphs. In the case of BSA, fouling does not appear to have a significant effect on the protein binding capacity. This is in agreement with the hypothesis that the discontinuous, dense skin layer allows a relatively small protein like BSA to access the particle interior. The fitted Langmuir isotherm parameters are  $q_m=166\pm 2.8$  and  $163\pm 2.6$  mg/mL of particle and  $K=130\pm 75$  and  $183\pm 122$  mL/mg for Samples B and D, respectively. It is apparent that the differences between the two samples are not significant.

In contrast to the results obtained for BSA, the amount of Thyroglobulin adsorbed in 1.5 hrs on the fouled resin was smaller than that of the virgin resin. Figure 5.6 (b) shows Samples B and D after exposure to Thyroglobulin solutions for 1.5 hours. The fitted Langmuir isotherm

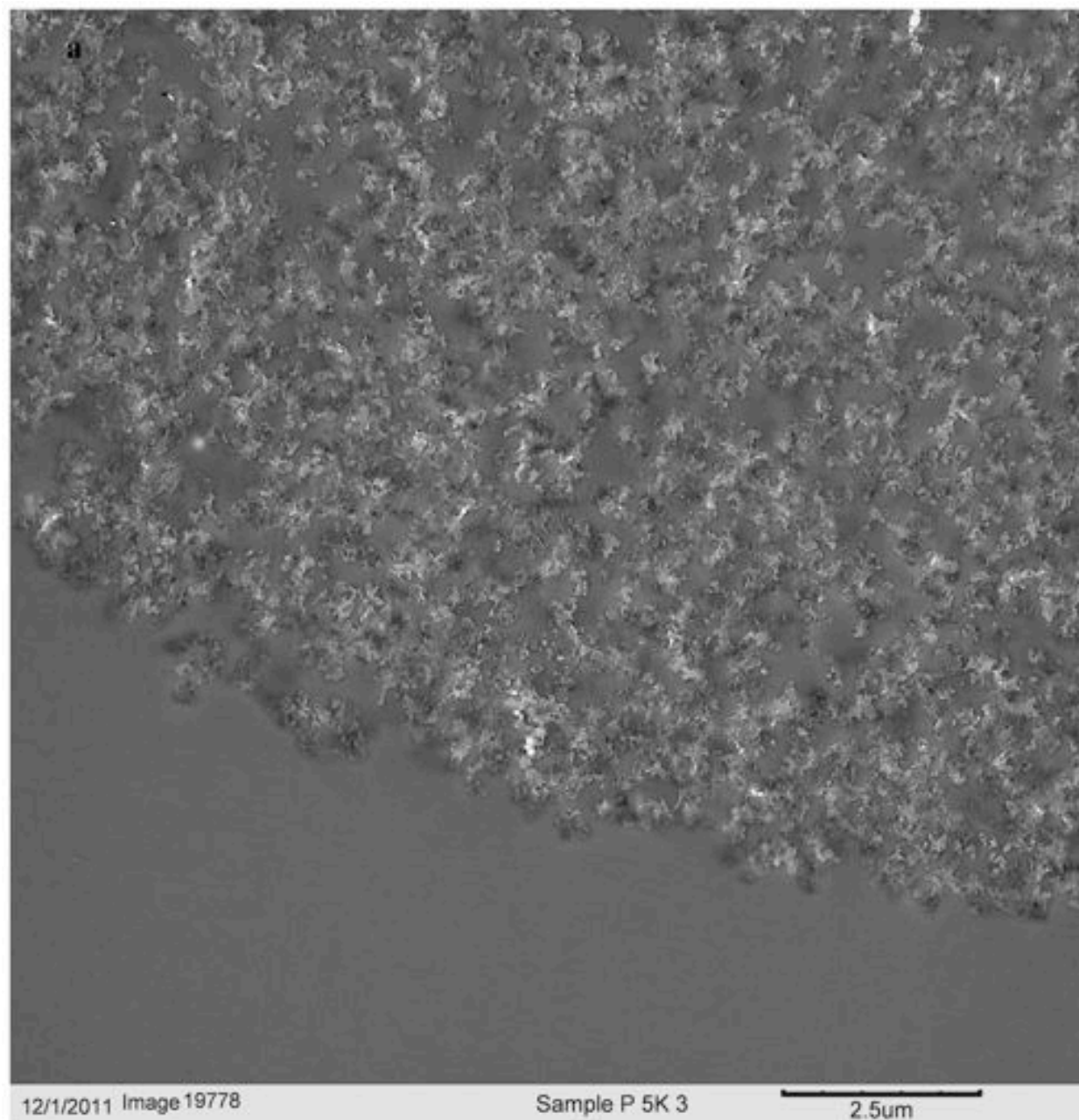


**Figure 5.5.** TEMs of a fouled sample of Fractogel TMAE after a protease treatment. (a) 5k magnification image at edge of particle; (b) 5k magnification image of particle interior; (c) 10k magnification image of edge of particle.

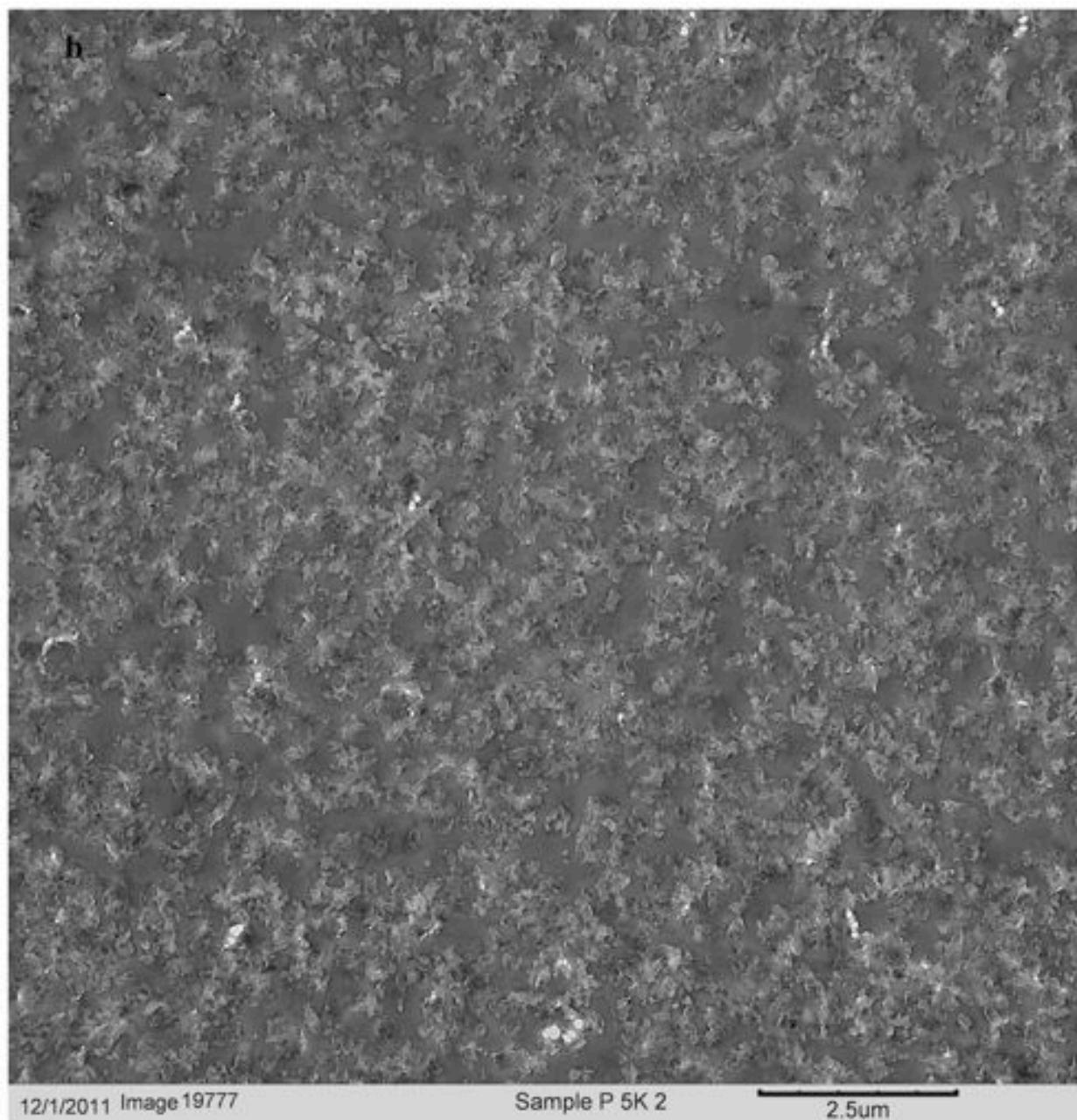


**Figure 5.5.b.**

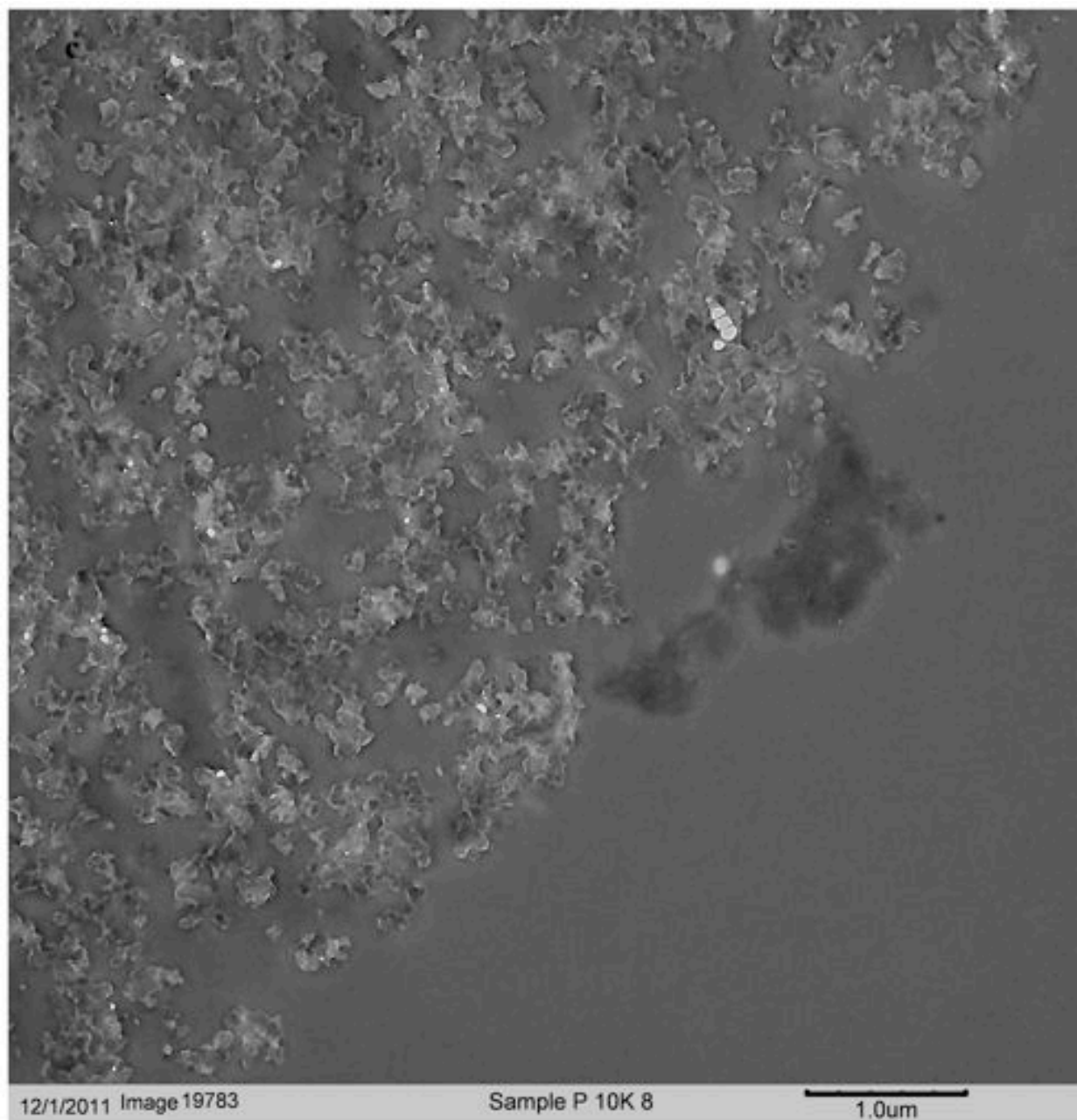


**Figure 5.5.c.**

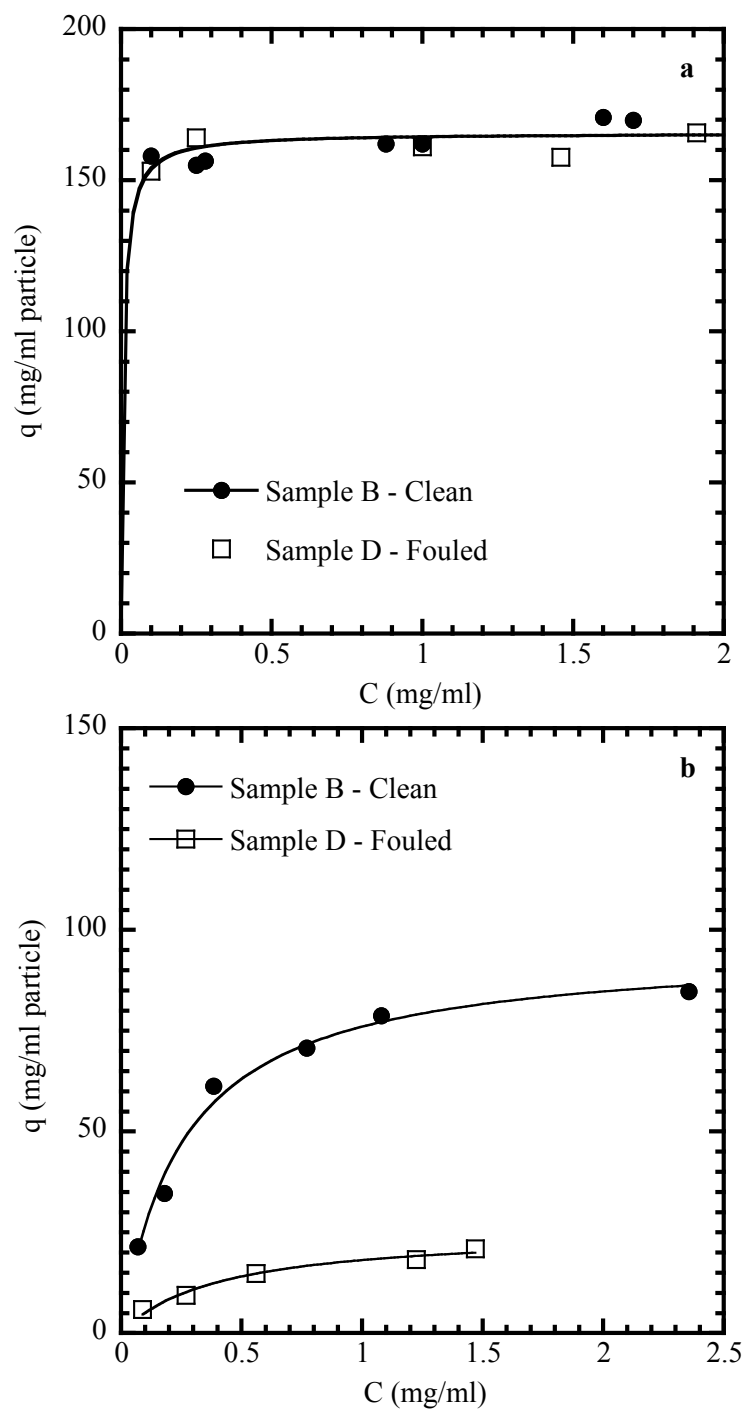


**Figure 5.6.** Protein binding capacities for Samples B and D using (a) BSA and (b) Thyroglobulin after 1.5 hours of protein exposure. Lines are calculated based on the Langmuir isotherm.

parameters were  $q_m=95\pm 4$  and  $25\pm 2$  mg/mL of particle and  $K=3.9\pm 0.5$  and  $2.5\pm 0.6$  mL/mg for Samples B and D, respectively.

### 5.3.1 Batch adsorption kinetics

The effect of fouling on the rate of protein adsorption was investigated through the use of transient batch adsorption under batch conditions. Figure 5.7 shows batch uptake curves for Samples B and D at different initial BSA concentrations. The pore diffusion model described in Section 2.1.2 was fitted to the experimental data under the assumption that the adsorption isotherm is rectangular. Table 5.2 summarizes the corresponding fitted parameters. From these data, it is evident that the rate of adsorption of BSA in the fouled sample is approximately half of the rate for the virgin sample. In fitting the data, the Sherwood number,  $Sh$ , was assumed to be 30 for the virgin resin, which is the value previously determined for similar particles (Stone and Carta, 2007). For the fouled sample, however, the Sherwood number was used as a fitted parameter to account for the additional resistance to transport caused by the skin layer. As seen in Table 5.2, a substantially lower apparent Sherwood number was obtained for the fouled resin. For these conditions, the Biot number is very small, suggesting that the combined effects of the external boundary layer mass transfer resistance and the additional resistance caused by the skin layer largely control the overall adsorption kinetics.

Figure 5.8 shows the effect of fouling on the transient adsorption of Thyroglobulin. A substantial difference is noted for the rate of adsorption which is not only much slower than that observed for the virgin resin, but also somewhat more dependent on the initial protein concentration.

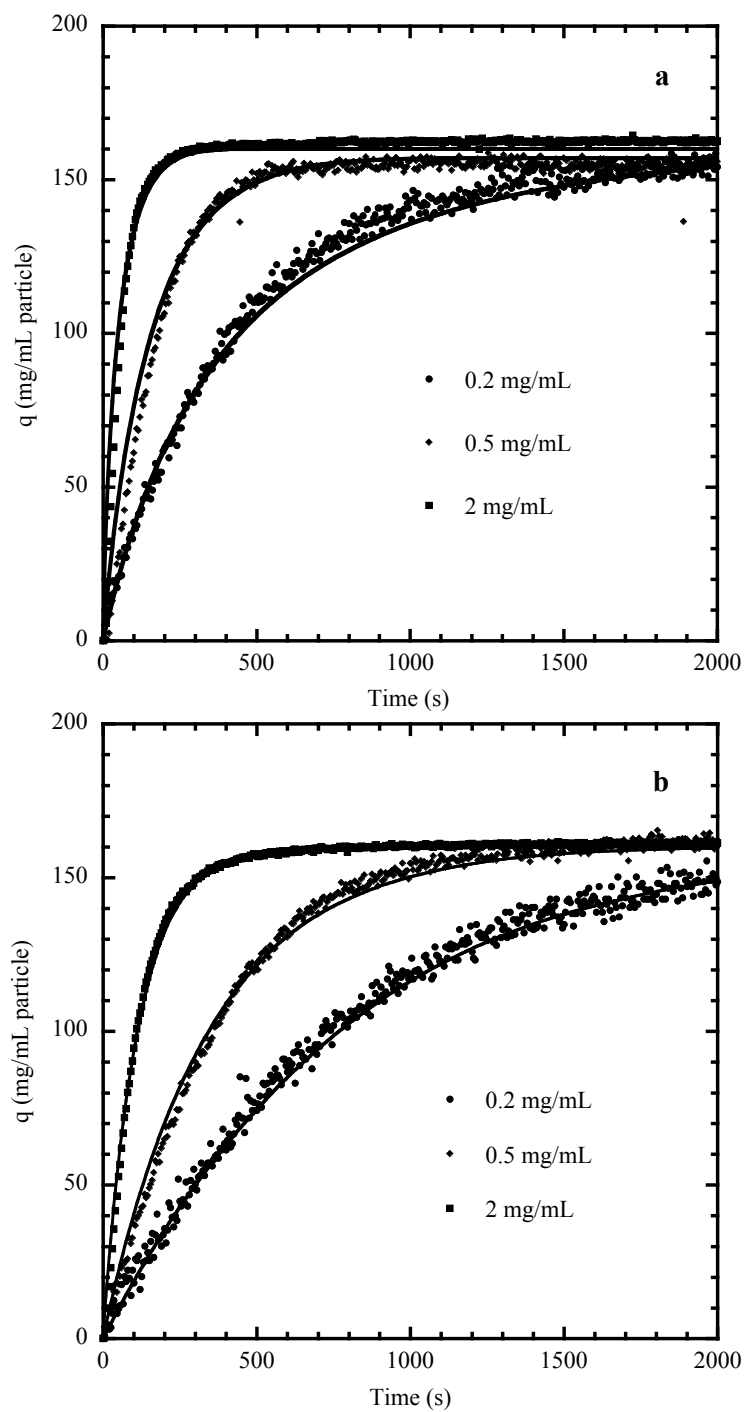


**Figure 5.7.** Batch uptake curves of BSA at different initial protein concentrations for (a) Sample B (virgin) and (b) Sample D (fouled).

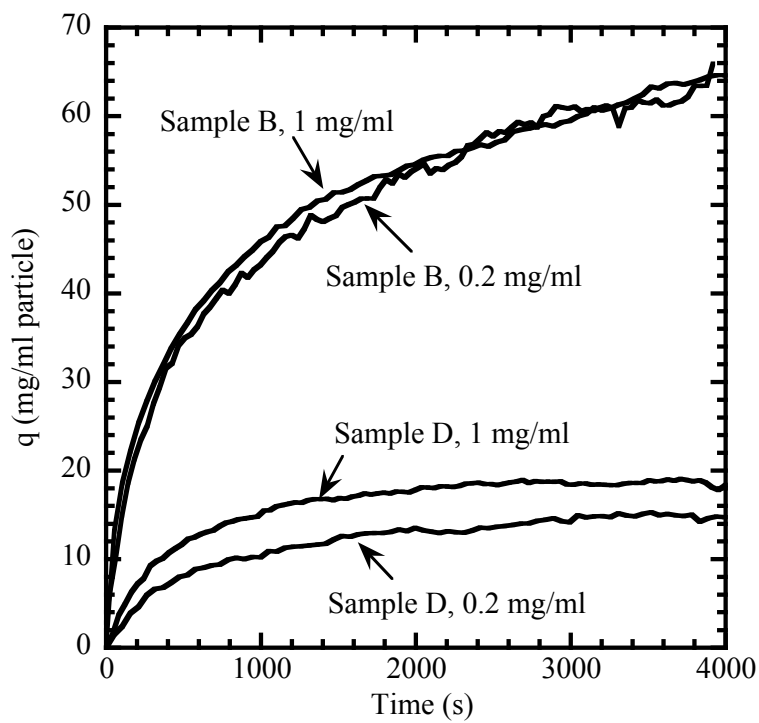


**Figure 5.8.** Batch uptake curves for Thyroglobulin at different initial protein concentrations for Samples B (virgin) and D (fouled).

**Table 5.2.** Parameters obtained by fitting batch uptake data using purified BSA for Samples B and D with the pore diffusion model.

Conditions	Sample B			Sample D		
	0.2 g/L	0.5 g/L	2 g/L	0.2 g/L	0.5 g/L	2 g/L
$D_e \times 10^{-6}$ (cm <sup>2</sup> /s)	4.0	3.0	1.5	2.0	2.0	1.4
$D_e/D_0$	6.8	5.08	2.5	3.4	3.4	2.4
$k_f \times 10^{-3}$ (cm/s)	2.5	2.5	2.5	0.85	1.02	0.76
$Sh=k_f d_p/D_0$	30	30	30	10	12	9
$Bi=k_f r_p/D_e$	2.2	2.6	5.9	1.5	1.8	1.9

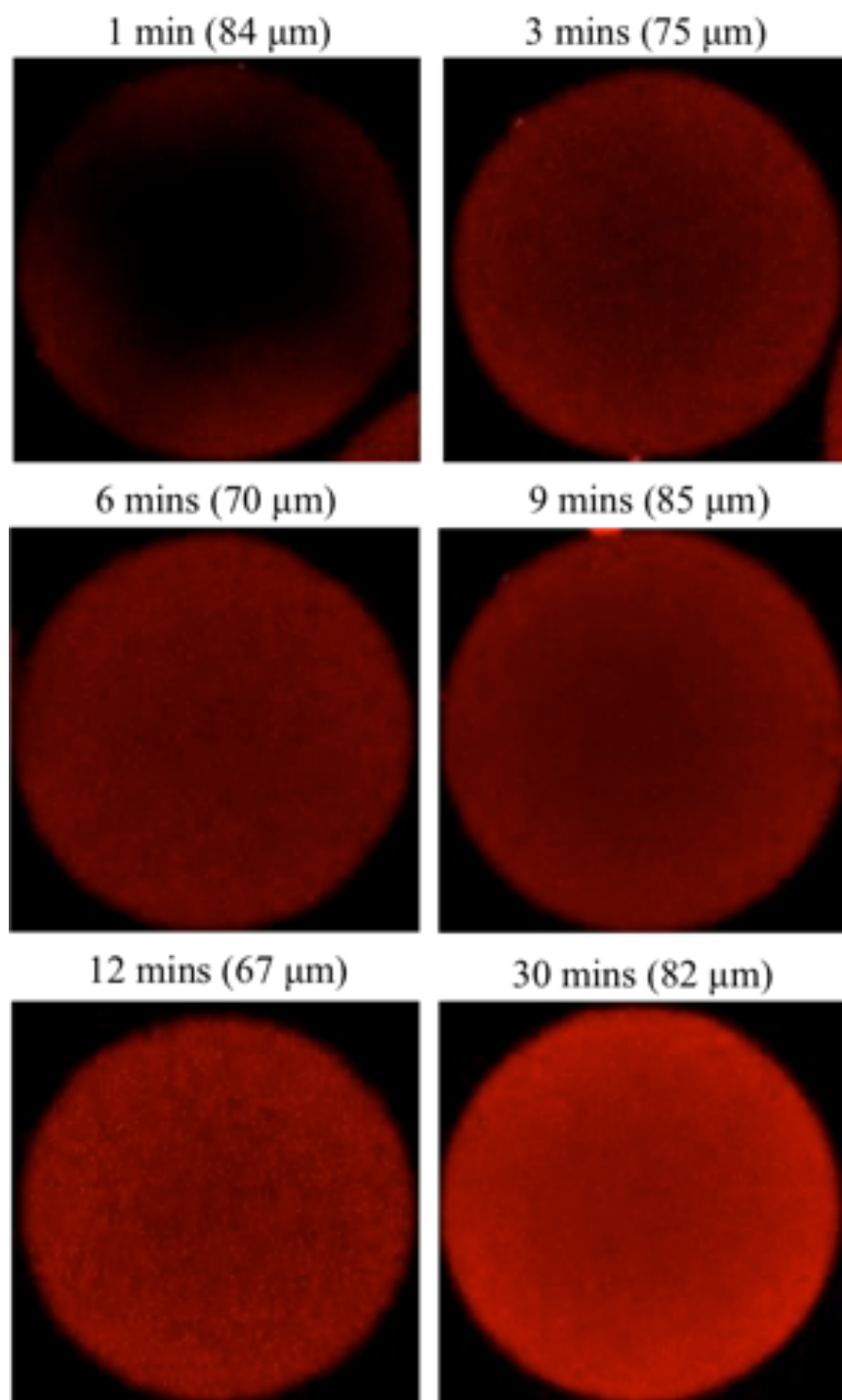
#### 5.4 Confocal laser scanning microscopy

Confocal laser scanning microscopy was used to determine the effect of the foulant on the mode of protein transport for BSA and Thyroglobulin. Studies were conducted for each protein individually and for the case where Tg is adsorbed first, followed by adsorption of BSA.

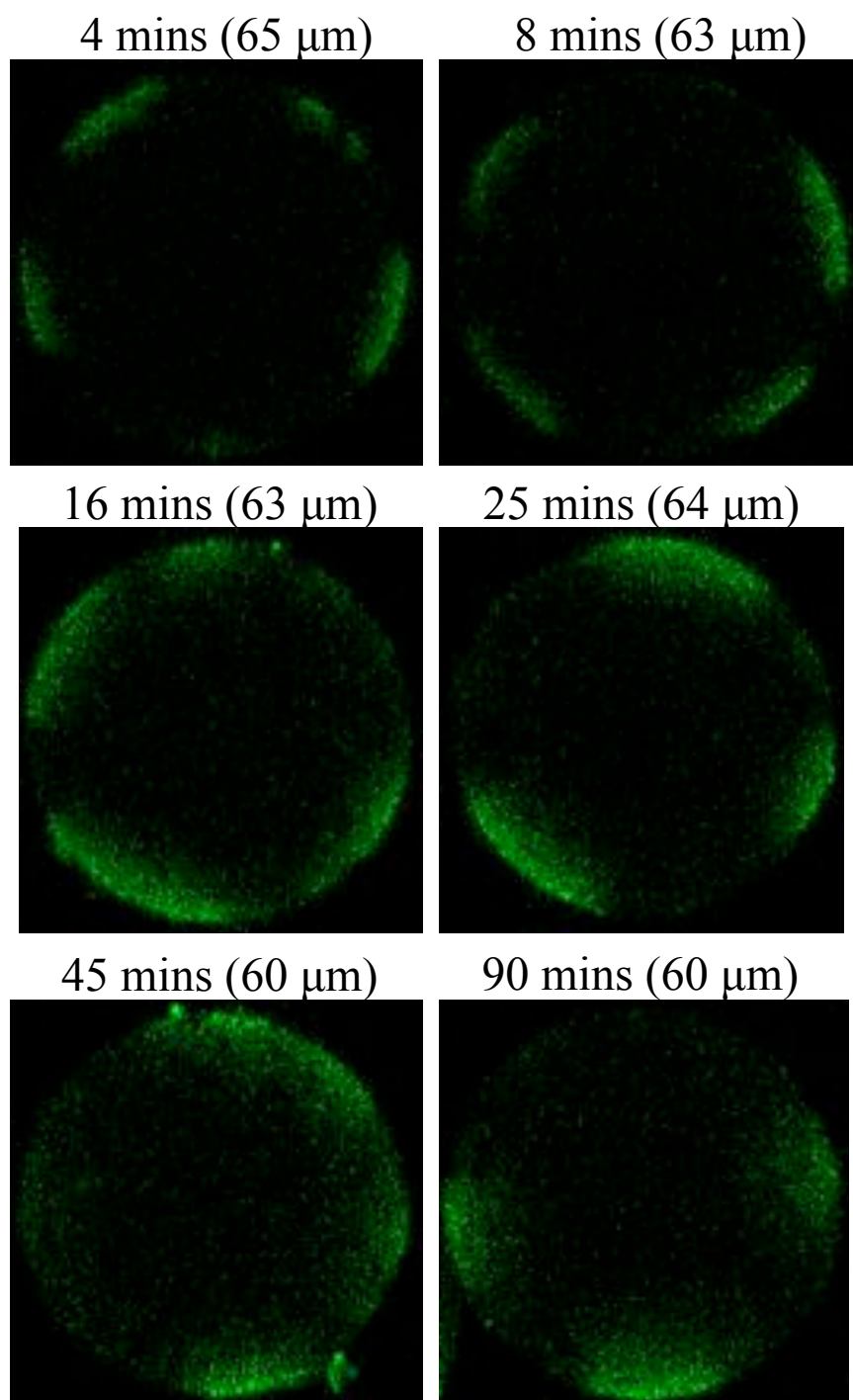
##### 5.4.1 Single component adsorption

Figure 5.9 shows the CLSM images obtained for 0.2 mg/ml BSA adsorption on Sample D. It should be noted that the laser intensity was changed from 2% for images taken up to 9 mins to 0.8% after that in order to avoid saturating the microscope CCD. Thus, these images show that after the first few minutes, the protein concentration profile is flat across the diameter, but increases uniformly with time as more BSA is bound. This is consistent with the BSA adsorption kinetics being controlled by the combined boundary layer and skin layer resistances in series. For these conditions, intraparticle diffusion of BSA is sufficiently fast to maintain a uniform concentration profile in the particle after the initial few minutes of contact with the protein solution.

Figure 5.10 shows representative CLSM images for batch adsorption of 0.2 mg/mL Thyroglobulin on Sample D. In this case, intraparticle transport of Tg appears to occur much more slowly than for BSA. As a result, what happens in the initial phases of the adsorption



**Figure 5.9.** CLSM images of batch adsorption of 0.2 mg/ml purified BSA in Fractogel TMAE Sample D. The laser intensity was varied in order to avoid saturation of the CCD detector; up to 9 minutes an intensity of 2% was used, with an intensity of 0.8% thereafter. The individual resin bead diameter is shown in parentheses above each image.



**Figure 5.10.** CLSM images of batch adsorption of 0.2 mg/ml Thyroglobulin in Fractogel TMAE Sample D. Each of the images shown was taken at an intensity of 19%. The individual resin bead diameter is shown in parentheses above each image.

process is more evident. For short times, Tg diffuses relatively fast only through a portion of the particle surface reaching significant depths of penetration. Over time, the Tg concentration profile appears to become more uniformly distributed. This result suggests that Tg transport is much more severely affected by the skin layer, which may nearly completely preclude access by this much larger protein. Despite the additional resistance to transport, the intraparticle Tg-concentration profile is fairly smooth, suggesting that transport occurs via a solid diffusion mechanism. This is consistent with the results obtained for the virgin Sample B (Fig. 4.17).

#### **5.4.2 Sequential adsorption**

Figures 5.11 and 5.12 show the sequential adsorption results for Samples B and D, respectively. In both cases, the resin was exposed to 0.2 mg/mL Thyroglobulin (Green) for 1.5 hours and then to 0.2 mg/mL BSA (Red). The CLSM images show the individual green and red channels as well as the overlay of the two.

Figure 5.11 shows that BSA adsorbs relatively quickly within the particle without displacing the bound Tg. As seen in the color overlay (bottom row of Fig. 5.11), BSA (red) moves ahead of the Tg bound near the particle's exterior surface, quickly attaining a uniform distribution (beyond the green surface layer) that grows in intensity over time as more BSA is bound. For the fouled sample (Fig. 5.12), BSA (red) moves past the region of the particle's exterior surface that shows adsorbed Tg, but also quickly fills the areas of the particle exterior surface where there is little or no Tg. This result, regarding the Tg-free areas, is consistent with that obtained for the virgin Sample B and suggests that although Tg cannot diffuse at any reasonable rate through the fouled areas, BSA can, albeit at a slower rate than through the unfouled areas.

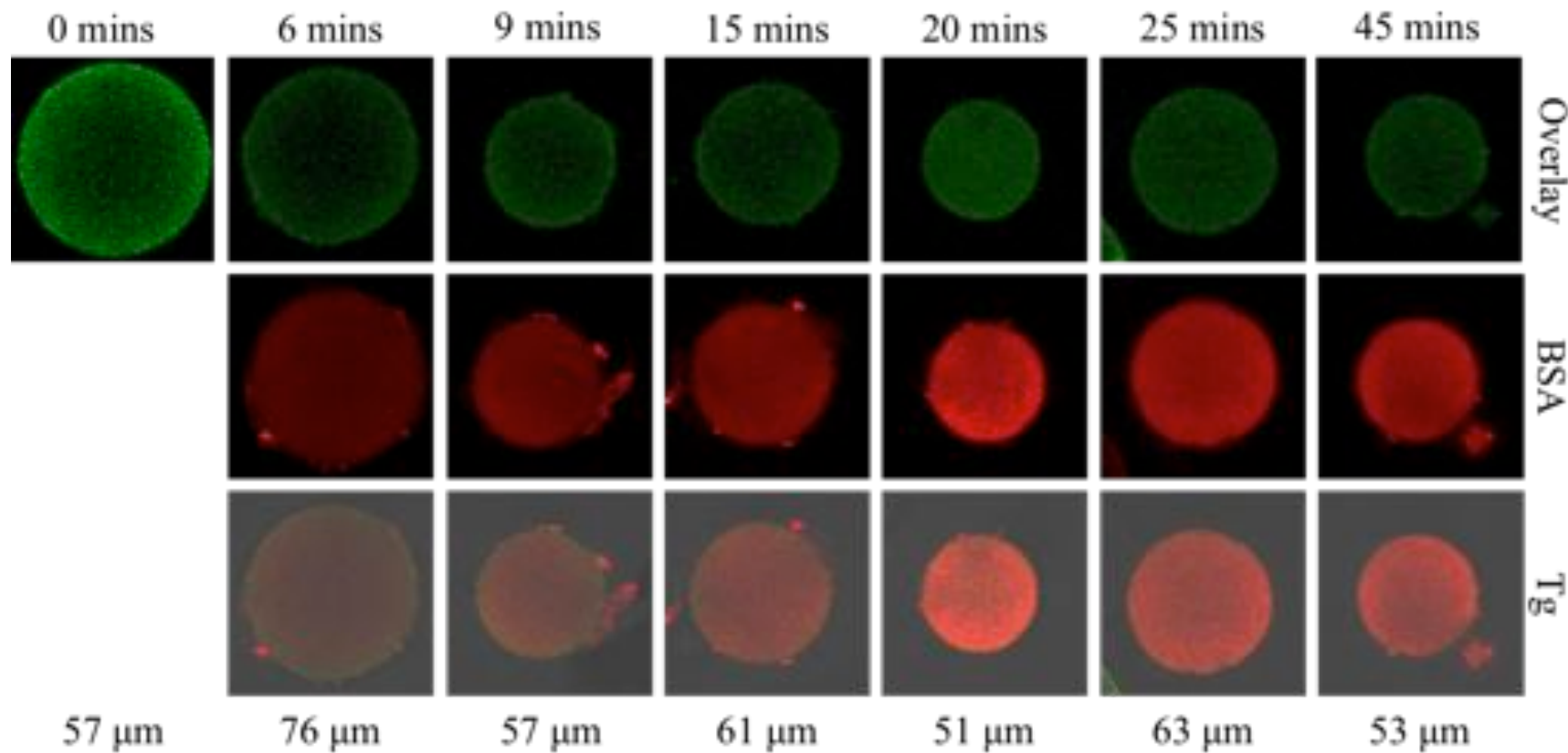


**Figure 5.11.** CLSM images of two-component batch adsorption using Thyroglobulin and purified BSA in series at concentrations of 0.2 mg/ml for Fractogel TMAE Sample B. The images were taken at an intensity of 19% for Thyroglobulin adsorption. The intensity was varied between 2% and 0.8% for the BSA adsorption in order to avoid saturation. The individual resin bead diameter is shown below each image.

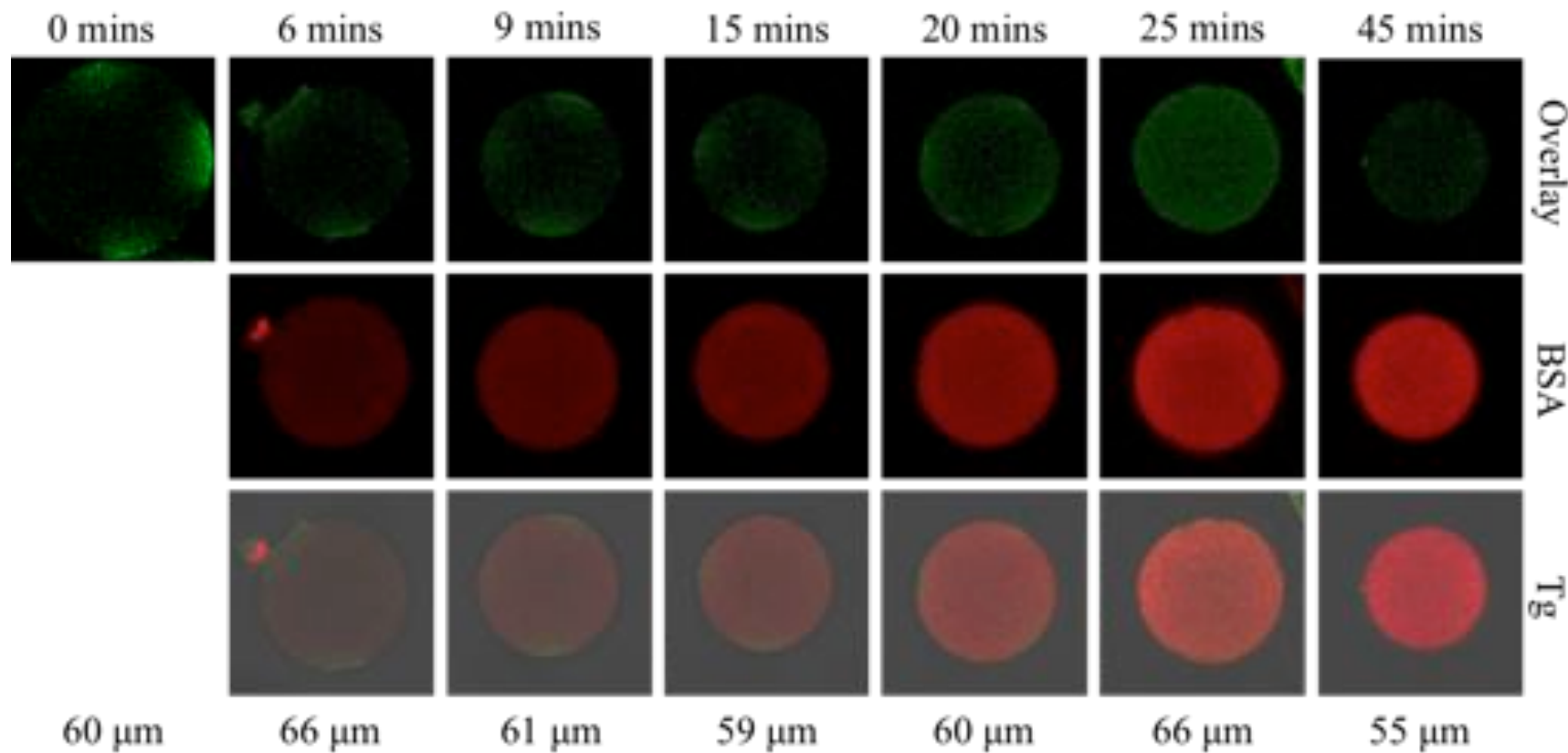


**Figure 5.12.** CLSM images of two-component batch adsorption in series using purified BSA and Thyroglobulin at concentrations on 0.2 mg/ml for Fractogel TMAE Sample D. The images were taken at an intensity of 19% for Thyroglobulin adsorption. The intensity was varied between 2% and 0.8% for the BSA adsorption in order to avoid saturation. The individual resin bead diameter is shown below each image.

## Chapter 6. Conclusions

Through this study, important physical and adsorption characteristics of Fractogel TMAE HiCap were elucidated. The impact of fouling was investigated, though additional work is needed in determining the foulant species. The following conclusions could be made from these studies:

### 6.1 Physical properties of Fractogel TMAE HiCap (m)

The key physical properties of the two Fractogel TMAE lots under consideration were the particle size distribution, accessible pore radius, pore structure, and the packing properties. The different lots provided equivalent results in the determination of the particle size distribution, resulting in values of  $d_p=70$  and  $72 \mu\text{m}$  for Samples A and B, respectively. The reproducibility of measurements when using different resin lots was further validated using iSEC, where minimal differences were seen in the elution peaks of the dextran probes. Through the use of a bimodal model it was determined that of the total void fraction of 0.82, only 10% are “macropores” with a radius on the order of 40 nm, as reported by the manufacturer. The other 90% of the structure is made up of “micropores”, which are between 4-5 nm in radius. The use of un-retained proteins proved that the results determined via dextran probes were due to size alone. Minimal variability was seen in the internal structure (observed using TEM), where both lots yielded images showing a microgranular structure with a heterogeneous distribution of pore sizes across the particle radius. The BSA saturated sample reveals the globular-like appearance of the resin when the majority of available sites are filled. A compressibility study was used to shed light on the packing properties. The results of this study indicate that although the resin is made up of a rigid polymethacrylate backbone, the introduction of functionalized tentacles within the pores allows a change in particle volume when exposed to external pressure.

## 6.2 Protein adsorption properties

A set of model proteins (BSA and Thyroglobulin) was used to characterize the protein adsorption properties of the resin using both pseudo-equilibrium and batch adsorption studies. The binding capacity of the resin was determined via adsorption studies at 1.5 and 24 hours. For BSA, the length of the experiment does not have a significant effect on the binding capacity of the resin, where nearly rectangular isotherms are achieved for both times. Thyroglobulin yields quite different results where not only the binding capacity but also the dependence of protein concentration is affected by the length of the experiment. By fitting the Langmuir equation to the 24-hour experimental data, a quantitative comparison of the model proteins' binding capacities was made, resulting in a 70% difference in the binding capacity of Tg when compared to that of BSA. This difference is likely due to the diffusional limitations presented by the large size of Tg in comparison to BSA.

The batch adsorption study using BSA allows for the rate of protein adsorption to be observed and quantified using the pore diffusion model, which assumes a rectangular isotherm. The binding capacity achieved through this study was comparable to the 1.5-hour isotherm values, and approximately 10% less than the 24-hour values. The substantial difference in the rate of adsorption for the two concentrations under consideration emphasizes the dependence of protein transport on the initial concentration. The small Biot values shed further light on the transport mode, indicating that the external mass transfer resistance is dominant. The latter two trends indicate that ordinary pore diffusion is not the main contributor to the mechanism of protein transport. The batch adsorption data for Thyroglobulin presents a quite different scenario where there is minimal dependence of the rate of adsorption on the initial protein concentration.

This trend indicates that due to the large size of the molecule, the external mass transfer resistance is negligible and does not affect the overall process of protein adsorption.

### **6.3 Mechanism of protein transport**

Confocal laser scanning microscopy was used to determine the mode of protein transport within individual Fractogel TMAE beads under batch conditions for a set of model proteins. The transport of both BSA and Thyroglobulin were shown to be “surface diffusion” controlled, resulting in a flat concentration profile within a few minutes of exposure to the protein solution. Once a flat profile is attained, protein continues to adsorb within the particle pores at what seems to be a uniform rate.

### **6.4 Impact of process Use**

The nature of the foulant species was investigated through physical characterization studies, including accessible pore radius, pore structure (fouled and protease treated samples), and packing properties. The accessible pore radius, determined by fitting a bimodal pore distribution model to iSEC retention volumes yields only slight differences between the virgin and fouled samples. This result indicates that the accessibility of the particle is not changed by the presence of the foulant. Transmission electron micrographs reveal the foulant to be a discontinuous dense skin layer, approximately 0.5  $\mu\text{m}$  thick. Although there is a clear presence of foulant species on the external surface of the particle, the particle interior retains a microgranular appearance suggesting minimal fouling within the particle pores. Through TEM imaging of a protease treated sample, the external foulant layer was reduced indicating that the foulant is proteinaceous. The discontinuous skin layer was further investigated by fouling a mechanically compressed mini-column. These studies showed minimal foulant present when particles were in close contact, and no visible foulant where particles were touching.

The effect of the foulant species on protein adsorption was investigated using pseudo-equilibrium and batch adsorption studies. Adsorption studies using BSA resulted in similar binding capacities for both virgin and fouled resin, further validating the hypothesis that the external skin layer does not hamper the accessibility of the particle pores to small molecules. A quite different result was seen for Tg, where binding capacity of the fouled resin was only 26% of that found for the virgin resin. This result indicates the importance of the additional mass transfer resistance, which was further investigated using batch adsorption studies. A pore diffusion model was fitted to batch adsorption data for BSA on both virgin and fouled resins. This model provides a good fit for the data and allows a quantitative apparent effective diffusivity to be determined. The fitted parameters yielded a significantly lower apparent Sherwood number as well as very small Biot numbers. This result suggests that the overall adsorption kinetics are controlled by a combination of the external mass transfer resistance and the additional resistance caused by the foulant layer. The batch adsorption data for Thyroglobulin resulted in a very poor fit for the pore diffusion model, yet from observation of the curves a significant difference in the rate of adsorption between the virgin and fouled resin can be seen.

Single component and sequential adsorption confocal microscopy studies were used to determine the effect of the foulant species on the mechanism of protein transport. Adsorption of BSA on the fouled resin showed comparable results as those obtained for the virgin resin, once again showing that the foulant layer has minimal effect on the accessibility of small molecules to the particles pores. However, transient adsorption of Tg revealed that at short times the protein only has access through a portion of the particle surfaces emphasizing the effect of the additional resistance on protein adsorption. Sequential studies for the virgin resin showed the rapid

adsorption of BSA bypass the Tg bound near the particle surface without displacing it. A similar adsorption profile is seen for the fouled sample, where BSA bypasses the Tg bound on the surface of the particle, however, BSA also binds in the regions on the exterior surface where Tg is not present. These results suggest that although Tg does not bind within the fouled layer at a reasonable rate, BSA is able to readily diffuse through the skin layer but results in a slower rate of adsorption when compared to the clean sample.

## Chapter 7. Recommendations

Future studies should be conducted to determine the foulant species and the mechanism of process related fouling. The recommendations for these studies are as follows:

### 7.1 Determination of foulant species

Gold labeling studies should be used to determine the foulant species within the dense skin layer present on the fouled sample. The foulant was shown to be proteinaceous by the removal of the skin layer using a protease treatment. It is hypothesized that the foulant layer is comprised of either host cell protein or monoclonal antibody aggregates. To determine the foulant species, carboxyl spherical gold nanoparticles (SGNPs) can be conjugated to proteins through amine bonds using EDC chemistry. An anti-HCP immunoglobulin G and Protein A could be used as the conjugate proteins due to their affinity to HCP and mAb, respectively. The result of this study would shed light on the localization of each throughout the resin matrix, and potentially indicate the species within the foulant skin layer. These experiments could be conducted using two different protocols. The first protocol would be to expose the virgin and fouled resin samples to the SGNP conjugates prior to embedding the resin. The diffusional hindrance due to the large size of the SGNPs may restrict the transport of the conjugates through the fouled layer, and therefore a second protocol would be needed to examine the localization of foulant species within the particle interior. The second protocol would be to embed the virgin and fouled resin samples as previously described in Section 3.2.2. The ultramicrotomed sections would then be exposed to the SGNP conjugates prior to TEM imaging. A future complication of this study is the effect of the dehydration and embedding processes on the external foulant layer. If the proteinaceous species become denatured, the SGNP conjugates will not be able to specifically bind to the foulant.

## 7.2 Mechanism of process related fouling

A better understanding of the mechanism of fouling is necessary. Confocal laser scanning microscopy (CLSM) could be used to investigate the manner in which the foulant layer is formed through fluorescent labeling. It is known that the Protein A eluate pool consists of HCP, target antibody, and DNA. Through separation processes, the eluate pool could be separated to give solutions containing the individual species. The HCP and mAb solutions could then be fluorescently dyed using the amine reactive dyes available within the lab. The utilization of flow cell technology would allow the fouling process to be observed in real time. Virgin resin particles would then be placed within a capillary tube through capillary diffusion. The particles would be fouled using the proprietary protocol to mimic the actual process. A multi-valve flow cell would be necessary to alternate the flow through solutions from the fouling solutions to a sucrose solution in order to match the refractive index of the resin. Through observance of the binding of each individual species, a better idea of the mechanism of fouling may be obtained.

## Chapter 8. References

- Armenante, P.M., Kirwan, D.J., 1989, "Mass transfer to microparticles in agitated systems," *Chem. Eng. Sci.*, 44 (12), pp 2781-2796.
- Beynon, R., Easterby, J., 1996, *Buffering Solutions – The Basics*, Oxford University Press, Oxford, pg. 69
- Carta G., Ubiera A., Pabst T., 2005, "Protein mass transfer kinetics in ion exchange media: Measurements and interpretations," *Chem. Eng. Technol.*, 28, pp. 1252-1264.
- Carta, G., Jungbauer, A., 2010, *Protein Chromatography: Process Development and Scale-Up*, Wiley, Weinheim.
- Chen et al., 2002, "Analysis of diffusion models for protein adsorption to porous anion-exchange adsorbent," *Journal of Chromatography A*, 962, pp. 29-40
- Cromwell et al., 2006, "Protein aggregation and bioprocessing," *The AAPS Journal*, Vol. 8, Issue 3, pgs E572-579.
- Cussler, E.L., 1997, *Diffusion: Mass Transfer in Fluid Systems*, Cambridge University Press, New York.
- Dziennik et al., 2003, "Nondiffusive mechanisms enhance protein uptake rates in ion exchange particles," *Proceedings of the National Academy of Science*, Vol. 100, 2, pp. 420-425.
- EMD Chemicals, 2011, *Fractogel EMD: Advancing your life sciences – from discovery to launch*.
- Froment G., Bischoff K., 1990, *Chemical Reactor Analysis and Design*, Second Edition, Cambridge University Press, New York.
- Hagel L., Östberg M., Andersson T., 1996, "Apparent pore size distributions of chromatography media," *Journal of Chromatography A*, 743(1), pp. 33-42.
- Kelley B. et al., 2008, "Weak partitioning chromatography for anion exchange purification of monoclonal antibodies," *Biotechnology and Bioengineering*, 101, pp. 553-566.
- Lenhoff, A., 2008, "Multiscale modeling of protein uptake patterns in particles," *Langmuir*, 24, pp. 5991-5995.
- Lenhoff, A., 2011, "Protein adsorption and transport in polymer-functionalized ion-exchangers," *Journal of Chromatography A*, 1218, pp. 8748-8759
- LeVan, M.D., G.Carta, C.M. Yon. Adsorption and Ion Exchange, 2007, Section 16 in D.W. Green (Ed.) *Perry's Chemical Engineers Handbook*, 8<sup>th</sup> Edition, McGraw-Hill, New York.

Perez et al., 2011, "Protein adsorption and transport in cation exchangers with a rigid backbone matrix with and without polymeric surface extenders," *Biotechnol. Prog.*, Vol. 28, No. 5, pp. 1264-1272.

Schirmer, E., Carta, G., 2008, "Protein adsorption kinetics in charged agarose gels: Effect of agarose content and modeling," *AIChE Journal*, Vol. 55, Issue 2, pp. 331-341.

Shukla A., Hinckley P., 2008, "Host cell protein clearance during Protein A chromatography: Development of an improved column was step," *Biotechnol. Prog.*, 24, pp. 1115-1121.

Stone M., Carta G., 2007, "Protein adsorption and transport in agarose and dextran-grafted agarose media for ion exchange chromatography," *Journal Chromatography A*, 1146(2), pp. 202-215.

Stone M. C., Tao Y., Carta G., 2009, "Protein adsorption and transport in agarose and dextran-grafted agarose media for ion exchange chromatography: Effect of ionic strength and protein characteristics," *Journal of Chromatography A*, 1216(20), pp. 4465-4474.

Stickel J., Fotopoulos A., 2001, "Pressure-flow relationships for packed beds of compressible chromatography media at laboratory and production scale," *Biotechnol. Progr.*, 17(4), pp. 744-751.

Suda et al., 2009, "Comparison of agarose and dextran-grafted agarose strong ion exchangers for the separation of protein aggregates," *Journal of Chromatography A*, 1216, pp. 5256-5264.

Swindells et al., 1958, "Viscosities of sucrose solutions at various temperatures: tables of recalculated values," *Supplement to National Bureau of Standards Circular 440*, pp. 1-7.

Tartutani, O., Shulman, S., 2002, "Properties of carbohydrate-stripped Thyroglobulin: I. Preparation and physicochemical properties of desialized Thyroglobulin," *Biochim. Biophys Acta.*, 229, pp. 642-648.

Thermo Scientific, 2008, "Extinction coefficients: A guide to understanding extinction coefficients, with emphasis on spectrophotometric determination of protein concentration," *Pierce Biotechnology*, pp. 1-3.

Tyn M., Gusek T., 1990, "Prediction of diffusion-coefficients of proteins," *Biotechnol. Bioeng.*, 35(4), pp. 327-338.